# Interferometric schemes: a probe for topological edge states, a tool in weak measurements

Inauguraldissertation

zur Erlangung der Würde eines Doktors der Philosophie
vorgelegt der Philosophisch-Naturwissenschaftlichen
Fakultät der Universität Basel

von

Grégory Strübi

aus Zürich (ZH), Schweiz

UNI
BASEL

Basel, 2014

**Attribution-NonCommercial-NoDerivatives 3.0 Switzerland**
(CC BY-NC-ND 3.0 CH)

**You are free:** **to Share** — to copy, distribute and transmit the work

**Under the following conditions:**

**Attribution** — You must attribute the work in the manner specified by the author or licensor (but not in any way that suggests that they endorse you or your use of the work).

**Noncommercial** — You may not use this work for commercial purposes.

**No Derivative Works** — You may not alter, transform, or build upon this work.

**With the understanding that:**

- **Waiver —** Any of the above conditions can be **waived** if you get permission from the copyright holder.
- **Public Domain —** Where the work or any of its elements is in the **public domain** under applicable law, that status is in no way affected by the license.
- **Other Rights —** In no way are any of the following rights affected by the license:
    - Your fair dealing or **fair use** rights, or other applicable copyright exceptions and limitations;
    - The author's **moral** rights;
    - Rights other persons may have either in the work itself or in how the work is used, such as **publicity** or privacy rights.
- **Notice —** For any reuse or distribution, you must make clear to others the license terms of this work. The best way to do this is with a link to this web page.

Quelle: creativecommons.org/licenses/by-nc-nd/3.0/ch/deed.en Datum: 12.11.2013

Genehmigt von der Philosophisch-Naturwissenschaftlichen Fakultät auf Antrag von

Prof. Dr. Christoph Bruder

Prof. Dr. Björn Trauzettel

Basel, den 25. März 2014

Prof. Dr. Jörg Schibler, Dekan

# Summary

In the first part of this thesis we propose interferometric schemes to probe the properties of edge states of topological insulators and superconductors. First, we consider two helical liquids on opposite edges of a narrow two-dimensional topological insulator, which are connected by one or several local tunnel junctions. In the presence of spatially inhomogeneous Rashba spin-orbit coupling, the spin textures of the helical states on opposite edges are different. We demonstrate that this has a strong impact on the electron transport between the edges. In particular, in the case of many random tunnel contacts, the localization length depends strongly on the spin textures of the edge states. We also propose to realize a Fabry-Pérot interferometer to measure the spin texture.

Second, we consider domain walls between superconducting and magnetic regions placed on top of a topological insulator, that were predicted support transport channels for Majorana fermions. We propose to study noise correlations in a Hanbury Brown-Twiss type interferometer and find three signatures of the Majorana nature of the channels. First, the average charge current in the outgoing leads vanishes. Furthermore, we predict an anomalously large shot noise in the output ports for a vanishing average current signal. Adding a quantum point contact to the setup, we find a surprising absence of partition noise which can be traced back to the Majorana nature of the carriers. Finally, we calculate the full counting statistics of this structure. At zero bias, we find an interpretation of Majorana-mediated charge transport in terms of two independent half-charge processes.

In the second part of this thesis, we explain how the quantum theory of weak measurements inspired a new method for the measurement of small effects and precision metrology. Many successful implementations of the weak-value amplification scheme have been recently reported. We review this scheme in some details with an emphasis on its benefits and limitations. We then generalize the method, and propose to use weak measurements away from the weak-value amplification regime to carry out precision measurements of time delays of light. Our scheme is robust to several sources of noise that are shown to only limit the relative precision of the measurement. Thus, they do not set a limit on the smallest measurable phase shift contrary to standard interferometry and weak-value based measurement techniques. Our idea is not restricted to phase-shift measurements and could be used to measure other small effects using a similar protocol.

# Acknowledgments

First, I would need to express my deepest gratitude to Christoph Bruder, my advisor, whose guidance and continued encouragements were of invaluable help to the completion of this work. It was also a great pleasure to collaborate with Wolfgang Belzig, Mahn-Soo Choi, Christoph Orth, and Thomas Schmidt.

A special thanks goes to Samuel Aldana, Patrick Hofer, Jennifer Nussbaum, Vladimir Stojanovic, Andreas Wagner, and Stefan Walter, for making the life at the office enjoyable. Many thanks also go to all the current and former members of the Basel group: Daniel Becker, Stefano Chesi, Gerson Ferreira, Jan Fischer, Suhas Gangadharaiah, Kevin van Hoogdalem, Adrian Hutter, Jelena Klinovaja, Christoph Klöffel, Viktoriia Kornich, Axel Lode, Daniel Loss, Franziska Maier, Tobias Meng, Simon Nigg, Andreas Nunnenkamp, Fabio Pedrocchi, Diego Rainis, Hugo Ribeiro, Maximilian Rinck, Beat Röthlisberger, Arijit Saha, Manuel Schmidt, Thomas Schmidt, Peter Stano, Dimitrije Stepanenko, Constantin Schrade, Rakesh Tiwari, Luka Trifunovic, Mircea Trif, Ying-Dan Wang, Talitha Weiss, James Wootton, Robert Zak, Robert Zielke, and Alexander Zyuzin.

Finally, I would like to thank my family and Ursula Zweifel for their love and support.

# Contents

# Chapter 1

# Introduction

In many ways, quantum mechanics is nothing but a very complicated interferometer. The manifestation of this statement is most clearly seen in Feynman's path integral representation. The propagator

$$K(x,t;x',t') = \int \mathcal{D}y(\tau) \exp\left(i\frac{S[y(\tau),\dot{y}(\tau),\tau]}{\hbar}\right), \tag{1.1}$$

which describes the full time evolution of the quantum state of a particle, is written as the sum over all possible paths $y(\tau)$ that the particle can take, subsumed to the boundary conditions $y(t) = x, y(t') = x'$. All of these trajectories *interfere* together according to the phase, given by the classical action functional over the quantum of action $S/\hbar$, they pick-up along the way.

Reciprocally, practical interferometry experiments are described by very simple quantum mechanics. But simple does not mean uninteresting. Roughly speaking, an interferometer with two arms can be viewed as a device that singles out two trajectories $y_1(\tau)$ and $y_2(\tau)$ in Eq. (1.1), with the corresponding actions $S_1$ and $S_2$. The resulting probability

$$|K(x,t;x',t')|^2 = \frac{1+\cos(\phi)}{2} \tag{1.2}$$

allows us to probe very sensitively the phase difference $\phi = (S_1 - S_2)/\hbar$, and thereby learn about various physical phenomena in a controlled way.

The Aharonov-Bohm effect [Aharonov59] is a striking illustration of this line of thought. In a celebrated *gedanken experiment* Aharonov and Bohm considered the motion of an electron subject to an electromagnetic vector potential $\boldsymbol{A}$ due to a magnetic field. The electron is constrained to move along two paths that go around the magnetic region, without entering it. As a result the electron never feels any classical force during its motion. Quantum mechanics, however, predicts that there is a nontrivial phase $\phi_{\rm AB}$ associated to these trajectories due to the vector potential $\boldsymbol{A}$

$$\phi_{\rm AB} = -\frac{e}{\hbar}\oint_C \boldsymbol{A}\cdot d\boldsymbol{l}\,, \tag{1.3}$$

where $C$ describes the closed curve formed by the two interferometer arms. Although the Aharonov-Bohm phase only depends on the magnetic flux enclosed in the loop $C$,

it has far reaching consequences for the significance of the electromagnetic potentials in quantum physics; they are not mere computational tools, but have a real, measurable, physical effect.

## 1.1 Thesis overview

In the first part of this thesis,we pursue this paradigm of using interferometric techniques as a tool to probe the edge states of topological states of matter. First, in Chapter 2, we give an introduction to the topic of topological insulators and superconductors that host the edge states of interest. In Chapter 3 we propose a Fabry-Pérot interferometer that allows to map the spin structure of 2d topological insulators. We also show a strong dependence of the localization length of the edge states on the spin texture in disordered and narrow samples. In Chapter 4 we look for transport signatures of Majorana fermions in interferometric schemes. Most notably, we find an absence of partition noise for Majorana fermions that can be connected to their charge neutrality.

In the second part, we explain how the quantum theory of weak measurements inspires new methods in interferometric schemes. In Chapter 5 we introduce the weak-value amplification method with a focus on its benefits and disadvantages. In Chapter 6 we give a generalization of this method that allows for further improvements of precision metrology. We propose an explicit scheme to measure ultrasmall time delays of light that outperforms weak-value amplification.

# Part I

# Probing topological edge states with interferometry

# Chapter 2

# Edge states and topology

The recent theoretical prediction [Kane05a, Bernevig06] and subsequent discovery [König07] of topological insulators triggered a lot of interest from the scientific community. The surprise also came from the simple description of topological insulators in terms of their single-particle band structure only; a theory that had allegedly already revealed all its secrets.

Topological insulators [Hasan10, Qi11] look like ordinary insulators in the bulk, in particular they display an electronic bulk band gap, but their peculiarity is revealed at interfaces with ordinary, topologically trivial, insulators (like vacuum): there lives a gapless electronic mode. Moreover these modes possess unusual properties. Edge states of 2D topological insulators are *helical*, spin-up electrons, say, run counterclockwise around the sample and spin-down run clockwise. Moreover, due to time-reversal symmetry, backscattering is forbidden and charge transport occurs without dissipation. Surface states of 3D topological insulators are described by the Dirac equation for massless fermions somewhat like in graphene, although without the spin and valley degeneracy of the latter.

Edge states of 2D topological insulators were rapidly connected to a bulk property of the materials: a $\mathbb{Z}_2$ topological invariant [Kane05b], an analogue to the Chern number of the integer quantum Hall effect [Thouless82, Simon83], for time-reversal-invariant systems. The strength of such topological invariants is their robustness to small perturbations; as long as perturbations do not close the band gap, the topological invariant remains unchanged. The novelty here is the realization of the role of symmetry. In this case time-reversal symmetry is crucial to force the topological invariant to take values 1 or 0 and no intermediate values.

Generalizing these ideas to include particle-hole symmetry and the chiral symmetry along with higher spatial dimensions leads to a whole periodic table of topological insulators and topological superconductors [Schnyder08, Ryu09, Kitaev09, Budich13] that all display interesting surface states with interesting properties. For instance Majorana fermions, fermions which are their own antiparticle, appear at the boundary of topological superconductors.

The goal of this chapter is to introduce the concept of topologically protected edge states to the reader. To this end, we first review briefly the edge state description of the integer quantum Hall effect, and the related quantum anomalous Hall effect and quantum spin Hall effect. Second, we make the connection between these edge states and the topological properties of the bulk materials. Finally, we introduce Majorana fermions

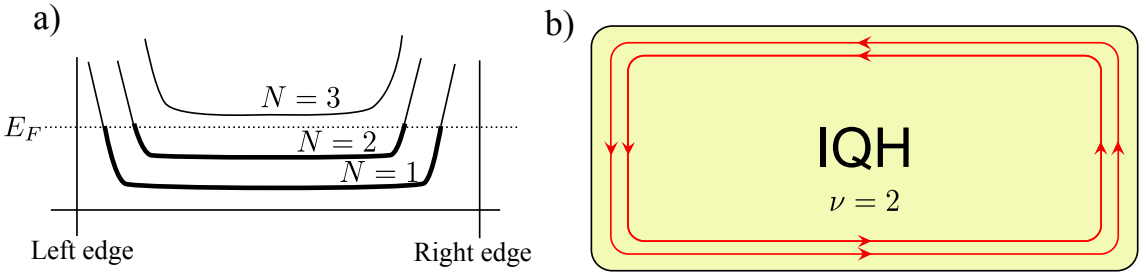


Figure 2.1: (a) Energy of ideal Landau levels across a sample with boundaries with filling fraction $\nu = 2$. The two first Landau levels cross the Fermi energy near the edges. (b) Corresponding chiral edge states of the IQH in a rectangular sample in real space. The arrows mark the direction of propagation.

which naturally arise as edge states of topological superconductors.

## 2.1 Three quantum Hall effects

### 2.1.1 Integer quantum Hall effect

The story starts with the experimental discovery of the integer quantum Hall (IQH) effect [Klitzing80]. Soon afterwards, theorists came up with ingenious ideas to explain the remarkably accurate Hall conductance quantization to integer multiples of the conductance quantum $G = \nu e^2/h$, where $\nu$ is the filling factor. Laughlin showed [Laughlin81] that the Hall conductivity ought to be quantized due to gauge invariance and the presence of a mobility gap. Halperin [Halperin82] refined the argument and predicted the existence of current-carrying edge states even in the presence of a moderate amount of disorder.

The intuitive picture for the edge states is that the Landau levels are pushed higher in energy at the boundaries of the sample and thus cross the Fermi level. Each occupied Landau level in the bulk gives rise to a metallic one-dimensional electron channel localized near the edge, see Fig. 2.1. The key property of these edge states is their *chirality*: they locally allow electrons to move in one direction only; they propagate either clockwise or anticlockwise around the whole sample. The consequence is that an electron moving in one of these chiral channels cannot experience backscattering unless it goes through the bulk to the other side of the sample, but the mobility gap of the bulk material makes this process effectively impossible for sufficiently large samples.

The transport properties of a 2D electron gas in the IQH state can be entirely described by the chiral edge states even though there is also a nonvanishing bulk current density in general [Komiyama96]. In this context, we can easily understand the observed conductance quantization for $\nu = 1$ within the Landauer-Büttiker formalism. The conductance of a one-dimensional channel is given by $Te^2/h$, where $T$ is the transmission probability of electrons across the channel. In the absence of backscattering $T = 1$ and the conductance is quantized. The origin of this quantization is the exact cancellation between the density of states and the group velocity of electrons. Büttiker [Büttiker88] showed that local elastic and inelastic scattering between the channels ($\nu > 1$) and disordered contacts does not break the picture for macroscopic Hall samples, i.e. samples larger than the inelastic

mean free path. Each edge state contributes equally to the transport of electrical current and the quantized conductance $\nu e^2/h$ is robust in transport experiments.

### 2.1.2 Quantum anomalous Hall effect

Haldane [Haldane88] came up with a model to obtain a quantum Hall effect without the need for an external magnetic field. He was able to show that the crucial ingredient is, in fact, the breaking of time-reversal symmetry (TRS). More precisely, the mobility gap of the bulk material must have a time-reversal-symmetry breaking origin.

The model he considered is based on "2D graphite" (nowadays, graphene) with a bipartite honeycomb lattice. The biparticity allows to define two sublattices $A, B$ such that nearest neighbour hopping connects $A$ sites to $B$ sites only and vice-versa. The unit cell contains one $A$ site and one $B$ site. It is natural to introduce an abstract two-dimensional sublattice space together with the Pauli matrices $\sigma$ acting in this space. Additionally he introduced a phase-dependent next-nearest neighbour hopping term $t_2 e^{i\phi}$ that connects sites of the same sublattice. The hopping phase $\phi$ breaks TRS for $\phi \neq 0, \pi$. The physical origin of such a term is of little importance for us now (we shall see a relevant example in the discussion of the quantum spin Hall effect). Finally, there is a "staggered potential" term $M\sigma_z$, which preserves TRS, that competes with the next-nearest neighbour hopping. The Hamiltonian in $k$-space reads

$$H(k) = 2t_2 \cos\phi \sum_i \cos(\boldsymbol{k}\cdot\boldsymbol{b}_i) + t_1 \sum_i \cos(\boldsymbol{k}\cdot\boldsymbol{a}_i)\sigma_x + t_1 \sum_i \sin(\boldsymbol{k}\cdot\boldsymbol{a}_i)\sigma_y \tag{2.1}$$

$$+ \left( M - 2t_2 \sin\phi \sum_i \sin(\boldsymbol{k}\cdot\boldsymbol{b}_i) \right) \sigma_z \,, \tag{2.2}$$

where $\boldsymbol{a}_i$ are the 3 vectors connecting nearest neighbour $A$ sites to $B$ sites, and $\boldsymbol{b}_i$ are the next-nearest neighbour equivalents. For $M = t_2 = 0$ the spectrum is gapless and the low-energy sector of the model is described by two Dirac cones centered around the two "valleys" of graphene, i.e. the two unequivalent corners of the Brillouin zone.

With nonzero values of $M$ and $t_2$ gaps

$$\Delta_\alpha = M - \alpha 3\sqrt{3}\, t_2 \sin\phi \tag{2.3}$$

open at the two valleys ($\alpha = \pm 1$). The low energy spectrum becomes that of two massive Dirac fermions $E_\alpha = \sqrt{(m_\alpha c^2)^2 + (ck_\alpha)^2}$, with $m_\alpha c^2 = \Delta_\alpha$ and where $\boldsymbol{k}_\alpha$ are the momenta measured from the center of the valleys.

The result of his analysis is that when the strength of the TRS breaking term overcomes the trivial mass term, $|3\sqrt{3}\, t_2 \sin\phi| > M$, the Hall conductivity is nonzero and is quantized to $\pm e^2/h$. As in the IQH effect there is a gapless chiral edge state associated to this nontrivial conductivity.

### 2.1.3 Quantum spin Hall effect

Similarly to the classical Hall effect, where a voltage transverse to the direction of propagation of an electric current in the presence of a magnetic field builds up, an intrinsic spin Hall effect, where spin accumulates on the edges transverse to the direction of propagation

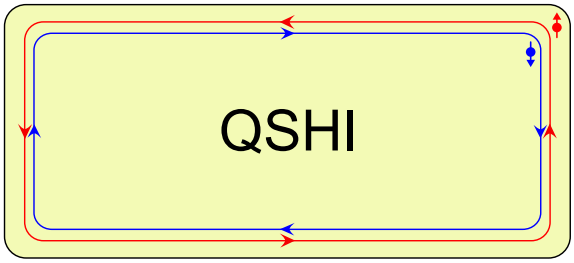


Figure 2.2: Helical edge states of the quantum spin Hall (QSH) state. Electrons with spin up propagate counterclockwise around the sample, while spin-down electrons propagate clockwise. Both edge states are at the same spatial position, the shift is only for readability.

of an electric current without a magnetic field, was predicted [Dyakonov71]. The origin of this effect is spin-orbit coupling: roughly speaking, an electric current looks like an effective magnetic field of opposite direction for the two spin orientations; the conventional Hall effect thus leads to a spin accumulation on the edges of the sample. The first reported observation of the intrinsic spin Hall effect was made in 2005 [Wunderlich05].

### Kane-Mele model

The quantized version, the quantum spin Hall (QSH) effect, was predicted to occur in the then recently discovered graphene [Kane05a] by an analogy to the quantum anomalous Hall effect (QAH). The key idea is to replace the phase-modulated hopping term, $t_2$ term in Eq. (2.2), by an intrinsic spin-orbit coupling.

Kane and Mele consider a low-energy effective model around the two valleys of graphene. They consider the Hamiltonian

$$H = -i\hbar v_F(\sigma_x\tau_x\partial_x + \sigma_y\partial_y) + \Delta_{\text{so}}\sigma_z\tau_z s_z \tag{2.4}$$

where the Pauli matrices $\tau$ act in valley space, $\sigma$ in sublattice space, and $s$ in spin space. The spin-orbit term is even under time-reversal as is the whole Hamiltonian. In this model, the $z$ component of the spin is a good quantum number. It thus suffices to consider the two sectors $s_z = \pm 1$ independently. Each sector taken separately violates TRS and reduces to the continuum version of the Haldane model (2.2) with $M = 0, \Delta_{\text{so}} = 3\sqrt{3}\,t_2 \sin\phi$ and is thus in the QAH state. The chirality of the QAH state produced depends on the sign of $s_z$. Therefore, we obtain two copies of QAH states with opposite chiralities. This state possesses so-called *helical* edge states: electrons with spin up propagate counterclockwise around the sample while spin-down electrons propagate clockwise, see Fig. 2.2. The electrical Hall conductivity vanishes $\sigma_{xy} = 0$, as it must be for a TRS preserving system. However, the spin Hall conductivity is quantized

$$\sigma^s_{xy} = \frac{\hbar}{2}\left(\frac{e}{h} - (-)\frac{e}{h}\right) = \frac{e}{2\pi}\,, \tag{2.5}$$

hence the name of quantum spin Hall effect.

The robustness of the helical edge states against backscattering is less obvious than for chiral edge states; at first it seems that any kind of disorder will couple them and induce a

gap. However, this is not the case. The argument is that the two edge states are Kramers partners and no time-reversal-symmetric perturbation can couple them. The helical edge states are thus protected against electrostatic disorder for instance. On the other hand, magnetic disorder will generically induce a gap.

The quantization of the spin Hall conductivity is also not robust against any breaking of the spin axial symmetry. For instance if we include a Rashba spin-orbit coupling term

$$H_R = \lambda_R(\sigma_x\tau_z s_y - \sigma_y s_x)\,, \tag{2.6}$$

then $s_z$ is no longer a good quantum number and the spin rotates while propagating along the edge states. Such a term generically occurs in the presence of an electric field perpendicular to the plane. Nevertheless, Kane and Mele showed that the edge states persist in this case, as long as $\lambda_R < \Delta_{\text{so}}$ [Kane05a].

Unfortunately, later calculations showed that the spin orbit gap opened at the Dirac point is too small ($\Delta_{\text{so}} < 0.01$ meV) for the QSH effect to be observed in graphene [Min06, Yao07]. A recent proposal [Weeks11, Hu12] suggests that the spin orbit gap could be enhanced by several orders of magnitude by doping the graphene sheet with heavy atoms, and make the QSH effect visible at accessible temperatures.

Bernevig, Hughes, and Zhang predicted that quantum wells CdTe-HgTe-CdTe would display the QSH effect in the HgTe layer when the latter is thicker than a critical thickness $d \approx 64$ Å. This was famously confirmed by a subsequent experiment by König *et al.* [König07] which observed dissipationless transport with an (almost) quantized conductance.

To conclude, the QSH state is essentially two copies of the QAH state. Reciprocally, the QAH state is half the QSH state: while the QAH effect inspired the theoretical prediction and experimental discovery of the QSH state, the realization of the QSH state led to the experimental discovery of the QAH state [Chang13]. The idea [Qi06, Yu10] is rather simple. By combining the strong SOC present in QSH insulators with ferromagnetism we may suppress one spin component from the edge and naturally end up with a QAH state. Chang *et al.* reported the observation of the QAH in chromium doped thin films of $(Bi,Sb)_2Te_3$.

## 2.2 Topological protection of edge states

It was realized early on that the quantization of the IQH conductance can be explained by a topological property of the groundstate wavefunction. Thouless *et al.* [Thouless82] wrote the Kubo formula for the Hall conductance $\sigma_{xy}$ in terms of an integral of the variation of the phase of Bloch wavefunctions along the boundary of the Brillouin zone; the famous TKNN invariant. Since the phase can only change by an integer multiple $\nu$ of $2\pi$, the quantization $\sigma_{xy} = \nu e^2/h$ follows. This argument is only valid in the presence of a gap in the spectrum, so that each band is either fully occupied or fully empty. Soon afterwards [Avron83], it was realized that the TKNN integral is invariant under smooth changes of the Hamiltonian that do not close the gap. No matter how much the occupied bands are mixed together by the deformation, the value of the invariant does not change. This is the key property of topological quantities. This already explains, to a certain extent, the robustness of the quantization of the Hall conductivity.

There is a deep principle that connects the topological properties of a given material to the occurence of edge states at its boundaries: the *bulk-boundary correspondence*. One of the early example are solitons in polyacetylene [Su79]. More important for us, the gapless edge states of the quantum Hall effects can be understood similarly. An intuitive way to understand this concept is semi-classical: imagine a boundary that separates two regions characterized by a different topological number. Going smoothly from one region to the other, the topological number has to jump along the way; but this is impossible unless the gap closes, i.e. there must be a gapless excitation somewhere near the boundary that connects the two regions. In fact, this argument hints that we expect to find gapless excitations near all topological defects, be it the surface of a topologically nontrivial material (=interface with the trivial vacuum), or, say, a vortex in a topological superconductor. The argument can be formalized in some cases by an index theorem, see e.g. [Volovik03].

The recent burst of research in topological insulators can be conceptually attributed to a refinement of the topological characterization of electronic states in different symmetry classes. The TKNN invariant of the IQH state does not require any symmetry of the system. For QSH states however, it is clear that time-reversal invariance plays a crucial role. It is therefore meaningful to investigate what kinds of topological invariants can be defined when nontrivial symmetries are present. We proceed to illustrate these ideas with a one-dimensional toy model.

### 2.2.1 A toy model to illustrate bulk-boundary correspondence

One could argue that the first manifestation of the bulk-boundary correspondence goes back to the year 1939 [Shockley39]. In this work, Shockley showed that if the bulk energy bands of a crystal have "crossed" there are surface states at the boundary of the material. More precisely, he considered the problem of electrons in a one-dimensional periodic potential due to a chain of atoms spaced with a lattice constant $a$. He first considers widely separated atoms $a \to \infty$ for which the energy levels of electrons are simply the atomic orbitals. By bringing the atoms closer and closer energy bands start to form. By further reducing the lattice constant the bandwidths grow and at some critical value $a_1$ two bands touch each other. Continuing the process, a gap between the two bands reopens but two edge states (one at each boundary, neglecting spin) remain in the middle of the gap.

To derive this result, Shockley made two assumptions about symmetries of the system. First, time-reversal symmetry is not broken. Second, the crystal is centro-symmetric and thus there is a global parity symmetry. We now want to consider a simple effective tight-binding two-band model with these symmetries. The general Hamiltonian in $k$-space reads $H(k) = \epsilon(k) + (\Delta + 2t\cos k)\sigma_z + \lambda \sin k\, \sigma_y$, where the $\sigma$ matrices are in band space (we neglect spin here as it does not play an essential role). To simplify the discussion we neglect the band-independent term $\epsilon(k)$ and obtain

$$H(k) = (\Delta + 2t\cos k)\sigma_z + \lambda \sin k\, \sigma_y\,. \tag{2.7}$$

This simple Hamiltonian has the additional chiral symmetry $\sigma_x H \sigma_x = -H$. The spectrum is therefore symmetric around zero energy and reads $E(k) = \pm\sqrt{(\Delta + 2t\cos k)^2 + (\lambda \sin k)^2}$. The analogue of Shockley's procedure of starting with a large lattice constant is starting with very small hopping terms $t, \lambda \to 0$. As the atoms are brought together, the hopping terms grow and at the critical value $\Delta = 2t$ the bands touch at $k = \pi$. For $\Delta < 2t$ the

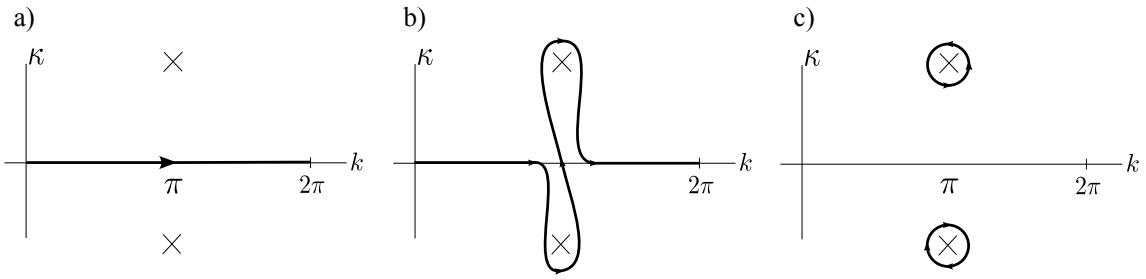


Figure 2.3: (a) trivial integration contour to calculate the winding number $w$, see Eq. (2.13) of the current topological state. The crosses mark the degeneracy points of the Hamiltonian in complex $k$-space. (b) integration contour to calculate the winding number of the topological state $w_i$ after a band crossing (c) difference of winding numbers $w - w_i$ between the current topological state and topological state after a band crossing. The whole contribution comes from singularities at the degeneracy points where the edge states lie.

bands have crossed and a gap reopens if $\lambda \neq 0$. The two questions we want to answer here are: (1) How can we associate a topological invariant to this band crossing? (2) How can we relate this topological property to the presence of edge states?

Logically, we start by answering a third question: (3) Why is there an edge state after the band crossing? By definition, edge states must decay in the bulk and, in the presence of translation symmetry, they are characterized by a complex wave number $\tilde{k} = k + i\kappa$. It is therefore natural to study the analytical structure of the Hamiltonian in the complex plane. The main interesting feature of $H(\tilde{k})$ is the appearance of degeneracy points that occur in pairs at $\tilde{k}_0 = k_0 + i\kappa_0$ and at the complex conjugate $\tilde{k}_0^*$ for which $E(\tilde{k}_0) = 0$. At these points, the Hamiltonian takes the form $H(\tilde{k}_0) \propto (\sigma_z \pm i\sigma_y)$. Crucially, which sign $(\pm)$ is realized depends both on the sign of $\Delta - 2t$ and on the sign of $\kappa_0$. We obtain

$$H(\tilde{k}_0) = \lambda \sin \tilde{k}_0 (\sigma_z + i\,\mathrm{sgn}(\kappa_0)\mathrm{sgn}(\Delta - 2t)\sigma_y)\,. \tag{2.8}$$

The corresponding zero-energy eigenstates are given by

$$\psi(x) = \begin{pmatrix} 1 \\ -\mathrm{sgn}(\kappa_0)\mathrm{sgn}(\Delta - 2t) \end{pmatrix} \exp(ik_0 x) \exp(-\kappa_0 x)\,. \tag{2.9}$$

We now consider two regions separated by a sharp domain wall at $x = 0$ described by the Hamiltonian (2.7) with parameters $\Delta^L, t^L, \lambda^L$ for $x < 0$, and $\Delta^R, t^R, \lambda^R$ for $x > 0$. To find a normalizable bound state at the interface between two regions, we must require that $\mathrm{sgn}(\kappa_0^L) = -1$ in the left region $\mathrm{sgn}(\kappa_0^R) = 1$ in the right region. Moreover, the continuity of the wavefunction requires $\mathrm{sgn}(\kappa_0^L)\mathrm{sgn}(\Delta^L - 2t^L) = \mathrm{sgn}(\kappa_0^R)\mathrm{sgn}(\Delta^R - 2t^R)$. If follows from these considerations that there is a bound state if the equation

$$\mathrm{sgn}(\Delta^L - 2t^L) = -\mathrm{sgn}(\Delta^R - 2t^R) \tag{2.10}$$

holds. In other words, there is a bound state at the interface of a material with crossed bands and a material with uncrossed bands (*e.g.* the vacuum). This answers question (3).

At this point, there is a clear connection between edge states and bulk band crossing. We would now like to make a further connection between the edge states to a

bulk topological invariant. To this end, consider the matrix $U(k)$ that diagonalizes $H(k)$: $H(k) = E(k)U(k)\sigma_z U^\dagger(k)$. Because of the symmetries of the Hamiltonian we can parametrize $U(k)$ with a single real parameter $\theta(k)$

$$U(k) = \exp(i\frac{\theta(k)}{2}\sigma_x)\,. \tag{2.11}$$

Since the overall phase of $U(k)$ is not physically relevant we identify $\theta + 2\pi \equiv \theta$. Up to this equivalence, we also have the periodicity $\theta(k + 2\pi) = \theta(k)$ due to the periodicity of the Hamiltonian. The set of all possible $U(k)$ is thus equivalent to the set of all periodic functions over the circle. The latter can be easily classified by their winding number $w \in \mathbb{Z}$. This leads us to consider the bulk topological invariant

$$w = \int_{\text{B.Z.}} \frac{dk}{2\pi}\,\frac{d\theta}{dk}\,. \tag{2.12}$$

It is possible to give an equivalent definition that does not involve $\theta(k)$

$$w = \int_{\text{B.Z.}} \frac{dk}{2\pi i}\,\text{Tr}\left(U(k)^{-1}\sigma_x\frac{dU}{dk}\right)\,. \tag{2.13}$$

For the Hamiltonian 2.7 an explicit computation of the winding number yields $w = 0$ for the uncrossed bands case ($\Delta > 2t$) and $w = 1$ for the crossed bands case ($\Delta < 2t$). This answers question (1).

To make the bulk-boundary correspondence even more manifest, we again consider complex wave numbers $\tilde{k}$. This allows us to deform the integration contour in Eq. (2.13) in the complex plane. At the degeneracy points $\tilde{k}_0$, the matrix $U(\tilde{k})$ is ill-defined. By going around the degeneracy points, see Fig. 2.3b, we can compute the winding number after a band crossing. Due to the degeneracy points we cannot deform continuously the contour (a) to the contour (b). The difference in winding numbers after a band crossing originates from the degeneracy points alone, see Fig. 2.3c. Now, there is an bound state at the interface between two regions only when the bands have crossed in one region and not in the other, this is Eq. (2.10). But as we have just seen a band crossing necessarily comes with the associated topological charge of the degeneracies; the presence of a bound state and winding number difference go hand in hand. This is a very clear manifestation of the bulk-boundary correspondence and an answer to question (2).

We now want to take advantage of the power of topological considerations to find explicit edge states for different values of the winding number. First, we take the Hamiltonian (2.7) for a finite chain of length $N$ and choose the parameters $2t = w$, $\Delta = 0$. This is a perfectly valid representative of the class of parameters for which $w = 1$. The surprise come if we go back to the real space representation, in which the tight-binding Hamiltonian reads

$$H = -2t\sum_{i=1}^{N} a_i^\dagger(\sigma_z - i\sigma_y)a_{i+1} + a_{i+1}^\dagger(\sigma_z + i\sigma_y)a_i\,., \tag{2.14}$$

where $a_i$ is a vector of two annihilation operators of electrons on site $i$ for the two bands. Since $\sigma_z \pm i\sigma_y$ act as ladder operators for $\sigma_x$ we find that the state on the first lattice

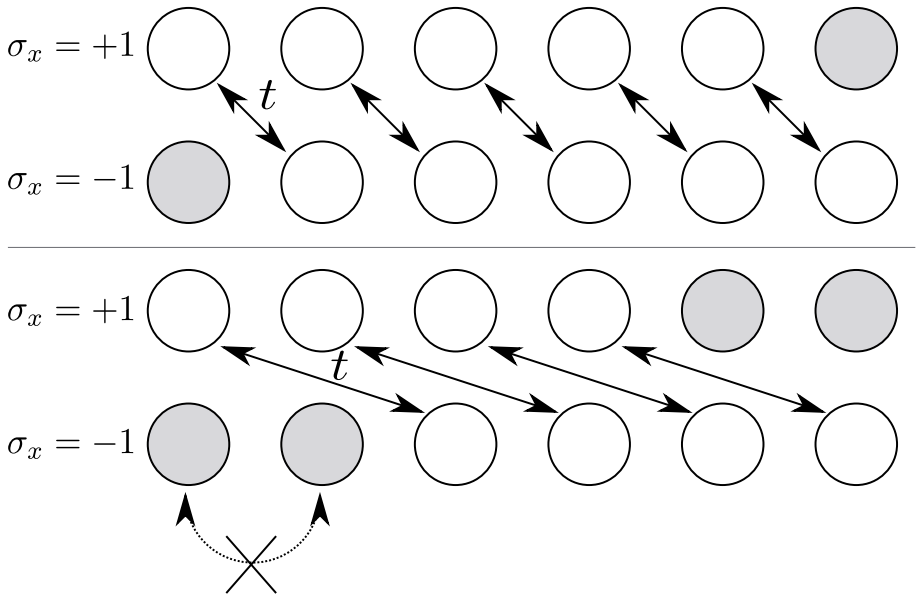


Figure 2.4: *Top panel*: real space picture of a representative of the $w = 1$ topological phase of the Hamiltonian given by (2.7) for $\Delta = 0, w = 2t$. Each site of the chain hosts two electronic states for which $\sigma_x = \pm 1$ respectively. The grayed leftmost state with $\sigma_x = -1$ and rightmost state with $\sigma_y = 1$ are fully uncoupled from the rest of the chain and are eigenstates with zero energy. The remaining states have energy $\pm 2t$. There are thus two midgap edge states in this phase. *Bottom panel*: representative of the $w = 2$ topological phase that can be obtained by doubling $k \to 2k$ and setting $\Delta = 0, w = 2t$ in the Hamiltonian (2.7). There are four edge states (grayed circles) uncoupled from the rest of the chain. Any coupling between neighbouring edge states is forbidden by the chiral symmetry.

site with $\sigma_x = -1$ and the state of the last lattice site with $\sigma_x = +1$ do not enter the Hamiltonian at all: they are the two zero energy edge states, see the top panel of Fig. 2.4. The rest of the states are coupled in pairs and have energy $\pm 2t$. Similarly, we can check that a finite chain with $w = 2$ has four edge states, see the bottom panel of Fig. 2.4.

**The role of symmetry**

The winding number defined by Eq. (2.13) is quantized (it takes only integer values) which makes it unsensitive to continuous changes in the Hamiltonian as long as the gap does not close. However, the topological invariant itself is symmetry protected; breaking the symmetries of the Hamiltonian also breaks the quantization of the winding number. If we allow for chirality breaking terms proportional to $\sigma_x$ in the Hamiltonian we must also enlarge the group of matrices $U(k)$ necessary to diagonalize $H(k)$. This opens up the possibility of continuously interpolating between, say, $w = 0$ and $w = 2$ without closing the gap. For instance, the two edge states at the bottom of Fig. 2.4 would couple by the $\sigma_x$ term and go away from zero energy.

#### Topological invariant and homotopy group

More formally, running over the one-dimensional Brillouin zone from $k = 0$ to $k = 2\pi$ naturally defines a loop $U(k)$ in the group $G$ of matrices $U$. For our purposes, the homotopy group $\pi_1(G)$ lists all the different loops that cannot be smoothly deformed into each other. For instance, with the Hamiltonian defined by Eq. (2.7) we had $G = O(2)$. The winding number we have chosen is an element of the homotopy group $\pi_1(O(2)) = \mathbb{Z}$; hence the quantization of $w$. If $\pi_1(G)$ is trivial then it is not possible to define a useful topological invariant for the system in this way. The symmetries of the Hamiltonian define which group $G$ is relevant.

### 2.2.2 Topological classification of Hamiltonians of free fermions

Remarkably, a full classification of topological of Hamiltonians of free fermions has been obtained [Schnyder08, Ryu09, Kitaev09]. It is well beyond the scope of this thesis to go into the details that allowed this achievement; we direct the interested reader to the review [Budich13]. Nevertheless, we would like to describe the result of the classification itself. To this end, we start with a brief explanation of the relevant symmetries that underpin the topological classification.

#### Altland-Zirnbauer symmetry classes

First, symmetries with a unitary representation in the Hilbert space are irrelevant to the classification. The reason is that the Hamiltonian can then be block diagonalized into sectors of the Hilbert space with no trace of the original symmetry, up to the degeneracy. Each block can be subsequently separately classified.

On the other hand, time-reversal symmetry (TRS) and particle-hole symmetry (PHS) are represented by antiunitary operators $\Theta = T\mathcal{K}$ and $\Xi = P\mathcal{K}$ respectively, where $T, P$ are unitary operators and $\mathcal{K}$ denotes complex conjugation; the Hamiltonian satisfies $T^\dagger H^* T = H$ and $P^\dagger H^* P = -H$. These symmetries impose nontrivial reality conditions on the Hamiltonian. Moreover, the operators can square to either $\pm 1$. As a result, we can already distinguish between nine classes for which $T^2 = -1, 0, 1$ and $P^2 = -1, 0, 1$, where 0 denotes the absence of the symmetry.

If there are two time-reversal-like symmetries $\Theta_1, \Theta_2$, we can define a unitary symmetry operator $A = \Theta_1\Theta_2$. We may therefore again block diagonalize the Hamiltonian and treat each block separately. It is therefore enough to consider system with one or zero TRS; the same goes for PHS. In the presence of both TRS and PHS we can again take the product $S = \Theta\Xi$ which defines a unitary operator. However, the Hamiltonian anticommutes with $S$, $S^\dagger H S = -H$; we cannot simply block diagonalize $H$ in this case. Such a symmetry is called chiral symmetry (CS) (or sublattice symmetry in connection to bipartite lattice models). While the existence of a CS is fully determined by TRS and PHS when at least one of them is realized, a CS may or may not be present when the system has neither a TRS, nor a PHS. This is the tenth class of the Altland-Zirnbauer classification scheme [Altland97], see the first four columns of Tab. 2.1.

**Periodic table of topological insulators**

For each of the symmetry class in the Altland-Zirnbauer classification and for every spatial dimension $d$ we can ask how many topologically distinct gapped Hamiltonians are there, and what kind of topological invariant we can define. With our toy model of Sec. 2.2.1 we have filled one square of the table by associating a winding number $w \in \mathbb{Z}$ for 1D systems in the presence of TRS (+1), PHS (+1), and CS, i.e. of class BDI. The 2D IQH and AQH effect belong to class A (no symmetry) and are characterized by the first Chern number $\mathcal{C}_1 \in \mathbb{Z}$. The full classification of free fermionic Hamiltonians, shown in Tab. 2.1, was recently obtained in Ref. [Schnyder08, Ryu09, Kitaev09].

| AZ | TRS | PHS | CS | $d=0$ | 1 | 2 | 3 | 4 | 5 | 6 | 7 |
|---|---|---|---|---|---|---|---|---|---|---|---|
| A | 0 | 0 | 0 | $\mathbb{Z}$ | 0 | $\mathbb{Z}$ | 0 | $\mathbb{Z}$ | 0 | $\mathbb{Z}$ | 0 |
| AIII | 0 | 0 | 1 | 0 | $\mathbb{Z}$ | 0 | $\mathbb{Z}$ | 0 | $\mathbb{Z}$ | 0 | $\mathbb{Z}$ |
| AI | 1 | 0 | 0 | $\mathbb{Z}$ | 0 | 0 | 0 | $\mathbb{Z}$ | 0 | $\mathbb{Z}_2$ | $\mathbb{Z}_2$ |
| BDI | 1 | 1 | 1 | $\mathbb{Z}_2$ | $\mathbb{Z}$ | 0 | 0 | 0 | $\mathbb{Z}$ | 0 | $\mathbb{Z}_2$ |
| D | 0 | 1 | 0 | $\mathbb{Z}_2$ | $\mathbb{Z}_2$ | $\mathbb{Z}$ | 0 | 0 | 0 | $\mathbb{Z}$ | 0 |
| DIII | -1 | 1 | 1 | 0 | $\mathbb{Z}_2$ | $\mathbb{Z}_2$ | $\mathbb{Z}$ | 0 | 0 | 0 | $\mathbb{Z}$ |
| AII | -1 | 0 | 0 | $\mathbb{Z}$ | 0 | $\mathbb{Z}_2$ | $\mathbb{Z}_2$ | $\mathbb{Z}$ | 0 | 0 | 0 |
| CII | -1 | -1 | 1 | 0 | $\mathbb{Z}$ | 0 | $\mathbb{Z}_2$ | $\mathbb{Z}_2$ | $\mathbb{Z}$ | 0 | 0 |
| C | 0 | -1 | 0 | 0 | 0 | $\mathbb{Z}$ | 0 | $\mathbb{Z}_2$ | $\mathbb{Z}_2$ | $\mathbb{Z}$ | 0 |
| CI | 1 | -1 | 1 | 0 | 0 | 0 | $\mathbb{Z}$ | 0 | $\mathbb{Z}_2$ | $\mathbb{Z}_2$ | $\mathbb{Z}$ |

Table 2.1: Periodic table of topological insulators and superconductors [Schnyder08, Ryu09]. The first two rows have a periodicity of period 2, the eight bottom rows have a period 8; this is known as Bott periodicity in K-theory [Kitaev09].

### 2.2.3 2D topological insulators

The QSH effect introduced previously has a true quantized spin Hall conductivity only if the spin component $S_z$ is conserved. According to our discussion on topological classification, such a unitary symmetry is irrelevant and we should characterize each sector $S_z = \pm 1$ separately. Each sector belongs to the Altland-Zirnbauer class A and is thus characterized by an integer topological invariant like the IQH or QAH effects. However, physical perturbations such as a Rashba spin-orbit coupling will break this symmetry an destroy the spin Hall conductivity quantization. Kane and Mele showed [Kane05a] that the gapless edge states persist even in that case. Moreover, in a parallel work [Kane05b], they connected this robustness to a nontrivial $\mathbb{Z}_2$ topological invariant (the system is in the symmetry class AII). This invariant defines 2D topological inslulators as a slight generalization of the QSH effect.

At low energies, the gapless helical states at the edge of 2D topological insulators can be described by the Hamiltonian

$$H = \int dx \sum_{\alpha=\pm} \psi_\alpha^\dagger(x)(-i\alpha v_F \partial_x - \mu)\psi_\alpha(x) \tag{2.15}$$

where $\alpha = \pm 1$ for right and left moving electrons. The existence of these states is protected by TRS and topology; the Kramers degeneracy forbids backscattering even in the presence of moderate disorder that does not close the bulk gap. Unlike in the IQH effect, however, interactions can lead to inelastic backscattering [Kane05a, Schmidt12] and thereby reduce the conductance at finite temperatures. Moreover, strong interactions even lead to localization of the edge states [Wu06, Xu06].

### 2.2.4 3D topological insulators

A generalization of the $\mathbb{Z}_2$ topological number of 2D topological insulators to gapped 3D systems in class AII followed soon afterwards [Fu07, Moore07, Roy09]. The result is that such systems are characterized by 4 $\mathbb{Z}_2$ invariants. Three of them correspond to stacking 2D topological insulators in the 3 axes and are not robust to disorder; the edge states becomes gapped by a coupling between neighbouring Kramers partners. The fourth one is nontrivial and defines strong 3D topological insulators.

Similarly to the 2D topological insulators, 3D topological insulators support gapless electronic states on their boundary. The surface states of 3D topological insulators are described by the 2D massless Dirac Hamiltonian

$$H = \int d^2x \; \psi^\dagger(\boldsymbol{x}) \left(-iv_F \boldsymbol{\sigma} \cdot \nabla - \mu\right) \psi(\boldsymbol{x}), \tag{2.16}$$

where the Pauli matrices $\boldsymbol{\sigma}$ are related to the spin $\boldsymbol{S}$ of electrons. If the surface has a mirror plane symmetry, then $\boldsymbol{S} = \hat{z} \times \boldsymbol{\sigma}/2$. The eigenstates of this Hamiltonian display spin-momentum locking; the spin is entirely fixed by the direction of propagation and vice-versa.

Dirac electrons display a weak antilocalization effect: whereas backscattering is enhanced due to constructive interferences between time-reversed processes in conventional systems, direct backscattering is forbidden for Dirac electrons due to destructive interferences between time-reversed processes. The reason for this is that Dirac electrons pick up a $\pi$ phase shift upon a full rotation in $k$-space. This Berry phase is due to the spin-momentum locking. As a striking consequence, these surface Dirac electrons remain gapless even in the presence of disorder [Nomura07]. We direct the reader to Ref. [Bardarson13] for a recent review of transport properties of these surface states.

Another interesting consequence of the $\pi$ Berry phase is the modification of the quantization condition of cyclotron orbits in the presence of a perpendicular magnetic field. This leads to a modified spectrum of Landau levels

$$E_N = \omega_c \sqrt{N + \left(\frac{g\mu_B B}{2\omega_c}\right)^2}, \tag{2.17}$$

where $\omega_c$ is the cyclotron frequency. Neglecting the Zeeman splitting, the Landau level $N = 0$ has zero energy. This Landau level structure was confirmed experimentally in $Bi_2Se_3$ [Cheng10, Hanaguri10].

## 2.3 Majorana fermions

We now turn to the description of the topologically protected gapless edge states of topological superconductors. We start with some very general considerations on excitations of superconductors. We describe a superconductor with the Boliubov-de Gennes formalism in which the Hamiltonian reads

$$H_{\mathrm{BdG}} = \frac{1}{2}\int dx\ \Psi^\dagger(x) \begin{pmatrix} H_0 - \mu & \Delta \\ \Delta^\dagger & \mu - \Theta H_0 \Theta^\dagger \end{pmatrix} \Psi(x)\,, \tag{2.18}$$

where $H_0$ is a normal Hamiltonian for electrons, $\Delta$ is the superconducting pairing term, $\Theta$ is the time-reversal operator, and the field operator $\Psi = (\psi_\uparrow, \psi_\downarrow, \psi_\downarrow^\dagger, -\psi_\uparrow^\dagger)^T$. The formalism has a built-in PHS $\Xi = \tau_y\sigma_y\mathcal{K}$, which is an artifact of the formalism introduced to reduce the Hamiltonian to a noninteracting form. The consequence is that all the eigenstates and eigenenergies are doubled: to a solution $\chi = (u_\uparrow, u_\downarrow, v_\uparrow, v_\downarrow)^T$, $\mathcal{H}_{\mathrm{BdG}}\chi = E\chi$, corresponds the eigenstate $\chi' = \Xi\gamma = (-v_\downarrow^*, v_\uparrow^*, u_\downarrow^*, -u_\uparrow^*)^T$ of opposite energy $\mathcal{H}_{\mathrm{BdG}}\chi' = -E\chi'$. This doubling is unphysical, and in practice we remove eigenstates of negative energy to avoid double counting. There is an important catch: what happens if an eigenstate has *exactly* zero energy? The question is especially relevant in the context of topologically protected edge states since we expect to find a *gapless* excitation at the boundary of the system. The answer is: it depends.

First, we consider an ordinary $s$-wave pairing term and an Hamiltonian $H_0$ without spin-orbit coupling. In that case, the Bogoliubov quasiparticles have a definite spin and have the form $\chi = (u, 0, v, 0)$ so that $\chi' = \Xi\chi \neq \chi$. In that case we can safely disregard either $\chi$ or $\chi'$ to avoid double counting.

Second, we consider either an $s$-wave pairing term with a spin-orbit coupled $H_0$, or an unconventional pairing term. The Bogoliubov quasiparticles no longer have a definite spin. This opens up the possibility of having a solution of the form $\chi = (u_\uparrow, u_\downarrow, u_\downarrow^*, -u_\uparrow^*)$ such that $\chi = \Xi\chi = \chi'$. We cannot remove one of two states, for there is only one! Note that such a state necessarily has zero energy. These types of states are the one of interest in this section; they are the edge states of topological superconductors.

### Majorana bound states

The quasiparticle annihilation operator $\gamma$ associated to a particle-hole invariant state satisfies $\gamma^\dagger = \gamma$. This is the key property of the so-called Majorana fermions, named in honor of Ettore Majorana who first proposed them as potential fundamental particles. We would now like to consider such Majorana fermions more formally.

A set $\gamma_i$, $1 \leq i \leq N$, of zero-dimensional Majorana fermions, or Majorana bound states (MBSs), satisfy the following relations

$$\gamma_i^\dagger = \gamma_i\,, \tag{2.19}$$

$$[H, \gamma_i] = 0\,, \tag{2.20}$$

$$\{\gamma_i, \gamma_j\} = \delta_{ij}\,. \tag{2.21}$$

The first equation states that a Majorana fermion is its own antiparticle. Since we want the MBSs to be eigenstates of the system the second equation is a consequence of the

first one. As an important consequence the presence of MBSs is always associated to a groundstate degeneracy. The third relation reflects the Fermi-Dirac statistics of MBSs.

There are a number of conceptual difficulties arising from the defining relations of MBSs. The first is the necessity to abandon the notion of an occupation number of a MBS. In fact the naive attempt fails miserably: the potential occupation number operator $n_i = \gamma_i^\dagger \gamma_i = 1/2$ is trivial. Alternatively some people say that MBSs are always *half*-occupied; this is not helpful in any way. It is much more fruitful to connect the MBSs to a groundstate degeneracy and see the operators $\gamma_i$ as operators switching between two states. It is however possible to recover a complex fermion operator $c$ out of a pair of MBSs by defining

$$c = \frac{\gamma_1 + i\gamma_2}{\sqrt{2}}\,, \tag{2.22}$$

that satisfies the usual commutation relations $c^2 = (c^\dagger)^2 = 0$ and $\{c, c^\dagger\} = 1$. Therefore a *pair* of Majorana fermions is connected to a two-fold groundstate degeneracy. With $N$ MBSs the groundstate manifold thus has a dimension $2^{(N/2)}$.

### 2.3.1 Kitaev chain

Kitaev [Kitaev01] proposed a simple toy-model of a spinless one-dimensional $p$+i$p$ superconductor (AZ class D) that has Majorana bound states at its ends when it is in the topologically nontrivial phase. We briefly review the model to explicitly show how Majorana fermions can arise in condensed matter systems.

Without further ado, the Hamiltonian is

$$H = \sum_j -w(a_j^\dagger a_{j+1} + a_{j+1}^\dagger a_j) - \mu\left(a_j^\dagger a_j - \frac{1}{2}\right) + \Delta a_j a_{j+1} + \Delta^* a_{j+1}^\dagger a_j^\dagger\,. \tag{2.23}$$

To diagonalize the Hamiltonian we introduce the equivalent of Nambu spinors $(a_k\ a_{-k}^\dagger)^T$. The doubled spectrum is $E(k) = \pm\sqrt{(\mu + 2w\cos k)^2 + 4|\Delta|^2 \sin^2 k}$. The gap closes when $|\mu| = |2w|$. For $|2w| < |\mu|$, the system is in a topologically trivial state because it is continuously connected to a trivial insulator with $\Delta = 0$. On the other hand, we can access the topological features (if they exist) of the $|2w| > |\mu|$ phase by considering the limiting case $\mu = 0, \Delta = w$. In that case, we obtain

$$H = -w\sum_j (a_j^\dagger - a_j)(a_{j+1} + a_{j+1}^\dagger)\,. \tag{2.24}$$

The terms that appear in the sum can be conveniently rewritten by defining two Majorana operators per site

$$\gamma_j^{(1)} = \frac{a_j^\dagger + a_j}{\sqrt{2}} \tag{2.25}$$

$$\gamma_j^{(2)} = i\frac{a_j^\dagger - a_j}{\sqrt{2}}\,, \tag{2.26}$$

which satisfy the reality condition $\gamma_j^{(l)\dagger} = \gamma_j^{(l)}$ and the commutation relations $\{\gamma_i^{(l)}, \gamma_j^{(m)}\} = \delta_{ij}\delta_{ml}$. In this representation, the Hamiltonian reads

$$H = 2iw \sum_j \gamma_j^{(2)} \gamma_{j+1}^{(1)} \,. \tag{2.27}$$

The two Majorana operators $\gamma_1^{(1)}$ and $\gamma_N^{(2)}$ are left uncoupled and therefore commute with the Hamiltonian. As such they are true Majorana bound states. They imply a ground state degeneracy.

The situation is very reminiscent of our toy model of Sec. 2.2.1, see Fig. 2.4. In fact, the analogy can be made precise by replacing the chiral symmetry operator $\sigma_x$ of the toy model with the operator $\tau_x$ that exchanges $a_j^\dagger \leftrightarrow a_j$ in the Kitaev model. However, $\tau_x$ is only a symmetry for special points of parameter space, such as in Eq. (2.27), but it is not a symmetry of the whole model (2.23). Specifically, we cannot have a pair MBSs $\gamma_a, \gamma_b$ at one edge, like we had on the bottom panel of Fig. 2.4, since they will generically be coupled by a term $i\gamma_a\gamma_b$. As a consequence, the topological state of the Kitaev model cannot be described by an integer $w \in \mathbb{Z}$ topological invariant. The relevant quantity is the *parity* of the "number of edge states". To see this, consider a Hamiltonian for $M$ Majorana modes $H = i\sum_{i,j=1}^{M} \gamma_i h_{ij} \gamma_j$. The matrix $h_{ij}$ must be antisymmetric to ensure $H = H^\dagger$. Now, if $M$ is odd $\det h = 0$ and thus $h_{ij}$ must have a zero-energy eigenstate. Because of particle-hole symmetry, a zero-energy eigenstate is a Majorana fermion in the spinless case. On the other hand, if $M$ is even no such constraint exists and in principle no MBS remains. This explains intuitively why the topological phase is characterized by a $\mathbb{Z}_2$ invariant in Hamiltonians in the AZ symmetry class D. Kitaev [Kitaev01] gave an explicit expression for the invariant, the "Majorana number" $\mathcal{M}$, even in the case of a disordered wire. In the clean case and for small pairing amplitude $\Delta \ll t$, the invariant is given by the parity of the number of Fermi points ($E(k) = 0$) in half of the Brillouin zone $k \in [0, \pi]$.

### 2.3.2 Majorana edge states

Gapless excitations of 2D topological superconductors are described by Majorana edge states rather than MBSs. Therefore, we now consider an one-dimensional massless Majorana mode along the $x$-axis. By definition, it satisfies the Majorana condition

$$\gamma(x)^\dagger = \gamma(x) \tag{2.28}$$

along with the commutation relations

$$\{\gamma(x), \gamma(y)\} = \delta(x - y) \,. \tag{2.29}$$

The Hamiltonian is given by

$$H = -iv_M \int dx \; \gamma(x) \partial_x \gamma(x) \tag{2.30}$$

where $v_M$ is the propagation velocity. The Fourier modes $\gamma_k$ for $k \neq 0$ obey

$$\gamma_k^\dagger = \gamma_{-k}\,, \tag{2.31}$$

$$\{\gamma_k, \gamma_{k'}\} = 0\,, \tag{2.32}$$

$$\left\{\gamma_k^\dagger, \gamma_{k'}\right\} = \delta_{k,k'}\,. \tag{2.33}$$

Unlike for MBSs it is meaningful to define the occupation-number operators $n_k = \gamma_k^\dagger \gamma_k$; the Majorana condition only entails we must disregard the modes with $k < 0$ to avoid double counting. The $k = 0$ mode is special and its properties are much more akin to those of MBSs.

### 2.3.3 Engineering Majorana fermions in solid state systems

The ideal way to obtain Majorana quasiparticles in solid state systems would be to use materials that are intrinsic topological superconductors. Unfortunately, the list of potential candidates is rather short. The two most prominent ones are $Sr_2RuO_4$ and the Moore-Read state of the $\nu = 5/2$ fractional quantum Hall effect [Moore91] but a decisive experimental confirmation is still lacking.

Recently, many schemes have been put forward to engineer topological superconductors by inducing an effective $p$-wave pairing in strongly spin-orbit coupled materials via the proximity effect of an ordinary $s$-wave superconductor. A promising way to realize the 1D Kitaev chain uses a nanowire with strong Rashba spin-orbit coupling and large magnetic $g$-factor such as InAs or InSb covered by a superconductor and with a longitudinal magnetic field to access the topological phase [Lutchyn10, Oreg10]. Another possibility is to use the 1D helical electronic states at the edge of 2D topological insulators covered by a superconductor [Fu09a]. An additional insulating ferromagnet is required at the boundaries of the superconducting region to open a gap in the helical liquid. There are also similar proposals to realize effective 2D $p$-wave superconductors by again the proximity effect of an ordinary $s$-wave superconductor in the surface states of 3D topological insulators [Fu08]. This list is far from exhaustive and we direct the interested reader to the review articles [Beenakker13, Alicea12].

# Chapter 3

# Point contacts and localization in generic helical liquids

This chapter is adapted from the publication:

> C. P. Orth, G. Strübi, and T. L. Schmidt, *Point contacts and localization in generic helical liquids*, Phys. Rev. B **88**, 165315.

As we have seen in the previous chapter, two-dimensional topological insulators support gapless helical one-dimensional edge states. Due to time-reversal symmetry, the transport is expected to remain ballistic even in the presence of non-magnetic disorder.

Several physical mechanisms lead to deviations from these simple predictions: it was realized early on that interactions can cause inelastic two-particle backscattering, which is allowed by time-reversal invariance, and thus change the conductance at finite temperatures [Kane05a]. Strong interactions can even open a gap in the edge state spectrum [Xu06, Wu06]. Moreover, magnetic perturbations can lead to backscattering, and can thus affect the conductance [Maciejko09], or even cause localization [Delplace12].

If we consider a long and narrow two-dimensional topological insulator (length $L$, width $W \ll L$), backscattering between helical states on opposite edges may become possible without breaking time-reversal invariance. However, if $W$ is larger than the decay length of the edge states into the bulk the overlap between states on opposite edges is still exponentially suppressed. One way to produce backscattering is to couple the helical states on opposite edges by local tunneling [Ström09, Hou09, Teo09]. On the one hand, such processes may be realized intentionally at point contacts formed either by lithographic techniques or by appropriate gating [Liu08], depending on the topological insulator material, and interesting transport properties have been predicted [Liu11a, Schmidt11, Dolcini11, Lee12, Dolcetto12, Edge13]. On the other hand, tunneling between opposite edges may also emerge accidentally in narrow samples if the bulk material is sufficiently disordered, so that charge puddles [Skinner12, Väyrynen13] can connect opposite edges. As long as this transport remains elastic and the puddles are dilute, such a system can be modeled using local tunnel contacts at random positions and with random tunnel amplitudes.

## 3.1 Generic helical liquids

To investigate these systems, we are going to employ the concept of *generic* helical liquids proposed in Ref. [Schmidt12]. Such a generic helical liquid provides a rather general template for time-reversal invariant helical edge states in which the electron spin is not necessarily a good quantum number. This situation can arise in all proposed topological insulator materials to date by effects such as bulk inversion asymmetry, structural inversion asymmetry [Qi11], or Rashba spin-orbit coupling [Rothe10]. The most important consequence of the broken axial spin symmetry is a rotation of the spin quantization axis of the helical eigenstates as a function of momentum.

It was shown in Ref. [Schmidt12] that in this case, the projections of left-moving and right-moving eigenmodes on a fixed spin axis are determined by a momentum-dependent spin rotation matrix $B(k)$. Certain symmetries of the rotation matrix $B(k)$, which we refer to as the "spin texture" of the edge state, are fixed by unitarity and time-reversal invariance, but its amplitude can be tuned locally: for instance, in HgTe quantum wells, a spatially inhomogeneous electric field perpendicular to the plane of the topological insulator will induce Rashba spin-orbit coupling [Rothe10] with different amplitudes on different sample edges. In such an experiment, the spins of the helical states at the Fermi energy $\mu$ on opposite edges will be tilted relative to each other by an angle $\theta(\mu)$. In this chapter, we shall show that a nonzero $\theta(\mu)$ has a strong effect on the current-voltage characteristic.

Our starting point is two generic helical liquids with different spin rotation matrices $B_U(k)$ and $B_L(k)$ living on the upper and lower edges, respectively, of a narrow 2D topological insulator. We shall calculate two-terminal transport properties, where a bias voltage is applied between the left side and the right side of the sample as shown in Fig. 3.1. First, we shall investigate the effect of a single tunnel contact between the upper and lower edges, and show that tunneling can lead to forward scattering as well as backscattering depending on $\theta(\mu)$, see Fig. 3.1. Next, we shall add a second tunnel junction and show that interference effects make it possible to determine $\theta(\mu)$ from a conductance measurement. Finally, we shall consider a large number of random tunnel contacts. Even for conventional helical liquids where spin is conserved, this type of disorder leads to localization and to a suppression of the conductance $G \propto 2G_0 e^{-L/\ell}$, where $G_0 = e^2/h$ is the conductance quantum, $L$ is the sample length and $\ell$ is the localization length. For our model, we shall show that $\ell$ depends strongly on $\theta(\mu)$. Since $\theta(\mu)$ depends on the Rashba spin-orbit coupling strength, we predict that the localization length of a narrow two-dimensional topological insulator in a two-terminal configuration is strongly sensitive to a spatially inhomogeneous electric field.

We start by considering a single point contact between two helical edges along the $x$ direction. After linearizing the spectrum, the kinetic part of the Hamiltonian for the two edges is given by

$$H_{kin} = -iv_F \sum_{\eta=U,L} \sum_{\alpha=\pm} \alpha \int_{-\infty}^{\infty} dx\, \phi^\dagger_{\eta\alpha}(x) \partial_x \phi_{\eta\alpha}(x), \tag{3.1}$$

where $\eta$ labels the upper ($\eta = U$) and lower ($\eta = L$) edges, each of which hosts right-movers ($\alpha = +$) and left-movers ($\alpha = -$). In general, the eigenstates $\psi_{\eta\alpha}(k)$ of this Hamiltonian, where $k$ is the momentum along the $x$ direction, need not be spin eigenstates [Schmidt12]:

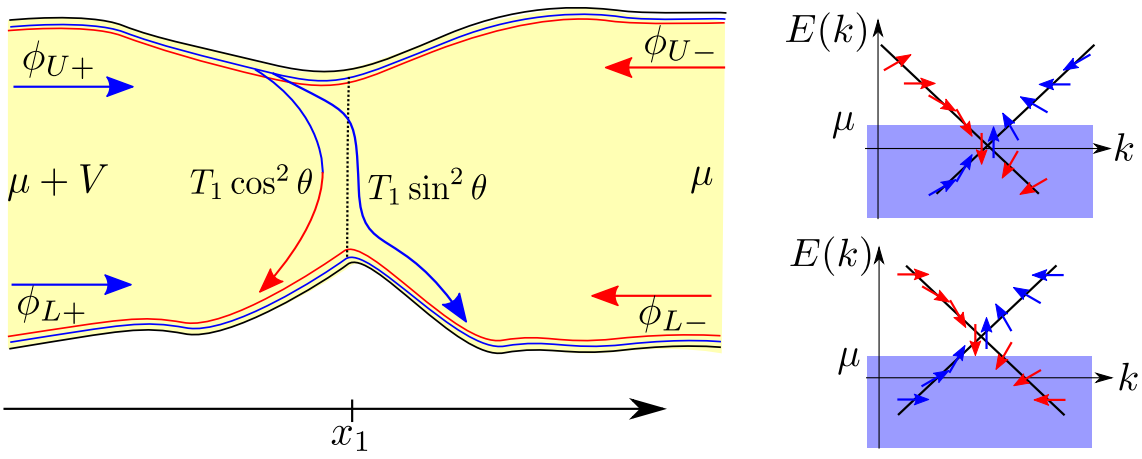


Figure 3.1: For a single point contact, the angle $\theta(\mu)$, see Eq. (3.24), determines the branching ratio of right movers on the upper edge into right- and left-movers on the lower edge. The right panel shows the spectra of the upper and lower edges for $V = 0$. $\theta(\mu)$ is given by the difference in spin axis rotation at the Fermi energy.

effects such as bulk inversion asymmetry, structural inversion asymmetry or Rashba spin-orbit coupling break the axial spin symmetry. The projections of the helical eigenstates $\phi_{\eta\alpha}(k)$ on states with definite spin along an arbitrary but fixed spin quantization axis, $\psi_{\eta\sigma}(k)$, can be encoded into a $2 \times 2$ momentum-dependent rotation matrix [Schmidt12]

$$\begin{pmatrix} \psi_{\eta\uparrow}(k) \\ \psi_{\eta\downarrow}(k) \end{pmatrix} = B_\eta(k) \begin{pmatrix} \phi_{\eta+}(k) \\ \phi_{\eta-}(k) \end{pmatrix}, \tag{3.2}$$

where $\eta = U, L$. The two rotation matrices $B_\eta(k)$ of the upper and lower edge are in principle independent of each other because the spatially separated edges can be subject to different gate voltages and Rashba spin-orbit coupling strengths. The resulting band structure is schematically shown in Fig. 3.1. Concrete expressions for $B_\eta(k)$ for helical edge states in HgTe/CdTe quantum wells in the presence of Rashba spin-orbit coupling where shown in Ref. [Schmidt12]. The matrices $B_\eta(k)$ are unitary, and as a consequence of time-reversal invariance, satisfy the condition $B_\eta(k) = B_\eta(-k)$.

$$B_\eta(k) = \begin{pmatrix} \cos(\theta_\eta(k)) & -\sin(\theta_\eta(k)) \\ \sin(\theta_\eta(k)) & \cos(\theta_\eta(k)) \end{pmatrix}, \tag{3.3}$$

where, according to Eq. (3.2), the angle $\theta_\eta(k)$, as a function of momentum $k$ and the edge $\eta$, determines the rotation of the spin quantization axis of the eigenstates of $H_0$, with respect to the fixed spin orientations $\uparrow, \downarrow$.

## 3.2 Solution to the tunneling problem

In this section we give a formal solution to the problem of helical edge states described by (3.1) in the presence of electron tunneling between the two edges. We model the

tunneling by the Hamiltonian

$$H_T = \int dx\, \psi^\dagger_{\eta'\sigma'}(x) T_{\eta'\sigma'\eta\sigma}(x) \psi_{\eta\sigma}(x)\,, \tag{3.4}$$

where a sum over repeated indices is implied (we use the summing convention throughout, unless otherwise specified). We assume spin-conserving tunneling, and we write $T(x) = \gamma(x)\tau^1$, where $\tau^1$ is the first Pauli matrix and acts on the edge space, and $\gamma(x)$ is a position dependent tunneling amplitude.

Dropping the indices for clarity, the full Hamiltonian in terms of the left and right moving fields reads

$$H = \int \frac{dk}{2\pi} vk\phi^\dagger(k)\sigma^3\phi(k) + \int \frac{dkdk'}{(2\pi)^2}\phi^\dagger(k)B^\dagger(k)T(k-k')B(k')\phi(k')\,, \tag{3.5}$$

where the $\sigma$ matrices act on the space of left/right movers.

### Quantum point contacts

We now specialize the form of the tunnel amplitude. We consider $N$ quantum point contacts at positions $x_i$ written as

$$T(x) = \sum_{i=1}^{N} \delta(x - x_i) T_i\,. \tag{3.6}$$

The tunneling Hamiltonian takes the form

$$H_T = \sum_i \int \frac{dk}{2\pi}\phi^\dagger(k)B^\dagger(k)e^{ikx_i}T_i \int \frac{dk'}{2\pi} e^{-ik'x_i}B(k')\phi(k')\,. \tag{3.7}$$

We want to find the eigenmodes of the form $\chi = \int \frac{dk}{2\pi} u^\dagger(k)\phi(k)$ which satisfy $[\chi, H] = E\chi$. This yields the equation for $u(k)$

$$(vk\sigma^3 - E)u(k) = -\sum_i e^{ikx_i}B^\dagger(k)T_i \int \frac{dk'}{2\pi} e^{-ik'x_i}B(k')u(k')\,. \tag{3.8}$$

We introduce the $k$ independent spinors

$$\xi_i = \int \frac{dk}{2\pi} e^{-ikx_i}B(k)u(k)\,, \tag{3.9}$$

which let us solve formally the equation for $u$

$$u_\xi(k) = u_h(k) - \sum_i e^{ikx_i}G(k)B^\dagger(k)T_i\xi_i\,, \tag{3.10}$$

where $u_h(k)$ is any solution to the homogeneous problem, and $G(k) = (vk\sigma^3 - E)^{-1}$ is the Green's function of the homogeneous problem. We have to regularize $G(k)$ around

$vk = \pm E$. Considerations on the boundary conditions in real space lead to the choice of the retarded Green's function

$$G(k) = \frac{1}{vk\sigma^3 - (E + i\delta)} = \frac{\sigma^3}{v}\frac{1}{k - \sigma^3(E + i\delta)/v} . \tag{3.11}$$

Substituting the solution (3.10) in the self-consistency condition (3.9) yields

$$\xi_i = \int \frac{dk}{2\pi} e^{-ikx_i} B(k) u_h(k) - \sum_j \int \frac{dk}{2\pi} e^{-ik(x_i - x_j)} B(k) G(k) B^\dagger(k) T_j \xi_j . \tag{3.12}$$

We introduce the matrix and spinor with QPC indices

$$Q_{ij} = \int \frac{dk}{2\pi} e^{-ik(x_i - x_j)} B(k) G(k) B^\dagger(k) , \tag{3.13}$$

$$\zeta_i = \int \frac{dk}{2\pi} e^{-ikx_i} B(k) u_h(k) = B(E/v) e^{-i\sigma^3 x_i E/v} u_0 , \tag{3.14}$$

where we wrote the solution to the homogeneous problem as $u_h(k) = 2\pi\delta(k - \sigma^3 E/v)u_0$. Using Eqs. (3.13, 3.14) we can solve the self-consistency equation by incorporating QPC indices in the matrix $T_{ij} = T_i\delta_{ij}$ (no sum):

$$\xi = (1 + QT)^{-1}\zeta . \tag{3.15}$$

And the formal solution for $u$ reads

$$u(k) = [2\pi\delta(k - \sigma^3 E/v) - \mathrm{Sum}_{\mathrm{QPC}}(e^{ikX} G(k) B^\dagger(k) T (1 + QT)^{-1} B(E/v) e^{-i\sigma^3 XE/v})] u_0 , \tag{3.16}$$

where we defined the QPC position matrix $X_{ij} = x_i\delta_{ij}$ (no sum), and $\mathrm{Sum}_{\mathrm{QPC}}$ denotes the sum over all matrix elements in QPC space, i.e. $\mathrm{Sum}_{\mathrm{QPC}}(A) = \sum_{i,j} A_{ij}$.

**Scattering matrix**

To determine the scattering matrix, we need to look at the real space dependence of the solution (3.16). In the Fourier transform, the $k$ integral singles out one pole of $G(k)$ determined by the sign of $x$ (asymptotically, i.e. for large $x$). We have

$$u(x) = e^{i\sigma^3 xE/v}\left[\mathbb{1} - \frac{i}{2v}(1 + \sigma^3 \mathrm{sign}(x))\mathrm{Sum}_{\mathrm{QPC}}(e^{i\sigma^3 XE/v} B^\dagger(\frac{E}{v}) T (1 + QT)^{-1} B(\frac{E}{v}) e^{-i\sigma^3 XE/v})\right] u_0 \tag{3.17}$$

For incoming states $(1 + \sigma^3 \mathrm{sign}(x)) = 0$, which means that the incoming states are simply given by $u(x) = e^{i\sigma^3 xE/v} u_0$. This is because we chose retarded boundary conditions for the Green's function. For the outgoing states we have $(1 + \sigma^3 \mathrm{sign}(x)) = 2$. The relation between output and input states is given by the scattering matrix

$$S = \mathbb{1} - \frac{i}{v}\mathrm{Sum}_{\mathrm{QPC}}(e^{i\sigma^3 XE/v} B^\dagger(E/v) T (1 + QT)^{-1} B(E/v) e^{-i\sigma^3 XE/v}) . \tag{3.18}$$

We now define the tunneling matrix in the rotated basis $\tilde{T} = e^{i\sigma^3 XE/v} B^\dagger(E/v) T B(E/v) e^{-i\sigma^3 XE/v}$ and similarly $\tilde{Q} = e^{i\sigma^3 XE/v} B^\dagger(E/v) Q B(E/v) e^{-i\sigma^3 XE/v}$. The scattering matrix now takes the rather simple form

$$S = \mathbb{1} - \frac{i}{v}\mathrm{Sum}_{\mathrm{QPC}}(\tilde{T}(1 + \tilde{Q}\tilde{T})^{-1}) . \tag{3.19}$$

This is the main result of this section.

We now compute the diagonal elements of the matrix $Q$

$$Q_{ii} = \int \frac{dk}{2\pi} B(k) G(k) B^\dagger(k) = \int \frac{dk}{2\pi} B(k) \frac{\sigma^3}{v} \frac{1}{k - \sigma^3(E+i\delta)/v} B^\dagger(k) \tag{3.20}$$

Using the symmetry $B(k) = B(-k)$ we may symmetrize the Green's function in the integrand $G(k) \to \frac{1}{2}(G(k) + G(-k))$. This allows us to compute

$$\begin{aligned} Q_{ii} &= \int \frac{dk}{2\pi} B(k) \frac{\sigma^3}{2v} \left( \frac{1}{k - \sigma^3(E+i\delta)/v} + \frac{1}{-k - \sigma^3(E+i\delta)/v} \right) B^\dagger(k) \\ &= \int \frac{dk}{2\pi} B(k) \frac{\sigma^3}{2v} \frac{2\sigma^3(E+i\delta)}{(k - \sigma^3(E+i\delta)/v)(k + \sigma^3(E+i\delta)/v)} B^\dagger(k) \\ &= \int \frac{dk}{2\pi} B(k) \frac{1}{2v} \frac{2(E+i\delta)}{(k - (E+i\delta)/v)(k + (E+i\delta)/v)} B^\dagger(k) \\ &= \int \frac{dk}{2\pi} \frac{1}{2v} \frac{2(E+i\delta)}{(k - (E+i\delta)/v)(k + (E+i\delta)/v)} \\ &= \frac{i}{2v} \end{aligned} \tag{3.21}$$

This remarkably simple result is largely due to the trivial matrix structure of the $k$-symmetrized Green's function.

The $k$ dependence of the spin rotation matrix $B(k)$ naturally defines a spin-rotation length $1/k_0$ in real space. If the separation between the QPCs is bigger than the spin-rotation length, we can also compute the off-diagonal elements of $Q$

$$\begin{aligned} Q_{ij} &= \int \frac{dk}{2\pi} e^{-ik(x_i - x_j)} B(k) G(k) B^\dagger(k) \\ &= \frac{i}{2v} B(E/v)(1 - \sigma^3 \mathrm{sign}(x_i - x_j)) e^{-i\sigma^3(x_i - x_j)E/v} B^\dagger(E/v)\,. \end{aligned} \tag{3.22}$$

## 3.3 Mapping the spin rotation of the edge states

As a first step, we are going to consider the effect of a single point contact at the position $x_1$ with tunnel amplitude $\gamma_1$ between the two helical edges, see Fig. 3.1. Our first goal is to determine the total current flowing along the $x$-direction if the system is coupled to two reservoirs held at chemical potentials $\mu_- = \mu$ and $\mu_+ = \mu + V$ on the right and left sides, respectively. These reservoirs thus define the chemical potential of the right-movers $(\mu + V)$ and left-movers $(\mu)$.

Using Eqs. (3.3,3.19), we find the scattering matrix

$$S(E) = \sqrt{1 - T_1} - i\sqrt{T_1} \left[ \sin\theta(E)\, i\tau^1 + \cos\theta(E)\, \sigma^2\tau^2 \right] , \tag{3.23}$$

where we defined the spin-rotation difference

$$\theta(E) = \theta_U(E/v) - \theta_L(E/v)\,, \tag{3.24}$$

and the transmission probability $T_1$ across the QPC

$$T_1 = \left( \frac{2(\gamma_1/2v)}{1 + (\gamma_1/2v)^2} \right)^2 . \tag{3.25}$$

For the current, we find $I(V) = \int_0^V d\omega G(\mu + \omega)$, where $G(\mu)$ is the two-terminal differential conductance for a system held at chemical potential $\mu$,

$$G(\mu) = \frac{2e^2}{h} \left[ 1 - T_1 \cos^2 \theta(\mu) \right] . \tag{3.26}$$

According to Eq. (3.26), the angle difference $\theta(\mu)$ has a strong impact on the conductance, because it determines the amount of right-movers on the upper edge that become left-movers or right-movers in the lower edge after tunneling, see Fig. 3.1. In the limit of strong tunneling ($T_1 \to 1$), the conductance from left to right can change from zero at $\theta(\mu) = 0$ to $2e^2/h$ at $\theta(\mu) = \pi/2$.

### 3.3.1 Fabry-Pérot interferometer

Next, we extend the system by adding a second point contact [Dolcini11, Virtanen11, Romeo12] at position $x_2$ with the tunnel amplitude $\gamma_2$. The distance between the two point contacts is $\Delta x_2 = x_2 - x_1$. From here on, we assume that the rotation angles $\theta_\eta(k)$ change very slowly with $k$, only on a large momentum scale $k_0 \gg k_F$. Furthermore we assume that the distance between tunnel contacts is large compared to the Fermi wavelength, i.e., $\Delta x_2 \gg 1/k_F$.

The scattering matrix can be computed with our general formula (3.19). The resulting differential conductance reads

$$G(\mu) = 2G_0 \frac{\left[ 1 - T_1 \cos^2 \theta(\mu) \right] \left[ 1 - T_2 \cos^2 \theta(\mu) \right]}{\left| 1 + \sqrt{T_1 T_2} \cos^2 \theta(\mu)\, e^{2i\Delta x_2 \mu / v_F} \right|^2}. \tag{3.27}$$

We find interference patterns between the different paths that depend on the phase $\phi_2 = \Delta x_2 \mu / v_F$ acquired by an electron when passing through the loop formed by the two tunnel junctions. Multiple traversals of this loop yield a geometric series which leads to the denominator of Eq. (3.27). The conductance as a function of the phase $\phi_2$ and the spin rotation angle $\theta(\mu)$ is plotted for different tunnel probability combinations in Fig. 3.2. For equal tunnel strengths $T_1 = T_2$, we always find the maximal conductance of $2e^2/h$ at the resonance condition $\phi = \pi$, even for very weak tunneling. This can be interpreted as Fabry-Pérot resonances which remain visible in the current as long as $V \ll v_F/\Delta x_2$. In setups where the distance between the two tunnel contacts is tunable, varying $\Delta x_2$ makes it possible to measure $\theta(\mu)$ as a function of $\mu$.

## 3.4 Localization in a narrow strip with disorder

**Modeling disorder with point contacts**

Finally we shall examine a large number $N$ of point contacts between the two edges at random positions $x_j$ and with random tunnel amplitudes $\gamma_j$ as depicted in Fig. 3.3. At

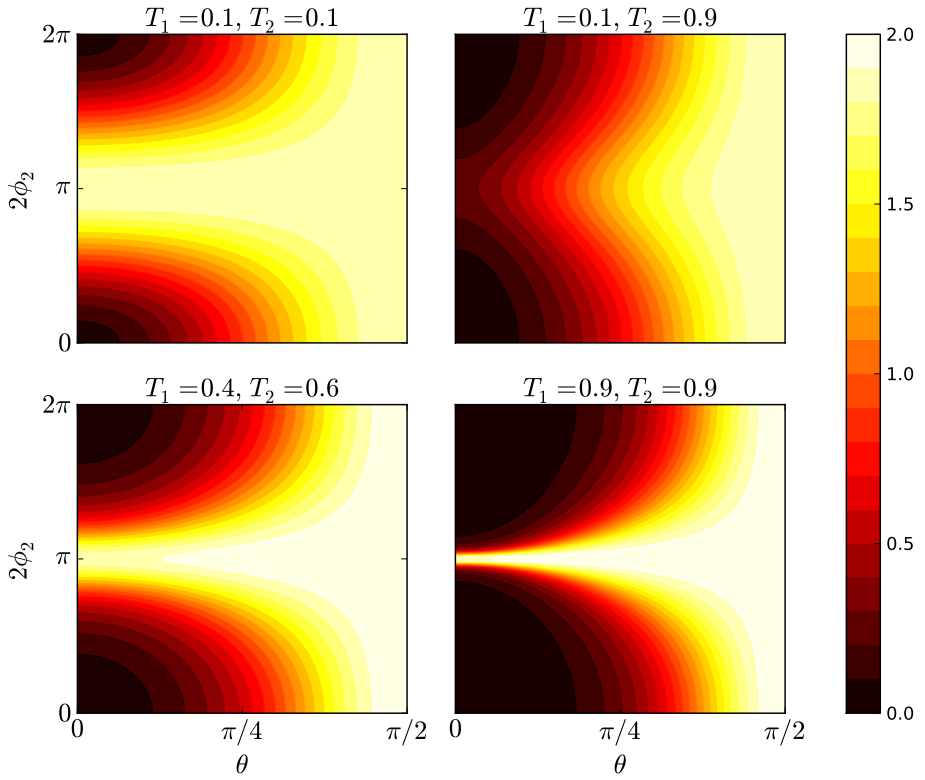


Figure 3.2: Conductance (in units of $e^2/h$) of a 2D topological insulator with two tunnel junctions as a function of the angle $\theta(\mu)$ and distance between tunnel junctions $\Delta x_2$, where $\phi_2 = \Delta x_2 \mu / v_F$. For $\theta = 0$, the setup shows Fabry-Pérot resonances: even if the transparency of the two QPCs is small but equal (upper left) all the electrons are transmitted across the interferometer at $\phi_2 = \pi/2$. For $\theta = \pi/2$, there is no backscattering at the QPCs and all the electrons are transmitted to the right contact.

the end we shall perform a disorder average over the $x_j$ and $\gamma_j$. This model captures the physics of narrow samples where the helical edges are connected by charge puddles [Skinner12, Väyrynen13, König13] that originate from doping. We effectively describe this situation by a set of point contacts

$$H_{\gamma,N} = \sum_{j=1}^{N} \gamma_j \psi^\dagger(x_j) \tau_1 \psi(x_j) \,, \tag{3.28}$$

which we add to $H_{kin}$. We assume that the positions $x_j$ are uniformly distributed in a region of length $L$, and that the density $n = N/L$ of point contacts is small, i.e., $k_0 \gg k_F \gg n$.

### Transfer matrix

For the disorder average over many point contacts it is most convenient to use transfer matrices to calculate the current. The transfer matrix $\mathcal{T}_j$ $(j = 1, \ldots N)$ relates the states

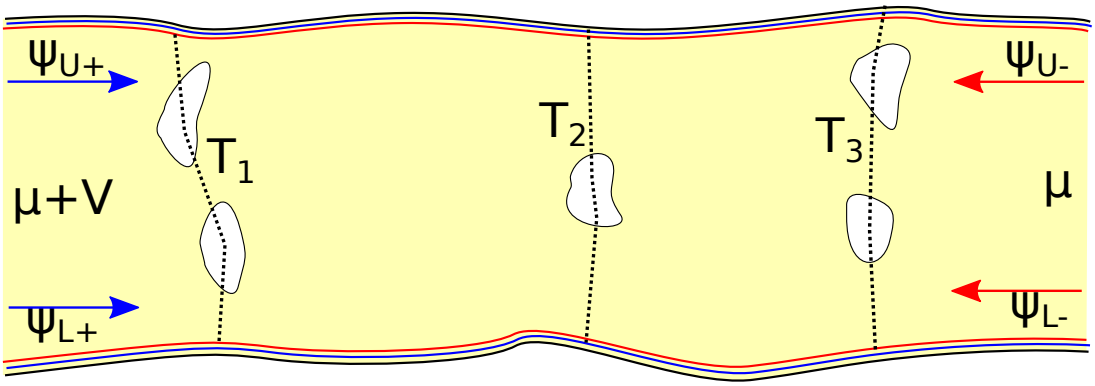


Figure 3.3: Charge puddles between two edges in a narrow 2D topological insulator can form tunnel paths at random positions $x_j$ and with random tunnel amplitudes $\gamma_j$. Tunneling leads to localization, with a localization length which depends strongly on the spin rotation angle $\theta(\mu)$.

on the left side of the $j$th point contact to those on its right side,

$$\begin{aligned}\mathcal{T}_j(\mu) &= \frac{1}{1-T_j\cos^2\theta}\begin{pmatrix} A & B \\ -B^* & A^*\end{pmatrix} \\ A &= \begin{pmatrix}\sqrt{1-T_j} & -i\sqrt{T_j}\sin\theta \\ -i\sqrt{T_j}\sin\theta & \sqrt{1-T_j}\end{pmatrix} \\ B &= \cos\theta\begin{pmatrix}-T_j\sin\theta & i\sqrt{(1-T_j)T_j} \\ -i\sqrt{(1-T_j)T_j} & T_j\sin\theta\end{pmatrix},\end{aligned} \tag{3.29}$$

in the basis $(\phi_{U+}, \phi_{L+}, \phi_{U-}, \phi_{L-})$. The total transfer matrix $\tilde{\mathcal{T}}_N$ for transport through $N$ point contacts can be determined from the following recursive relation [Delplace12]

$$\tilde{\mathcal{T}}_1 = \mathcal{T}_1, \quad \tilde{\mathcal{T}}_j = \tilde{\mathcal{T}}_{j-1}P_j\mathcal{T}_j, \tag{3.30}$$

where $P_j = \mathrm{diag}\left(e^{i\phi_j}, e^{i\phi_j}, e^{-i\phi_j}, e^{-i\phi_j}\right)$ is a diagonal transfer matrix that describes free propagation between the contacts at positions $x_{j-1}$ and $x_j$, and results in dynamical phases $\phi_j = \Delta x_j \mu/v_F$ for right-movers and $-\phi_j$ for left-movers, where $\Delta x_j = x_j - x_{j-1}$.

**Localization**

The total transfer matrix has the general structure

$$\begin{aligned}\tilde{\mathcal{T}}_j &= \begin{pmatrix}\lambda_j & \rho_j \\ -\rho_j^* & \lambda_j^*\end{pmatrix} \\ \lambda_j &= \begin{pmatrix}a_j & ia_jb_j \\ ia_jb_j & a_j\end{pmatrix}, \quad \rho_j = \begin{pmatrix}c_j & ic_j/b_j \\ -ic_j/b_j & -c_j\end{pmatrix}\end{aligned} \tag{3.31}$$

with two complex parameters $a_j, c_j$ and a real parameter $b_j$. Products of these transfer matrices always reproduce this structure. The lower right component of the transfer matrix is the inverse of the transmission matrix $t_j = (\lambda_j^*)^{-1}$ which is connected to the dimensionless

conductance through $j$ contacts as $\tilde{G}_j(\mu) = \mathrm{Tr}(t_j^\dagger t_j)$ [Bruus04]. Equation (3.30) leads to a recursive relation expressing the conductance through $j$ contacts in terms of the product of the conductance through $j-1$ contacts, the conductance of the $j$th contact, as well as a phase dependent term

$$\tilde{G}_j = \tilde{G}_{j-1}\frac{G_j}{2G_0}\left|1 + \frac{c_{j-1}}{a_{j-1}b_{j-1}}\sqrt{T_j}\cos\theta e^{-2i\phi_j}\right|^{-2} \tag{3.32}$$

where $G_j = 2G_0 - 2G_0T_j\cos^2\theta$ and $\tilde{G}_0 = 2$. We take the logarithm of the whole equation and solve it recursively. Averaging both sides over the phases $\phi_j$ yields for the total conductance of all $N$ contacts,

$$\langle\log(\tilde{G}_N/2)\rangle_\phi = \log\left(\frac{G_N}{2G_0}\right) + \cdots + \log\left(\frac{G_1}{2G_0}\right). \tag{3.33}$$

Furthermore, taking the average over the tunnel probabilities $T_j$ renders all the logarithms on the right side equal. Comparing the resulting equation

$$\langle\log(\tilde{G}_N/2)\rangle = N\left\langle\log\left[1 - T\cos^2\theta(\mu)\right]\right\rangle \tag{3.34}$$

with $\langle\log(\tilde{G}_N/2)\rangle = -L/\ell$ allows us to define the localization length as [Delplace12, Anderson80, Pendry94]

$$\begin{aligned}\ell^{-1} &= -\lim_{N\to\infty}\frac{n}{N}\left\langle\log(\tilde{G}_N/2)\right\rangle \\ &= -n\left\langle\log\left[1 - T\cos^2\theta(\mu)\right]\right\rangle.\end{aligned} \tag{3.35}$$

If the tunnel probabilities are small ($T_j \approx 0$) we can approximate the logarithm to linear order and obtain

$$\ell^{-1} = n\cos^2\theta(\mu)\langle T\rangle. \tag{3.36}$$

This means a change of $\theta(\mu)$ can change the localization length in the interval $1/(n\langle T\rangle) < \ell < \infty$. In particular, an infinite localization length can be reached even in the presence of tunneling for $\theta(\mu) = \pi/2$. In the opposite limit of large tunneling ($T_j \approx 1$) Eq. (3.35) becomes

$$\ell^{-1} = -n\log\left[\sin^2\theta(\mu)\right] \tag{3.37}$$

and the localization length can reach all values between zero and infinity for $\theta(\mu) \in [0, \pi/2]$.

In this derivation, we assumed for simplicity that $B_\eta(k)$ has the form shown in Eq. (3.3), which is true if tunneling conserves spin. We would like to point out, however, that the localization length depends strongly on the spin texture even if spin is not conserved during tunneling. In that case, $\ell$ is determined by the combination $B_U^\dagger(\mu/v_F)B_L(\mu/v_F)$ of spin rotation matrices.

## 3.5 Conclusion

To summarize, we have investigated narrow two-dimensional topological insulators where the helical liquids on the two opposite edges have different spin textures. In this case, the spin axes of two particles on the upper and lower edges at the Fermi energy $\mu$ are tilted by

an angle $\theta(\mu)$. This angle can be tuned in experiments, e.g., by applying a perpendicular electric field gradient. We have considered a system where the edge states are coupled locally by one or several tunnel contacts. For two tunnel contacts, interference effects in the two-terminal conductance make it possible to determine $\theta(\mu)$. Many random contacts lead to localization of the edge states with a strong dependence of the localization length on $\theta(\mu)$. These effects could be used in experiments to map the helical structure of the edge states.

# Chapter 4

# Interferometric and noise signatures of Majorana fermion edge states in transport experiments

This chapter is adapted from the publication:

> G. Strübi, W. Belzig, M.-S. Choi, and C. Bruder, *Interferometric and Noise Signatures of Majorana Fermion Edge States in Transport Experiments*, Phys. Rev. Lett **107**, 136403.

Because of their fascinating properties, and potential application to topological quantum computation [Kitaev01, Ivanov01, Nayak07, Alicea10, Stern13], Majorana fermions catalyzed an immense body of work. However the very nature of Majorana fermions make them elusive for unambiguous detection in experiments: they are chargeless and cannot be taken out of the sample for private inspection. Elaborate schemes leading to indirect but conclusive signatures of their presence are needed.

Recently, several groups [Mourik12, Deng12, Das12, Finck12] have reported the identification of Majorana bound states in nanowires through a measurement of a zero-bias peak in tunneling spectroscopy experiments. There is, however, no consensus regarding the attribution of this result to the presence of Majorana fermions and not on another origin [Liu12]. The situation is similar with the experimental report [Rokhinson12] of a $4\pi$-periodic Josephson effect [Fu09a], which cannot yet be unambiguously attributed to the presence of MBS in the josephson junction [Sau12].

There are also many proposals to detect Majorana fermions based on interferometric structures in the literature. They can be divided into two classes. The first class intends to probe the non-Abelian statistics of MBSs trapped in vortices of topological superconductors. In Ref. [Akhmerov09, Nilsson10] the authors study conductance signatures of vortex tunneling in a Fabry-Pérot interferometer. Another proposal [Grosfeld10] is based on a Mach-Zehnder interferometer constructed from a topological Josephson junction. In that case, Josephson vortices trapping a MBS propagate along the two arms of the in-

terferometer and give rise to a Josephson-vortex current $I_v$. The presence of absence of another MBS at the center of the interferometer, which can be tuned by a magnetic flux, leads to a striking switching between a vanishing $I_v$ and a nonzero $I_v$. The roots of this effect are traced back to the non-Abelian exchange statistics of MBSs.

The goal of the second class of interferometer-based proposals is to find a signature of Majorana edge states. Ref. [Liu11b] finds a signature of chiral Majorana modes in the conductance of a Mach-Zehnder interferometer built in a S-QSH-S sandwich. In [Park13] the absence of an Aharonov-Bohm effect for Majorana edge states is predicted. We also mention a nice formulation of the scattering matrix approach in terms of Majorana modes [Li12] that highlights their special properties and is readily applied to these interferometric structures.

In Sec. 4.2, we review in more details early proposals [Fu09b, Akhmerov09] that also belong to the second class. They propose to use 3D topological insulator heterostructures to build a Mach-Zehnder interferometer for Majorana edge states contacted by electronic leads and find conductance signatures. In Sec. 4.3, we extend this setup and propose to study noise correlations in a Hanbury Brown-Twiss type interferometer. We find three signatures of the Majorana nature of the channels. First, the average charge current in the outgoing leads vanishes. Furthermore, we predict an anomalously large shot noise in the output ports for a vanishing average current signal. Adding a quantum point contact to the setup, we find a surprising absence of partition noise which can be traced back to the Majorana nature of the carriers. In Sec. 4.4 we further study the full counting statistics of transport in these interferometers and find an interesting interpretation of charge transfer processes in term of two independent half-charge transfers.

## 4.1 3D Topological insulators in heterostructures

The surface states of topological insulators provide a firm basis to realize nontrivial topological states. The intuitive way to understand this comes from the description of these boundary states in terms of a single Dirac cone. As a consequence, if we open a gap in these boundary states, we expect that the topological contribution coming from the massive Dirac point is not compensated by an opposite contribution from another Dirac point.

We can envision two interesting types of gaps of magnetic and superconducting origin. A natural way to induce a superconducting gap is by the proximity of an ordinary s-wave superconductor. Likewise, a magnetic gap can be opened by the proximity of an insulating ferromagnet. In this section, we review the proposed heterostructures [Fu08, Fu09b, Akhmerov09] that realize these ideas.

### 4.1.1 Helical Majorana channels in S-TI-S structures

#### Proximity induced superconductivity for Dirac fermions

One way of realizing a topological superconductor goes through an heterostructure of an ordinary s-wave superconductor in proximity to the surface of a 3D topological insulator [Fu08]. Tunneling of Cooper pairs from the superconductor to the surface states of the topological insulator introduces a term $\Delta\psi_\uparrow^\dagger\psi_\downarrow^\dagger + h.c.$ in the Hamiltonian, where $\Delta = \Delta_0 e^{i\phi}$

is the proximity-induced pairing potential in the surface state of the topological insulator. In Nambu notation, $\Psi = (\psi_\uparrow, \psi_\downarrow, \psi_\downarrow^\dagger, -\psi_\uparrow^\dagger)^T$, the total Dirac-Bogoliubov-de Gennes Hamiltonian can be written $H = \int d^2k \frac{1}{2} \Psi^\dagger \mathcal{H} \Psi$, with

$$\mathcal{H} = \tau_z \left( v_F \boldsymbol{\sigma} \cdot \boldsymbol{k} - \mu \right) + \Delta_0 \left( \tau_x \cos\phi + \tau_y \sin\phi \right), \tag{4.1}$$

where the $\tau$ are Pauli matrices in particle-hole space. For a spatially homogeneous $\Delta$, the system acquires a gap and the spectrum reads

$$E(\boldsymbol{k}) = \sqrt{\left( \pm v_F \left| \boldsymbol{k} \right| - \mu \right)^2 + \Delta_0^2}\,. \tag{4.2}$$

What makes the system very interesting is the connection between the proximity induced $s$-wave pairing for Dirac electrons Eq. (4.1) and $p$-wave superconductivity. Introducing the operators $c_{\boldsymbol{k}\pm}$

$$\psi_{\boldsymbol{k}\uparrow} = \frac{c_{\boldsymbol{k}+} + c_{-\boldsymbol{k}-}^\dagger}{2} e^{-i\theta_{\boldsymbol{k}}} \tag{4.3}$$

$$\psi_{\boldsymbol{k}\downarrow} = \frac{c_{\boldsymbol{k}+} - c_{-\boldsymbol{k}-}^\dagger}{2} e^{i\theta_{\boldsymbol{k}}} \tag{4.4}$$

$$\boldsymbol{k} = k \begin{pmatrix} \cos\theta_{\boldsymbol{k}} \\ \sin\theta_{\boldsymbol{k}} \end{pmatrix}, \tag{4.5}$$

the Hamiltonian becomes

$$H = \sum_{\boldsymbol{k}, s=\pm} (v_F k - s\mu) c_{\boldsymbol{k}s}^\dagger c_{\boldsymbol{k}s} + \Delta e^{-is\theta_{\boldsymbol{k}}} c_{\boldsymbol{k}s}^\dagger c_{-\boldsymbol{k}s}^\dagger + \Delta^* e^{is\theta_{\boldsymbol{k}}} c_{-\boldsymbol{k}s} c_{\boldsymbol{k}s}\,. \tag{4.6}$$

This Hamiltonian belongs to the Altland-Zirnbauer symmetry class DIII, characterized by a $\mathbb{Z}_2$ invariant, see Tab. 2.1. It is in the topologically nontrivial phase of two copies of spinless $p_x + ip_y$ superconductors with opposite chiralities related by TRS. As such, we expect to find a pair of helical Majorana edge states at the boundary of this state.

### Majorana channels at domain walls

Let us now consider domain walls in the induced pairing potential $\Delta(x, y)$. We consider a domain wall parallel to the $x$ axis, see Fig. 4.1. The pairing potential only depends on $y$ and we retain full translation invariance in the $x$ direction. The Hamiltonian reads

$$\mathcal{H}(y) = \tau_z \left( -iv_F \sigma_y \partial_y + v_F \sigma_x k_x - \mu \right) + \Delta_0(y) \left( \tau_x \cos\phi(y) + \tau_y \sin\phi(y) \right)\,. \tag{4.7}$$

We treat the term containing the longitudinal momentum $k_x$ as a perturbation, and we denote the remaining part by $\mathcal{H}_0$. To solve the Schrödinger equation $\mathcal{H}_0(y)\chi(y) = E\chi(y)$, we isolate $\partial_y \chi$:

$$\partial_y \chi(y) = \frac{1}{v_F} [i\mu\sigma_y + \Delta_0(y)\sigma_y(\cos\phi(y)\tau_y - \sin\phi(y)\tau_x) + iE\sigma_y\tau_z]\chi(y)\,, \tag{4.8}$$

which we write

$$\partial_y \chi(y) = V(y)\chi(y)\,. \tag{4.9}$$

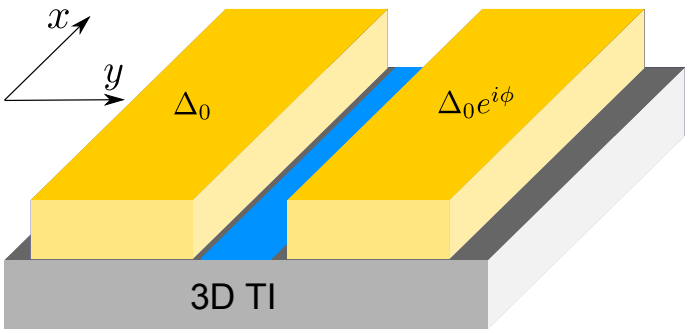


Figure 4.1: Two $s$-wave superconductors (yellow) in contact with the surface of a 3D topological insulator. Superconductivity is induced in the surface states of the 3D TI. Bound states appear at the interface in the surface of the TI (blue region) when the two superconductors have a nonzero phase difference $\phi$. For $\phi = \pi$ the interface supports gapless helical Majorana modes.

We are looking for solutions of this equation $\chi(y)$ that are localized around $y = 0$. If $V(y)$ has the following simple spatial structure

$$V(y) = \begin{cases} V_< & \text{for } y < 0\,, \\ V_> & \text{for } y > 0\,, \end{cases} \tag{4.10}$$

and providing that there is exactly one eigenvalue $\lambda_>$ of $V_>$ and one eigenvalue $\lambda_<$ of $V_<$ leading to a bound state (i.e. the real part of $\lambda_{>,<}$ is negative, resp. positive) then we know the discontinuity of $\partial_y \chi(y)$ at $y = 0$. This allows us to write

$$(\lambda_> - \lambda_<)\chi(0) = (V_> - V_<)\chi(0)\,, \tag{4.11}$$

which is in general a simpler problem. In particular $\mu$ and $E$ will drop out of the right-hand side of equation (4.11). We can then find the eigenvalues of $(V_> - V_<)$ and see if one of them match $(\lambda_> - \lambda_<)$ (this quantizes the energy $E$). Finally, the corresponding eigenvector $\chi(0)$ fixes the full bound state $\chi(y) = e^{\lambda_> y}\chi(0)$ for $y > 0$, $\chi(y) = e^{\lambda_< y}\chi(0)$ for $y < 0$.

We now consider a sharp domain wall of the superconducting phase

$$\phi(y) = \begin{cases} 0 & y < 0 \\ \phi & y > 0, \end{cases} \tag{4.12}$$

and $\Delta_0(y) \equiv \Delta_0$ constant. Equation (4.8) reads

$$\partial_y \chi(y) = \frac{1}{v_F}[i\mu + \Delta_0(\cos\phi(y)\tau_y - \sin\phi(y)\tau_x) + iE\tau_z]\sigma_y\chi(y). \tag{4.13}$$

We treat the cases $\sigma_y\chi_\pm(y) = \pm\chi_\pm(y)$ separately. For $\chi_+$ we have $\lambda_> - \lambda_< = -2\sqrt{\Delta_0^2 - E^2}/v_F$ and $V_> - V_< = \Delta_0/v_F((\cos\phi - 1)\tau_y - \sin\phi\tau_x)$ with eigenvalues $\pm 2/v_F \sin\phi/2$. Solving Eq. (4.11) we find the Andreev bound states energies

$$E = \pm\Delta_0 \cos\phi/2\,. \tag{4.14}$$

Note that our derivation thus far was only for $k_x = 0$. The free bonus that comes with this is that Eq. (4.13) also describes a 1D domain wall between two 1D topological superconductors. This situation is realized in superconductor-QSH insulator-superconductor heterostructures. In this context, it was shown [Fu09a] that he $\phi/2$ dependence of the Andreev bound states (4.14) is responsible for a $4\pi$ periodicity of the Josephson effect.

For the special case $\phi = \pi$, we find $E = 0$ and it is possible to express the bound states for an arbitrary spatial modulation of the pairing amplitude $\Delta_0(y)$, because of the vanishing commutator $[V(y), V(y')] = 0$ in the left and right regions. The solutions are

$$\chi_\pm(y) \propto e^{-|\int_0^y dy' \ \Delta_0(y')/v_F|} e^{\pm i\mu y/v_F} \begin{pmatrix} 1 \\ \pm i \\ \pm i \\ -1 \end{pmatrix}. \tag{4.15}$$

We can then include $k_x \neq 0$ by evaluating the matrix elements $\langle \chi_\pm | \mathcal{H} | \chi_\pm \rangle$. We get the Hamiltonian projected on the bound states

$$\widetilde{\mathcal{H}} = v_m k_x \widetilde{\sigma}_x \tag{4.16}$$

where $v_m = v_F \langle \chi_+ | \sigma_x \tau_z | \chi_- \rangle$ and $\widetilde{\sigma}$ acts in the $\chi_\pm$ basis. The eigenmodes $\gamma_1 = (\chi_+ + \chi_-)/\sqrt{2}$, $\gamma_2 = i(\chi_+ - \chi_-)/\sqrt{2}$ saitisfy are self adjoint $\gamma_1^\dagger = \gamma_1$, $\gamma_2^\dagger = \gamma_2$. They are helical Majorana fermions that propagate with velocity $v_m$ along the domain wall. If the characteristic width $W$ of the domain wall is large enough, $W > v_F/\Delta_0$, higher energy Andreev bound states appear in the junction, but the low energy sector of interest is still described by a single helical Majorana fermion.

### 4.1.2 Chiral electron channels in FM-TI-FM structures

We now investigate the effect of a magnetic gap induced by the proximity of an insulating ferromagnet to the surface states of the 3D topological insulator [Fu09b]. The Hamiltonian we consider is

$$\mathcal{H} = v_F \boldsymbol{k} \cdot \boldsymbol{\sigma} + \boldsymbol{M} \cdot \boldsymbol{\sigma} - \mu \tag{4.17}$$

where $\boldsymbol{M}$ is the exchange field induced by the proximity of the ferromagnet. The out-of-plane component $M_z$ opens a Zeeman gap of magnitude $M_z$ at the Dirac point.

#### Chiral Dirac electrons at domain walls

We model a simple magnetic domain wall along $x$, see Fig. 4.2, with $M_z = M\mathrm{sgn}(y)$ and $M_x = M_y = 0$. We treat again the term containing $k_x$ as a perturbation. The matrices that describe the propagation along the $y$-axis in the right and left regions, see Eq. (4.9), are given by

$$V_{>,<} = \frac{1}{v_F}[\pm M\sigma_x + i(E + \mu)\sigma_y]\,. \tag{4.18}$$

Solving Eq.(4.11) for this case yields $E = -\mu$ and the corresponding bound state

$$\chi(y) = \frac{1}{\sqrt{2}} \begin{pmatrix} 1 \\ -\mathrm{sgn}(M) \end{pmatrix} \frac{v_F}{2|M|} e^{-|\frac{M}{v_F} y|} \tag{4.19}$$

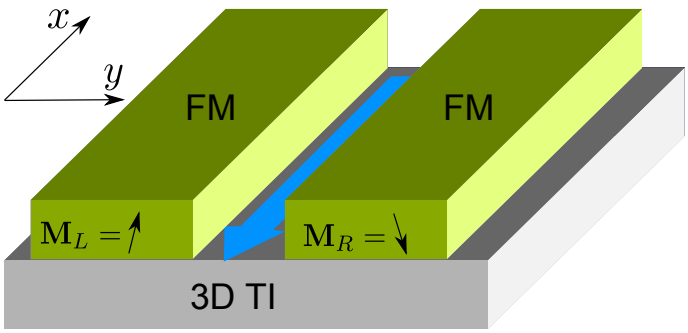


Figure 4.2: Insulating ferromagnets (green) induce an exchange field in the surface states of the 3D topological insulator. If the magnetizations $\boldsymbol{M}_L$ and $\boldsymbol{M}_R$ have opposite $z$ components, the magnetic domain wall along $x$ supports a chiral channel of Dirac electrons denoted by the blue arrow in the figure.

with the proper normalization. The bound state is localized over a scale $L_M = \frac{v_F}{|M|}$. Projecting the original Hamiltonian (4.17) with $k_x \neq 0$ we get the dispersion relation of the bound state

$$E(k_x) = -\mathrm{sgn}(M) v_F k_x - \mu\,. \tag{4.20}$$

The domain wall is thus a chiral channel for electrons. Again, a finite "well-width' W ($M_z(y) = 0, |y| < W/2$) will allow for further branch of bound states if $W > L_M$, with an energy spacing of $ML_M/W$.

**Arbitrary directions of $\boldsymbol{M}$** We can now consider the more general case

$$\boldsymbol{M}(y) = \begin{cases} \boldsymbol{M}_L & \text{for } y < 0 \\ \boldsymbol{M}_R & \text{for } y > 0, \end{cases} \tag{4.21}$$

Where the magnitudes are the same $M_{L,R} = M$, but the directions are arbitrary. The $y$-component of $\boldsymbol{M}$ only induces phase oscillations of the wavefunction along $y$ and we neglect it. Parameterizing the two magnetizations with polar angles $\theta_{L,R}$

$$\boldsymbol{M}_{L,R} = M \begin{pmatrix} \cos\theta_{L,R} \\ 0 \\ \sin\theta_{L,R} \end{pmatrix} \tag{4.22}$$

and defining

$$\theta = \frac{\theta_R + \theta_L}{2} \tag{4.23}$$

$$\alpha = \frac{\theta_R - \theta_L}{2}, \tag{4.24}$$

we get the dispersion relation

$$E(k_x) = M\cos\alpha + M\sin\theta v_F p_x - \mu\,. \tag{4.25}$$

One possible application is to tune the velocity of the bound states, $v_F \sin\theta$, by modifying the orientation of the magnetizations.

### 4.1.3 Chiral Majorana channels in S-TI-FM structure

We now consider a combination of the first two structures. On the right, $y > 0$, we induce a superconducting gap $\Delta_0$ and on the left, $y < 0$, a magnetization $M_z > 0, M_x = M_y = 0$. Solving the resulting Bogoliubov-de Gennes equation with $k_x = 0$ we find $E = 0$ (due to particle-hole symmetry) and the corresponding spinor

$$\chi(y=0) \propto \begin{pmatrix} \sqrt{M+\mu} \\ \sqrt{M-\mu} \\ -\sqrt{M-\mu} \\ \sqrt{M+\mu} \end{pmatrix} . \tag{4.26}$$

$\chi(y)$ is then found using equation(4.8), and is exponentially decreasing over scales $L_S = v_F/\Delta_0$ and $L_M = v_F/\sqrt{M^2-\mu^2}$ in the superconducting and magnetic regions respectively. It is therefore necessary to tune the Fermi energy to lie within the magnetic gap.

The linearized dispersion relation of this mode is given by

$$E(k_x) = v_F\sqrt{M^2-\mu^2}\, k_x \, . \tag{4.27}$$

The spinor is particle-hole symmetric and therefore describes a Majorana fermion. The domain wall support a chiral Majorana mode.

There is a related proposal [Tiwari12] to obtain a one-dimensional channel of chiral Majorana fermions. The idea is to replace the magnetic gap due to the ferromagnetic insulator by a strong perpendicular magnetic field. Relativistic Landau levels are formed in the surface states of the topological insulator in the normal region. At the boundary with the superconducting region, the authors show the formation of chiral Andreev edge channels arising from Landau levels. The edge channel coming from from the $N = 0$ Landau level can be identified as a Majorana edge channel.

## 4.2 Mach-Zehnder interferometer

In this section we review the early proposals [Akhmerov09, Fu09b] that use a Mach-Zehnder interferometer built out of the kind of heterostructures we have described. They find a signature of chiral Majorana fermions in the conductance of the structure.

### 4.2.1 Converting Dirac electrons to Majorana fermions

Combining the different types of domain walls, we are able to construct "exotic" circuits supporting electrons and Majorana fermions. A particularly intersecting building-block is the "Dirac-to-Majorana converter" [Akhmerov09, Fu09b] shown in Fig. 4.3. In this structure an incoming chiral Dirac electron is converted into a Majorana fermion split into two channels. Because of chirality no backscattering can occur at the junction; the conversion process works with full efficiency.

#### Symmetry constraints on the scattering matrix

We use the scattering matrix formalism [Büttiker92] to describe transport and noise properties of all the interferometers in this section. The central quantity we need is the scattering matrix of the Dirac-to-Majorana converter that relates the outgoing Majorana modes

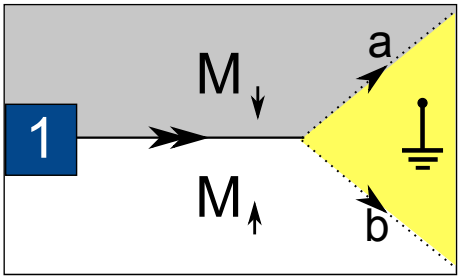


Figure 4.3: Splitting of a chiral electronic channel (1) to a pair of chiral Majorana fermions channels (a),(b). $M_{\uparrow(\downarrow)}$ represents regions with magnetization pointing up (down) and the yellow part is superconducting.

to the incoming Dirac modes. Because we do not want to consider a detailed and specific model for the junction, we shall limit ourselves to a study of the constraints imposed by symmetry and unitarity. The scattering matrix is defined, at a given energy $E$, by

$$\begin{pmatrix} \gamma_a \\ \gamma_b \end{pmatrix} = S_{D\to M}(E) \begin{pmatrix} \psi_{1,e} \\ \psi_{1,h} \end{pmatrix} . \tag{4.28}$$

Particle-hole symmetry relates the scattering matrix at energy $E$ to the scattering matrix at energy $-E$ in the way

$$S_{D\to M}(E) = S^*_{D\to M}(-E) \begin{pmatrix} 0 & 1 \\ 1 & 0 \end{pmatrix} . \tag{4.29}$$

Together with unitary, particle-hole symmetry determines the entire form of the scattering matrix at zero energy

$$S_{D\to M}(E=0) = \frac{1}{\sqrt{2}} \begin{pmatrix} 1 & 1 \\ \pm i & \mp i \end{pmatrix} \begin{pmatrix} e^{i\alpha} & 0 \\ 0 & e^{-i\alpha} \end{pmatrix} , \tag{4.30}$$

up to an unimportant phase $\alpha$ (gauge choice for the Dirac modes) and a sign convention for the Majorana modes.

At nonzero energies small deviations can occur, but the corrections are expected to be small for $E \ll \Delta$. Moreover if there is an additional mirror symmetry one can show that the form given by Eq. (4.30) is exact at all energies [Akhmerov09]. For these reasons, we shall work with the energy independent scattering matrix

$$S_{D\to M} = \frac{1}{\sqrt{2}} \begin{pmatrix} 1 & 1 \\ i & -i \end{pmatrix} . \tag{4.31}$$

We see from the form of the scattering matrix that the charge of the incoming particle is encoded nonlocally into the phase difference of the Majorana mode in the two arms. Namely, $\phi_a - \phi_b = \pm\pi/2$ for an incoming electron, or hole respectively.

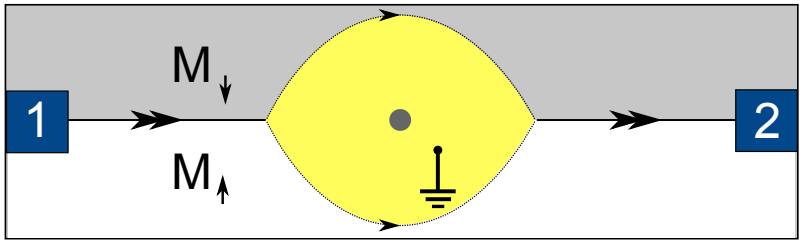


Figure 4.4: Mach-Zehnder interferometer. An incoming charged Dirac fermion is converted into a Majorana fermion which propagates along two possible paths around the superconductor. Depending on the parity of the number of vortices threading the superconductor, the Majorana fermion is converted back to either an electron or a hole. The superconductor is grounded to compensate for the net charge transfer in the interferometer.

#### Majorana-to-Dirac converter

The scattering matrix for the inverse process, fusing two Majorana arms into one Dirac arm, can be simply obtained by taking the time reversed version of Eq. (4.31)

$$S_{M\to D} = (S_{D\to M})^T = \frac{1}{\sqrt{2}} \begin{pmatrix} 1 & i \\ 1 & -i \end{pmatrix} . \tag{4.32}$$

Again, the charge of the outgoing Dirac electron is encoded in the relative phase of the incoming Majorana fermions.

As a side remark, we note that one might be worried by the apparent violation of spin and charge conservation. Indeed consider an incoming electron on the left lead (with a charge -e and a definite spin). After going through the junction (it cannot be reflected) it is converted into a Majorana fermion which is neutral and does not carry the same spin as the electron. Hence both charge and spin conservation appear to be broken. This formal artifact is in fact expected, for our mean-field description of the superconductor and the ferromagnet does not conserve either. In reality those conservation laws are satisfied by, possibly copropagating, spin excitations in the ferromagnet and Cooper pairs in the superconductor. Grounding the superconductor ensures that it will not accumulate charges over the course of conversion processes.

### 4.2.2 $\mathbb{Z}_2$ interferometry

Following [Fu09b, Akhmerov09] we introduce a Mach-Zehnder interferometer for Majorana fermions. It combines two converters of the last section: an incoming arm supporting Dirac-like excitations is split into two Majorana arms that interfere and fuse back together into an outgoing Dirac arm. The two Majorana arms encircle a superconducting region. A number $n_v$ of vortices is threading the superconductor. A sketch of the setup is shown in Fig. 4.4.

Owing to the chirality of the propagating modes, the total scattering matrix

$$\begin{pmatrix} \psi_{2,e} \\ \psi_{2,h} \end{pmatrix} = S_{\text{tot}} \begin{pmatrix} \psi_{1,e} \\ \psi_{1,h} \end{pmatrix} \tag{4.33}$$

can be obtained by multiplying the scattering matrices for the two conversion processes and for the free propagation of Majorana fermions inbetween

$$S_{\text{tot}} = \frac{1}{2}\begin{pmatrix} 1 & i \\ 1 & -i \end{pmatrix}\begin{pmatrix} e^{i\phi_a} & 0 \\ 0 & e^{i\phi_b} \end{pmatrix}\begin{pmatrix} 1 & 1 \\ i & -i \end{pmatrix} \tag{4.34}$$

where $\phi_{a,b}$ are the phases accumulated by the Majorana fermions along $a$ and $b$. There are several contributions to the phase difference $\phi_a - \phi_b$. The first one is a dynamical phase due to the length difference $\delta L$ of the two arms, the second one is a Berry phase of $\pi$ due to the rotation of a spin 1/2 ($e^{i\sigma_z(2\pi)/2}$) and the third is coming from the magnetic flux. Notice that the latter does not come from the term involving directly the vector potential in the Hamiltonian since $\langle\chi|\,\sigma_x\,|\chi\rangle = 0$ for the bound-state $\chi$ given by equation (4.26), rather it is the modulation of the phase of the superconductor ($e^{i\tau_z n_v \pi}$) that is responsible for this. Collecting everything we obtain

$$\phi_a - \phi_b = E\delta L/v_M + \pi + n_v\pi. \tag{4.35}$$

The total scattering matrix takes the form

$$S_{\text{tot}} = \begin{pmatrix} i\cos(\phi/2) & -\sin(\phi/2) \\ -\sin(\phi/2) & i\cos(\phi/2) \end{pmatrix}, \tag{4.36}$$

where we defined $\phi = E\,\delta L/v_M + n_v\pi$.

For a symmetric interferometer, $\delta L = 0$, and an even number of vortices the interferometer acts trivially: electron(holes) are transmitted as electrons(holes) with unit probability. For an odd number of vortices, however, electrons are transmitted as holes and vice-versa. This interferometer is sometimes called $\mathbb{Z}_2$ interferometer due to its sensitivity to the *parity* of the number of vortices.

### Conductance

We now fix a voltage $V > 0$ between the terminals 1 and 2. Both the terminal 2 and the superconductor are grounded. The differential conductance $G_{12}(V)$ is readily obtained from the scattering matrix (4.36). At zero temperature we obtain

$$G_{12}(V) = \frac{e^2}{h}\cos\left(n_v\pi + \frac{eV\,\delta L}{v_M}\right). \tag{4.37}$$

We may instead consider the current that flows through the superconductor due to charge conversion processes in the interferometer. The differential conductance reads

$$G_{1s}(V) = \frac{2e^2}{h}\sin^2\left(\frac{n_v\pi}{2} + \frac{eV\,\delta L}{2v_M}\right), \tag{4.38}$$

where $s$ denotes the superconducting terminal. This equation was first derived in [Fu09b, Akhmerov09]. Notably, the linear response conductance $G_{1s}(0)$ is quantized to $2e^2/h$ for an odd number of enclosed vortices in the interferometer, while it vanishes if the number of vortices is even. This is the main transport signature of Majorana fermions in this Mach-Zehnder interferometer setup.

### 4.2.3 Current-current correlations

For completeness, we also derive the current-current correlations obtained in the structure. For the symmetric interferometer, $\delta L = 0$, we can simply express the current operator in lead 2 as $I_2 = (-1)^{n_v} I_1$. Thus the cross-correlation $S_{12} = \frac{h}{2}\langle\{\Delta I_1, \Delta I_2\}\rangle = (-1)^{n_v}\frac{h}{2}\langle\{\Delta I_1, \Delta I_1\}\rangle = (-1)^{n_v} S_{11}$ is equal to $\pm$ the autocorrelation of the current in lead 1 . In particular, cross-correlations can be switched between positive and negative values by tuning the magnetic field in the superconductor. Note that if we want to obtain the cross-correlations with the superconducting lead $s$ , we can use such relations as $S_{11}+S_{12}+S_{1s} = 0$ that come from the conservation of charge. The current autocorrelation in the incoming lead is simply the sum over fluctuations in the electron and hole channel

$$S_{11} = \frac{e^2}{h}\int_0^\infty dE\ \left(n_{1,e}(1-n_{1,e}) + n_{1,h}(1-n_{1,h})\right), \tag{4.39}$$

where $n_{1,e}$ is the occupation of electrons in lead 1, and $n_{1,h}$ is the occupation of holes in lead 1. At zero temperature all the correlations vanish; the transport is noiseless.

In the nonsymmetric case we find $\langle I_2\rangle = \cos\phi\langle I_1\rangle$ and the current autocorrelation has an additional term

$$S_{22} = S_{11} + \frac{e^2}{h}\int_0^\infty dE\ \sin^2\phi(n_{1,e} - n_{1,h})^2 \tag{4.40}$$

The extra noise is attributed to probabilistic partioning of incoming electrons in lead 1 into electrons or holes in lead 2.

## 4.3 Hanbury Brown-Twiss interferometer

The form of the conductance of the Mach-Zehnder interferometer shows the same periodicity as a normal (non-superconducting) interference experiment. Hence, there is a need for further signatures of Majorana physics beyond the Mach-Zehnder setup. The structure we have in mind is a Hanbury Brown-Twiss (HBT) type interferometer built on the surface of a topological insulator. This setup is inspired by recent proposals [Fu09b, Akhmerov09, Bose11, Chung11] and is related to the two-particle Aharonov-Bohm effect [Samuelsson04]. We calculate the current cross-correlations in the two outgoing leads of this interferometer and predict the possibility to switch between negative and positive current cross-correlations by tuning the magnetic flux threading the superconductor. Positive cross-correlations are remarkable since non-interacting fermions will always show a negative sign [Büttiker92]; see, however, [Martin96, Börlin02, Samuelsson02]. The cross-correlations are predicted to be temperature-independent in a reasonable range of temperature and at low voltages. As in [Chung11] we find that the cross-correlations vanish when only one source is active as the consequence of the transport through Majorana modes.

We then consider a setup that contains an additional quantum point contact (QPC), similarly as in [Fu09b]. Strikingly, the partition noise associated to the quantum point contact is predicted to vanish, which is an evidence of the neutrality, or equivalently, the Majorana nature, of the charge carriers.

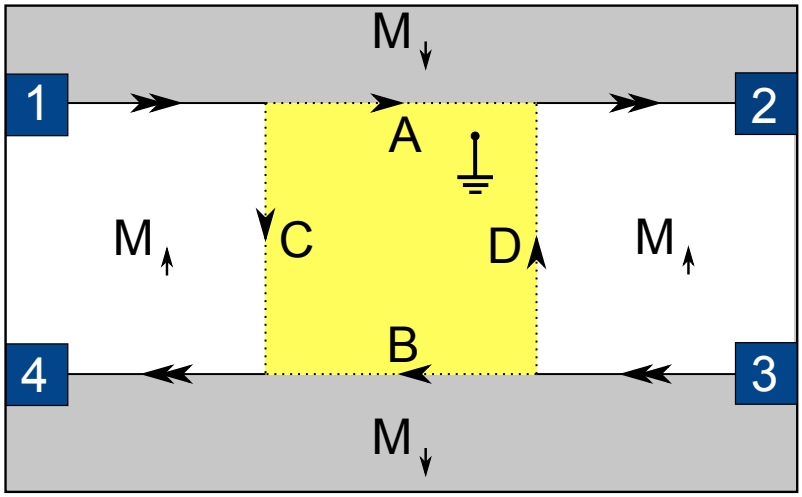


Figure 4.5: Hanbury Brown-Twiss type interferometer. A grounded superconductor surrounded by four magnetic domains is placed on the surface of a three-dimensional topological insulator. The terminals 1, 2, 3, and 4 are connected to the outside circuit and biased at potentials $V_1, \ldots, V_4$ respectively. The magnetizations are chosen such that Dirac electron states at leads 1, 2, 3, and 4 exist and propagate in the direction of the double arrows. Electrons and holes can enter the interferometer at leads 1 and 3, Majorana fermions propagate along the arms A,B,C, and D in the direction of the single arrows and electrons and holes leave through leads 2 and 4. A magnetic flux in the form of $n_v$ vortices threading the superconductor will control the phase difference between the arms of the interferometer.

**Setup**

We propose to realize a Hanbury Brown-Twiss type interferometer consisting of a grounded superconductor surrounded by four magnetic domains, as shown in Fig. 4.5. Incoming electrons (holes) are associated to the operators $\psi_{1,e(h)}, \psi_{3,e(h)}$, outgoing electrons (holes) to $\psi_{2,e(h)}, \psi_{4,e(h)}$ and intermediate Majorana fermions to $\gamma_{a,b,c,d}$. Combining the previous result for the scattering matrix of the Dirac-Majorana converter, see Eq. (4.31), the total scattering matrix is straightforward to compute. The result is

$$\begin{pmatrix} \psi_{2,e} \\ \psi_{2,h} \\ \psi_{4,e} \\ \psi_{4,h} \end{pmatrix} = \frac{1}{2} \begin{pmatrix} 1 & 1 & 1 & 1 \\ 1 & 1 & -1 & -1 \\ 1 & -1 & \eta & -\eta \\ 1 & -1 & -\eta & \eta \end{pmatrix} \begin{pmatrix} \psi_{1,e} \\ \psi_{1,h} \\ \psi_{3,e} \\ \psi_{3,h} \end{pmatrix} , \tag{4.41}$$

where $\eta = \pm(-1)^{n_v} e^{ik\delta L}$, $\delta L = L_a + L_d - L_b - L_c$ is the arm length asymmetry and $k = E/\hbar v_M$ is the wavenumber at energy $E$. This scattering matrix is exact at zero energy but remains valid for $E \ll (v_M/v_F)\Delta$, where $v_M$ is the Majorana fermion velocity and $v_F$ the Fermi velocity at the surface of the bare topological insulator. We also chose a gauge to concentrate the whole phase shift on the arm D of the interferometer.

For topological reasons, one-particle quantities are not sensitive to the enclosed flux in this structure: because of the chiral nature of the Majorana states, no one-particle state will enclose the flux. One incoming electron or hole is scattered with equal probability to a hole or an electron at lead 2 or 4. The outgoing currents thus vanish on average. This vanishing conductance is a first hallmark of Majorana fermions: in a standard setup with Andreev processes this could occur only accidentally, and small perturbations would give rise to a nonzero conductance. However a vanishing conductance could in principle be due to an interrupted circuit and has to be complemented by an additional measurement of, e.g., the current autocorrelation discussed below.

On the other hand, when both sources are active we expect to see a manifestation of an interesting two-particle Aharonov-Bohm effect [Samuelsson04, Neder07] for Majorana fermions. As an example consider two incoming electrons in leads 1 and 3

$$\begin{aligned} \psi_{1,e}\psi_{3,e} = &- (\psi_{2,e}\psi_{2,h} + \eta^* \psi_{4,e}\psi_{4,h})/2 \\ &+ (\eta^* - 1)(\psi_{2,e}\psi_{4,e} - \psi_{2,h}\psi_{4,h})/4 \\ &+ (\eta^* + 1)(\psi_{2,h}\psi_{4,e} - \psi_{2,e}\psi_{4,h})/4 \, . \end{aligned} \tag{4.42}$$

The current cross-correlations between leads 2 and 4 are thus expected to be sensitive to the parity of the number $n_v$ of enclosed vortices through the phase parameter $\eta$. In particular, as shown later, it is possible to switch between positive and negative cross-correlations by tuning the magnetic field threading the superconductor. As a side remark, note that post-selecting events with one fermion per lead for $\eta = \pm 1$ yields maximally entangled pairs in particle-hole space, and we can equivalently speak of antibunching [Büttiker92].

**Vanishing conductance**

The current operators are given by $I_j = \frac{e}{h}\int dE\ (b_j^\dagger(E)b_j(E) - a_j^\dagger(E)a_j(E))$. Expressing $I_2$ and $I_4$ in terms of the incoming modes gives

$$I_2 = -\frac{e}{2h}\int_0^\infty dE\ (a_1^\dagger(E) + b_1^\dagger(E))(a_3(E) + b_3(E)) + h.c. \tag{4.43}$$

$$I_4 = -\eta\frac{e}{2h}\int_0^\infty dE\ (a_1^\dagger(E) - b_1^\dagger(E))(a_3(E) - b_3(E)) + h.c. \tag{4.44}$$

Since the different reservoirs of incoming electrons are uncorrelated, the average current vanishes $\langle I_{2,4}\rangle = 0$ as was expected.

**Switching between positive and negative current-current cross-correlations**

The current-current cross-correlation

$$S_{24} = h\frac{1}{2}\langle\{I_2, I_4\}\rangle = -\frac{e^2}{h}\int_0^\infty dE\ \mathrm{Re}\,(\eta(E))(n_{1,e} - n_{1,h})(n_{3,e} - n_{3,h}) \tag{4.45}$$

is sensitive to the magnetic flux through the real part of $\eta$, $\mathrm{Re}\,(\eta) = (-1)^{n_v}\cos k\delta L$. At equilibrium $S_{24} = 0$; i.e., there is no thermal noise in this quantity (electrons and holes compensate each other). This temperature independence is expected to hold as long as $k_BT \ll (v_M/v_F)\Delta$. With a voltage bias configuration $V_1 = V_3 = V$, $V_2 = V_4 = 0$ (with respect to the potential of the superconductor), temperatures such that $k_BT \ll eV$ and an approximately symmetric interferometer, $\delta L \ll \hbar v_M/eV$,

$$S_{24} = (-1)^{n_v+1}\frac{e^2}{h}\int_0^\infty dE\ (n_e + n_h) = (-1)^{n_v+1}\frac{e^2}{h}e|V|\,. \tag{4.46}$$

Thus, the sign of the cross-correlation is given by the parity of the number of vortices. The possibility to achieve positive cross-correlations for fermions is attributed here to electron-hole conversions.

**Current-current autocorrelations**

The remaining cross-correlations are easily computed, we get $S_{13} = S_{23} = S_{14} = S_{24} = 0$ using the above expressions for $I_{3,4}$ and because the reservoirs $1, 2$ are uncorrelated. Also $S_{12} = 0$ for the same reason, and finally the autocorrelations of the incoming leads $S_{11(22)} = \frac{e^2}{h}\int dE\ (n_{1(2)e}(1 - n_{1(2)e}) + n_{1(2)h}(1 - n_{1(2)h}))$ present no special properties.

We now look at the current autocorrelations in the outgoing leads. While the outgoing current is zero on average, it is carried by electrons and (the same number of) holes. Current fluctuations are thus expected to be relevant. Indeed,

$$S_{22} = S_{44} = \frac{e^2}{h}\int_0^\infty dE\ (n_{1,e} + n_{1,h} + n_{3,e} + n_{3,h}) - (n_{1,e} + n_{1,h})(n_{3,e} + n_{3,h}) \tag{4.47}$$

At zero bias, this reduces to the usual Johnson-Nyquist noise $S_{22} = \frac{4e^2}{h}k_BT$, while for voltages $V_2 = V_4 = 0$, $V_1 = V_3 = V$ and $k_BT \ll eV$, we obtain a quantized shot noise

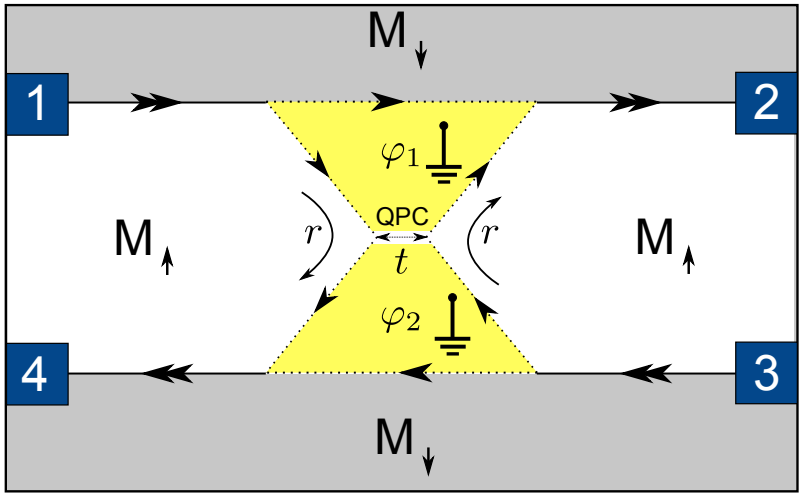


Figure 4.6: Modified Hanbury Brown-Twiss interferometer. Majorana excitations will propagate along the boundaries of the two triangular superconducting structures with phases $\varphi_1$, $\varphi_2$. An additional short gapped channel appears at the domain wall between the two superconducting regions, forming a quantum point contact characterized by reflection and transmission amplitudes $r$, $t$. The setup is similar to the one proposed in Ref. [Fu09b].

result $S_{22} = \frac{e^3}{h}|V|$, which is 4 times larger than the maximal expected shot noise due to a beam splitter of chiral electrons. This remarkable result can be explained by noting that in each scattering event both outgoing electrons and holes contribute to the charge fluctuations, while giving a zero average current as a consequence of the perfect electron-hole symmetry imposed by the Majorana conversion.

### 4.3.1 Point contact in the Hanbury Brown-Twiss interferometer

We would now like to discuss a second possibility to obtain a signature of Majorana fermions by adding a QPC to the previous setup; see Fig. 4.6. A novel feature will appear in the noise properties, which we want to study in the same spirit as in the previous section.

As explained in [Fu09b], the transmission and reflection amplitudes $t$, $r$ of the QPC can be strongly tuned by altering the geometry of the QPC itself, or by changing the phase difference $\varphi$ between the two superconducting parts. A narrow constriction would be dominated by direct tunneling and thus hardly sensitive to the phase difference. Therefore, the geometry we want to consider is closer to a line junction supporting a non-chiral Majorana channel on its own. By changing $\varphi = \varphi_1 - \varphi_2$ from $\varphi = 0$ to $\varphi = \pi$, the channel appearing at the interface of the two superconductors can be tuned from closed ($t \ll 1$) to fully open ($t \lesssim 1$) at zero energy. For intermediate values of the phase, the channel is gapped and the transmission amplitude strongly depends on energy.

We would first like to look at the limiting cases. For $t = 1$, $r = 0$, the upper and lower channels are not connected by the QPC. As a consequence, the setup effectively reduces to two independent copies of a Mach-Zehnder interferometer between terminals 1 and 2 (3 and 4) (see Fig. 4.6). The full current-current correlation matrix $S_{\mathrm{MZ+MZ}}$ for the

outgoing leads is easy to obtain in that case: the cross-correlations vanish since they are not connected in any way, and the auto-correlations are given in Table 4.1. For $t = 0$, the setup is equivalent to the HBT interferometer of the previous section, whose correlation matrix $S_{\mathrm{HBT}}$ is given by Eqs. (4.45), (4.47). At intermediate values of $t$, we use the same formalism as for the HBT setup, taking the QPC into account in the scattering matrix:

$$\begin{pmatrix} \psi_{2,e} \\ \psi_{2,h} \\ \psi_{4,e} \\ \psi_{4,h} \end{pmatrix} = \frac{1}{2} \begin{pmatrix} \eta_1 - t & \eta_1 + t & r & r \\ \eta_1 + t & \eta_1 - t & -r & -r \\ r & -r & -\eta_2 + t & \eta_2 + t \\ r & -r & \eta_2 + t & -\eta_2 + t \end{pmatrix} \begin{pmatrix} \psi_{1,e} \\ \psi_{1,h} \\ \psi_{3,e} \\ \psi_{3,h} \end{pmatrix} . \tag{4.48}$$

Here, $\eta_{1(2)}$ is the interferometric phase factor for Majorana fermions around the upper (lower) superconductor.

In this case, the average currents do not identically vanish. In fact the conductances $G_{12} = G_{34} = \frac{e^2}{h}|t|$ are proportional to the transmission *amplitude*. This allows to experimentally access the QPC properties. The two remaining conductances $G_{14}$ and $G_{32}$ still vanish.

We now focus on the quantities of interest, namely the current-current correlations $S_{22}$, $S_{44}$, and $S_{24}$. The auto-correlation reads

$$\begin{aligned} S_{22} = &\int_0^\infty dE \ \frac{e^2}{h} R(n_{1,e} + n_{1,h} + n_{3,e} + n_{3,h} - (n_{1,e} + n_{1,h})(n_{3,e} + n_{3,h})) \\ &+ \frac{e^2}{h} T(n_{1,e}(1 - n_{1,e}) + n_{1,h}(1 - n_{1,h}) + (n_{1,e} - n_{1,h})^2 (\mathrm{Re}\,\eta_1)^2) \, , \end{aligned} \tag{4.49}$$

and has two contributions. The first one, multiplying the reflection probability $R = |r|^2$ at the QPC, is the auto-correlation of the interferometer without the point-contact, see Eq. 4.47). The second term, multiplying the transmission probability $T = |t|^2$ at the QPC, is the auto-correlation of the Mach-Zehnder interferometer, see Eq. (4.40). The latter oscillates with twice the phase acquired by a Majorana fermion in the loop. As a consequence, it is not sensitive to vortices in the superconductor but only to the dynamical phase. The first term, proportional to R, is not sensitive to any phase. The cross-correlation

$$S_{24} = -\frac{e^2 R}{h} \int_0^\infty dE \ (n_{1,e} - n_{1,h})(n_{3,e} - n_{3,h}) \, \mathrm{Re}(\eta_1^* \eta_2) \tag{4.50}$$

is equal to $R$ times the cross-correlation without the point contact, see Eq.(4.45). It oscillates with the total phase acquired by a Majorana fermion around the total loop.

### Absence of partition noise

In the light of the results 4.49 and 4.50, we readily see that the resulting $2 \times 2$ correlation matrix, for the two outgoing leads and at a given energy, can be decomposed as

$$S = R \times S_{\mathrm{HBT}} + T \times S_{\mathrm{MZ+MZ}} \, . \tag{4.51}$$

The QPC effectively interpolates between the two limiting cases: surprisingly, there are no mixed terms proportional to $RT$; in other words, while there are the (auto and cross-correlation) noise terms related to the HBT and MZ interferometer present in the structure,

there is no partition noise. This is one of the main results of this section and is deeply rooted in the Majorana nature of the excitations transported along the boundaries of the superconductor.

In the following we give an intuitive explanation of this remarkable feature of Eq. (4.51). Partition noise in the context of an electronic beam splitter is due to the transport of charge in discrete units. An incoming electron is coherently split into e.g. two channels, and in a current measurement the electron will contribute to the current in one, and only one, outgoing channel. The splitting thereby induces current fluctuations proportional to the charge of the electron. Majorana fermions, on the other hand, fail to generate electric current fluctuations since they are neutral. We thus believe that the absence of electronic partition noise predicted by Eq. (4.51) is a signature of channels supporting Majorana fermions. Importantly, this absence occurs while the QPC is proven to actually scatter the fermions because of the dependence on $R$ and $T$.

## 4.4 Full Counting Statistics

In the previous section we have studied the average currents and second-order correlations in various interferometers and found signatures of the transport through Majorana modes. It is natural to ask if other such signatures could hide in higher-order correlations. Therefore we shall investigate the full counting statistics of the Hanbury Brown-Twiss interferometer with the additional QPC, see Fig. 4.6, in order to access correlations at all orders at once.

### 4.4.1 Formalism

In order to compute the outgoing-current moments to all orders easily, it is useful to define the characteristic function $\Lambda(\chi_2, \chi_4)$ [Levitov93]

$$\Lambda(\chi_2, \chi_4) = \langle e^{i(\chi_2 I_2 + \chi_4 I_4)} \rangle = \langle e^{i\chi_2 I_2} e^{i\chi_4 I_4} \rangle \,. \tag{4.52}$$

It is a function of two new parameters $\chi_2, \chi_4$ called counting variables. The usefulness of the characteristic function stems from the relations

$$\langle I_2^m I_4^n \rangle = (-i\partial_{\chi_2})^m (-i\partial_{\chi_4})^n \Lambda(\chi_2, \chi_4)|_{\chi_2=\chi_4=0} \,, \tag{4.53}$$

in other words all the current moments are given by the derivatives of the characteristic function at the origin, $\chi_2 = \chi_4 = 0$. Moreover, the derivatives of $\log \Lambda(\chi_2, \chi_4)$, called the cumulant generating function, are equal to the current cumulants. For example,

$$\langle (\Delta I_2)^2 \rangle \rangle = -\partial_{\chi_2}^2 \log \Lambda(\chi_2, \chi_4)|_{\chi_2=\chi_4=0} \,. \tag{4.54}$$

We now turn to the computation of the characteristic function. In our systems, the currents contain an electron and a hole contribution: $I_j = e(\psi_{j,e}^\dagger \psi_{j,e} - \psi_{j,h}^\dagger \psi_{j,h})$. Therefore the exponent $\chi_2 I_2 + \chi_4 I_4$ in the expression of $\Lambda$ takes the form

$$e\, (\psi_{1,e}^\dagger \psi_{1,h}^\dagger \psi_{3,e}^\dagger \psi_{3,h}^\dagger) S^\dagger \begin{pmatrix} \chi_2 & 0 & 0 & 0 \\ 0 & -\chi_2 & 0 & 0 \\ 0 & 0 & \chi_4 & 0 \\ 0 & 0 & 0 & -\chi_4 \end{pmatrix} S \begin{pmatrix} \psi_{1,e} \\ \psi_{1,h} \\ \psi_{3,e} \\ \psi_{3,h} \end{pmatrix} , \tag{4.55}$$

where $S$ is the scattering matrix of the Hanbury Brown - Twiss interferometer with a QPC given by Eq. (4.48). We denote the diagonal central matrix $\chi$. To evaluate the average in Eq. (4.52), we use the following trick, see [Klich02],

$$Tr(e^{\Gamma(A)}e^{\Gamma(B)}) = \det(1 + e^{A}e^{B})\,, \tag{4.56}$$

where $A, B$ are fermionic operators in the single-particle picture and $\Gamma(A), \Gamma(B)$ are their representation on the Fock space (second quantized operators). Using this formula, we obtain

$$\Lambda = \frac{1}{Z}Tr(e^{-\beta\mathcal{H}_0}e^{i(\chi_2 I_2 + \chi_4 I_4)}) = \frac{1}{Z}\det(1 + e^{-\beta H_0}e^{ieS^\dagger\chi S})\,. \tag{4.57}$$

We now use $Z = \det(1 + e^{-\beta H_0})^{-1}$, $n = \frac{e^{-\beta H_0}}{1+e^{-\beta H_0}}$ the occupation-number operator and $e^{ieS^\dagger\chi S} = S^\dagger e^{ie\chi}S$ to write $\Lambda$ as

$$\Lambda = \det\left(1 + n\left(S^\dagger e^{ie\chi}S - 1\right)\right)\,. \tag{4.58}$$

Or, using the properties of determinants,

$$\Lambda = \det\left(1 + SnS^\dagger\left(e^{ie\chi} - 1\right)\right)\,, \tag{4.59}$$

which is the analogue of the Levitov formula [Levitov93, Klich02].

### 4.4.2 Full counting statistics of the Hanbury Brown-Twiss interferometer

To analyze the full counting statistics of the Hanbury Brown-Twiss interferometer of Majorana fermions, we plug the expression for the scattering matrix (4.48) into the result (4.59). The outcome can be cast into the form

$$\Lambda = 1 + \sum_{s_2,s_4} P_{s_2,s_4}\left(e^{ie(s_2\chi_2 + s_4\chi_4)} - 1\right)\,, \tag{4.60}$$

where $s_{2,4} = -1, 0, +1$ and the probabilities $P_{s_2,s_4}$ depend on the occupation of the leads, the transmission amplitude $t$ of the QPC, and the effective fluxes $\eta_1, \eta_2$. The probabilities are related to charge transfer processes of the structure. The probability $P_{0,0}$ does not contribute to the sum in Eq. (4.60) because it corresponds to processes where no net charge is transmitted to either lead 2 or 4. These processes are still important because they capture the situations where both an electron and a hole are transmitted to the same

outgoing lead. The probabilities are given by

$$\begin{aligned}
P_{\pm,0} =& \frac{1}{8} - 2\alpha\beta\gamma\delta \pm \frac{1}{4}t\ \mathrm{Re}(\eta_1)(\alpha-\beta)(4\gamma\delta+1) + \frac{1}{2}t^2\ (\gamma\delta-\alpha\beta)\,,\\
P_{0,\pm} =& \frac{1}{8} - 2\alpha\beta\gamma\delta \pm \frac{1}{4}t\ \mathrm{Re}(\eta_2)(\gamma-\delta)(4\alpha\beta+1) + \frac{1}{2}t^2\ (\alpha\beta-\gamma\delta)\,,\\
P_{\pm,\pm} =& \frac{1}{16} + \alpha\beta\gamma\delta - \frac{1}{8}(\alpha+\beta)(\gamma+\delta) + \frac{1}{8}\mathrm{Re}(\eta_1\eta_2)(\alpha-\beta)(\gamma-\delta)\\
&\pm \frac{1}{8}t\left(\mathrm{Re}(\eta_1)(\alpha-\beta)(1-4\gamma\delta) + \mathrm{Re}(\eta_2)(\gamma-\delta)(1-4\alpha\beta)\right)\\
&+ \frac{1}{8}t^2\left(\mathrm{Re}(\eta_1\eta_2^*)(\alpha-\beta)(\gamma-\delta) - (\alpha-\gamma)(\beta-\delta) - (\alpha-\delta)(\beta-\gamma)\right)\,,\\
P_{\pm,\mp} =& \frac{1}{16} + \alpha\beta\gamma\delta - \frac{1}{8}(\alpha+\beta)(\gamma+\delta) - \frac{1}{8}\mathrm{Re}(\eta_1\eta_2)(\alpha-\beta)(\gamma-\delta)\\
&\pm \frac{1}{8}t\left(\mathrm{Re}(\eta_1)(\alpha-\beta)(1-4\gamma\delta) - \mathrm{Re}(\eta_2)(\gamma-\delta)(1-4\alpha\beta)\right)\\
&- \frac{1}{8}t^2\left(\mathrm{Re}(\eta_1\eta_2^*)(\alpha-\beta)(\gamma-\delta) + (\alpha-\gamma)(\beta-\delta) + (\alpha-\delta)(\beta-\gamma)\right)\,,
\end{aligned} \tag{4.61}$$

where we introduced the symmetrized occupation numbers

$$\alpha = \frac{1}{2} - n_{1e}\,, \tag{4.62}$$

$$\beta = \frac{1}{2} - n_{1h}\,, \tag{4.63}$$

$$\gamma = \frac{1}{2} - n_{3e}\,, \tag{4.64}$$

$$\delta = \frac{1}{2} - n_{3h}\,, \tag{4.65}$$

to simplify the expressions.

The sum of the probablities yields

$$\sum_{s_2,s_4} P_{s_2,s_4} - P_{0,0} = \frac{3}{4} - \frac{1}{2}(\alpha+\beta)(\gamma+\delta) - 4\alpha\beta\gamma\delta - \frac{1}{2}t^2\left((\alpha-\gamma)(\beta-\delta) + (\alpha-\delta)(\beta-\gamma)\right)\,, \tag{4.66}$$

hence

$$P_{0,0} = \frac{1}{4} + \frac{1}{2}(\alpha+\beta)(\gamma+\delta) + 4\alpha\beta\gamma\delta + \frac{1}{2}t^2\left((\alpha-\gamma)(\beta-\delta) + (\alpha-\delta)(\beta-\gamma)\right)\,, \tag{4.67}$$

since $\sum_{s_2,s_4} P_{s_2,s_4} = 1$.

The probabilities $P_{s_2,s_4}$ take into account all the physical processes that may occur in the interferometer. Processes with $s_i = +1(-1)$ correspond to an outoing electron (hole) in lead i, while processes with $s_i = 0$ correspond to processes with no outoing particles in lead i **or** to processes with an outgoing electron *and* a hole in lead i.

To understand the features of the probabilities in more details, it is useful to distinguish between 5 classes of processes depending on the number of incoming particles they involve: the trivial 0-particle process that contributes solely to $P_{0,0}$; 1-particle processes

that contribute to $P_{0,\pm}$ and $P_{\pm,0}$; 2-particle processes that contribute to $P_{\pm,\pm}$, $P_{\pm,\mp}$, and $P_{0,0}$; 3-particle processes that contribute to $P_{0,\pm}$ and $P_{\pm,0}$; and the trivial 4-particle process that also only contributes to $P_{0,0}$.

### 4.4.3 Factorization of the process probabilities

The limit of the HBT interferometer is readily obtained by setting $t = 0$ in Eq. (4.61). In the opposite limit, $t = 1$, we have two uncorrelated Mach-Zehnder interferometers: we expect that the charactersitic function factorizes, or, equivalently, that

$$P_{s_2,s_4} = P^{(2)}_{s_2} P^{(4)}_{s_4} \,. \tag{4.68}$$

Indeed, it turns out that

$$\begin{aligned} P^{(2)}_{\pm} &= \left(\frac{1}{4} - \alpha\beta \pm \frac{1}{2}\mathrm{Re}(\eta_1)(\alpha-\beta)\right) , \\ P^{(2)}_{0} &= 2\alpha\beta + \frac{1}{2} \,, \end{aligned} \tag{4.69}$$

and equivalently for $P^{(4)}$ with the substitutions $(\alpha, \beta, \eta_1) \to (\gamma, \delta, \eta_2)$, yields a proper factorization of the probabilities for the case $t = 1$.

For the general case, $t \neq 1$, a complete factorization of the form (4.68) is not expected to be possible. However the result (4.69) suggests to introduce the following $t$-dependent quantities

$$\begin{aligned} P^{(2)}_{\pm}(t) &= \frac{1}{2}\left(\frac{1}{2} - 2\alpha\beta \pm t\ \mathrm{Re}(\eta_1)(\alpha-\beta)\right) , \\ P^{(2)}_{0} &= \frac{1}{2} + 2\alpha\beta \,, \end{aligned} \tag{4.70}$$

and similarly for $P^{(4)}$. It is then easily verified that we can write more compactly all the probabilities in Eq. (4.61) as

$$\begin{aligned} P_{0,0} &= P^{(2)}_0 P^{(4)}_0 - \frac{1}{2}r^2\ \left((\alpha-\gamma)(\beta-\delta) + (\alpha-\delta)(\beta-\gamma)\right) , \\ P_{\pm,0} &= P^{(2)}_{\pm}(t) P^{(4)}_0 - \frac{1}{2}r^2\ (\gamma\delta - \alpha\beta) \,, \\ P_{0,\pm} &= P^{(2)}_0 P^{(4)}_{\pm}(t) - \frac{1}{2}r^2\ (\alpha\beta - \gamma\delta) \,, \\ P_{\pm,\pm} &= P^{(2)}_{\pm}(t) P^{(4)}_{\pm}(t) + \frac{1}{8}r^2\ \left((\alpha-\gamma)(\beta-\delta) + (\alpha-\delta)(\beta-\gamma) + \mathrm{Re}\,(\eta_1\eta_2)(\alpha-\beta)(\gamma-\delta)\right) , \\ P_{\pm,\mp} &= P^{(2)}_{\pm}(t) P^{(4)}_{\mp}(t) + \frac{1}{8}r^2\ \left((\alpha-\gamma)(\beta-\delta) + (\alpha-\delta)(\beta-\gamma) - \mathrm{Re}(\eta_1\eta_2)(\alpha-\beta)(\gamma-\delta)\right) . \end{aligned} \tag{4.71}$$

Remarkably all the probabilities factorize into products of two Mach-Zehnder like processes, up to some corrections proportional to the reflection probability $r^2$. In this form, the structure behind the probabilities is much more apparent. Namely, the probabilities (4.70 capture the processes where particles are coming from one source only. The corrections, all proportional to $r^2$ describe the additional correlations that arise when both sources are active.

### 4.4.4 Results

In order to get all cumulants of the outgoing currents, we have to consider the function

$$\frac{1}{h}\int_0^\infty dE\ \log\Lambda = \frac{1}{h}\int_0^\infty dE\ \log\left(1+\sum_{s_2,s_4} P_{s_2,s_4}\left(e^{ie(s_2\chi_2+s_4\chi_4)}-1\right)\right). \tag{4.72}$$

The cumulants $C(m,n)$ are given by the derivatives at the origin

$$C(m,n) = \left[(-i\partial_{\chi_2})^m(-i\partial_{\chi_4})^n\frac{1}{h}\int_0^\infty dE\ \log\Lambda\right]_{\chi_2=\chi_4=0}. \tag{4.73}$$

Let us check first if we can rederive the results of Sec. 4.3. For example, the average current in lead 2 is given by

$$\begin{aligned}\langle I_2\rangle =& C(1,0) = \frac{e}{h}\int_0^\infty dE\ \sum_{s_2} s_2 \sum_{s_4} P_{s_2,s_4}\\ =&\frac{e}{h}\int_0^\infty dE\ (P_{++}+P_{+0}+P_{+-}-P_{-+}-P_{-0}-P_{--})\\ =&\frac{e}{h}\int_0^\infty dE\ t\mathrm{Re}(\eta_1)v_1\\ =&\frac{e}{h}\int_0^\infty dE\ t\mathrm{Re}(\eta_1)(n_{1e}-n_{1h})\,.\end{aligned} \tag{4.74}$$

making contact to the previously obtained result. Similarly the current-current cross-correlation

$$\begin{aligned}S_{24} =& C(1,1) = \frac{e^2}{h}\int_0^\infty dE\ \sum_{s_2,s_4} s_2 s_4 P_{s_2,s_4} - \left(\sum_{s_2,s_4} s_2 P_{s_2,s_4}\right)\left(\sum_{s_2,s_4} s_4 P_{s_2,s_4}\right)\\ =&-\frac{e^2R}{h}\int_0^\infty dE\ (n_{1,e}-n_{1,h})(n_{3,e}-n_{3,h})\,\mathrm{Re}(\eta_1^*\eta_2)\end{aligned} \tag{4.75}$$

is the same as Eq. (4.50).

In order to go further, let us now specify a set of parameters which capture the most interesting physics. Temperature and interferometer asymmetry do not bring any new effects, but only smear out certain quantities. We will thus set $\delta L = 0$ (equivalently we can also study the zero-bias properties even with $\delta L \neq 0$), or $\eta_{1,2} = \pm 1$, and $T = 0$. Moreover we will adopt a symmetric voltage configuration where $V_1 = V_2 = V > 0$ to access the nontrivial multiparticle processes. A plot of the resulting cumulants is shown in Fig. 4.7. Two observations can be drawn from this plot. First, it appears that there is a relation of the form $|C(m,n)| = |C(m+n,0)|$. Second, the cumulants $C(n,0)$ seem to be connected to the cumulants of the binomial distribution , albeit the relation is hard to pinpoint visually. We shall investigate this further in the next section.

The relation $|C(m,n)| = |C(m+n,0)|$ holds because we treat a special case : first $P_{0\pm} = P_{\pm 0} = 0$ and second, for $\eta_{1,2} = \pm 1$, it turns out that either $P_{++} = P_{--} = 0$ or $P_{+-} = P_{-+} = 0$. It then follows that $S(\chi_2,\chi_4)$ is either a function of $\chi_2 - \chi_4$ or a function of $\chi_2 + \chi_4$. The cumulants of the k-th order $C(m,n)$, $m+n=k$, obtained by taking $m$ derivatives of $S$ with respect to $\chi_2$ and $n$ derivatives with respect to $\chi_4$, are thus exactly the same in the latter case (function of $\chi_2+\chi_4$) and only change sign in the former (function of $\chi_2-\chi_4$).

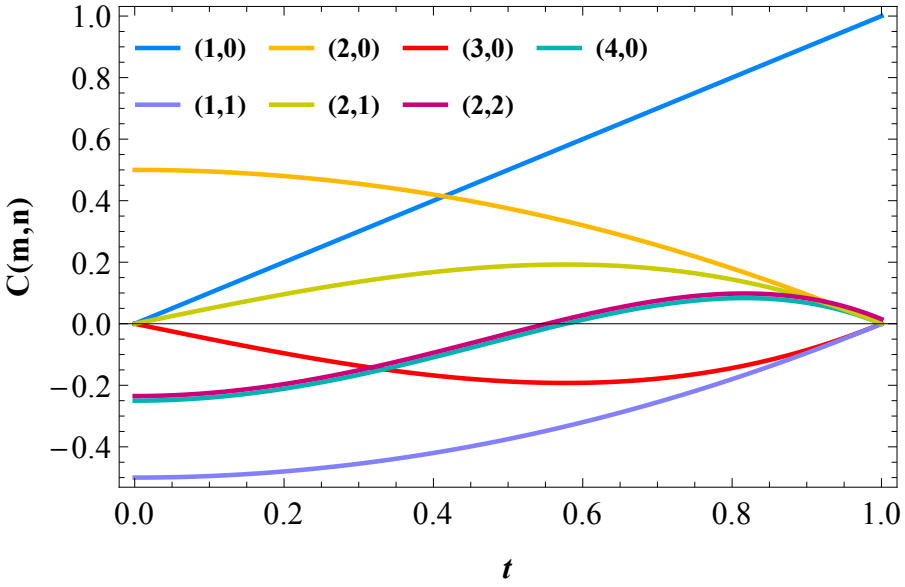


Figure 4.7: Cumulants $C(m,n)$ as a function of $t$ (transmission amplitude of the QPC) at zero temperature and for $\eta_1 = 1$, $\eta_2 = -1$. The vertical axis is in arbitrary units and we set $V_1 = V_2 = e = h = 1$.

### 4.4.5 Half-charge transfers

The cumulants $C(n,0)$ are obtained from the cumulant generating function

$$\log \Lambda(\chi) = \log\left(1 + p_+\left(e^{i\chi} - 1\right) + p_-\left(e^{-i\chi} - 1\right)\right) , \tag{4.76}$$

obtained from the full cumulant generating function (4.59) by summing over the outcomes in lead 4, and where

$$p_\pm = \left(\frac{1 \pm \eta_1 t}{2}\right)^2 \tag{4.77}$$

are the probabilities of transfering an electron or a hole into lead 2. Note that we still assume $T = 0, \eta_{1,2} = \pm 1, V_1 = V_2 = V > 0$.

We are now ready to make the connection with the binomial process. Basically, it turns out that

$$\log \Lambda(\chi) = 2 \log\left(1 + \frac{1+\eta_1 t}{2}(e^{i\chi/2} - 1) + \frac{1-\eta_1 t}{2}(e^{-i\chi/2} - 1)\right) . \tag{4.78}$$

This means that we can interpret unit-charge transfer processes as two independent half-charge transfer processes (notice the 2 multiplying the log and in $\chi/2$). In other words, two independent binomial processes occuring with probability $p = (1+\eta_1)/2$.

The decomposition of unit-charge transfers into two half-charge tranfers strongly suggests the implication of new half-electron (and/or half-hole) particles that always come in pairs. Is this a signature of Majorana fermions? Maybe, but we must remain careful. First, Majorana fermions are *neutral*, not *half charged*. However it might still be possible

to interpret the $\chi/2$ factors as describing *half-fermion* transfers rather than half-charge transfers. Moreover, this decomposition is only valid for a symmetric interferometer, or at zero bias. This could be potentially attributed to a special property of the $k = 0$ Majorana mode (which is self-adjoint) that the $k \neq 0$ modes to not possess.

## 4.5 Conclusion

The results for the zero-temperature conductance and noise properties of normal electron and Majorana interferometers in a two-terminal (Mach-Zehnder) and four-terminal (Hanbury Brown-Twiss) setup are summed up in Table 4.1.

| | Normal | Majorana |
|---|---|---|
| $G_{12}^{\mathrm{MZ}}[e^2/h]$ | $\frac{1}{2}[1+\cos(2\pi\phi/\phi_0)]$ | $\cos(2\pi\phi/\phi_0)$ |
| $S_{22}^{\mathrm{MZ}}[e^3V/h]$ | $\frac{1}{8}[1-\cos(4\pi\phi/\phi_0)]$ | $\frac{1}{2}[1-\cos(4\pi\phi/\phi_0)]$ |
| $G_{12}^{\mathrm{HBT}}[e^2/h]$ | $1/4$ | $0$ |
| $S_{22}^{\mathrm{HBT}}[e^3V/h]$ | $1/4$ | $1$ |
| $S_{24}^{\mathrm{HBT}}[e^3V/h]$ | $-\frac{1}{4}[1+\cos(2\pi\phi/\phi_0)]$ | $-\cos(2\pi\phi/\phi_0)$ |

Table 4.1: Summary of conductance and noise properties of normal electron (as in Ref. [Samuelsson04] for the HBT setup) and Majorana interferometers at zero temperature. In the Mach-Zehnder (MZ) interferometer, 1(2) labels the incoming (outgoing) lead. In the Hanbury Brown-Twiss (HBT) interferometer, 1 and 3 (2 and 4) refer to the incoming (outgoing) leads.

To summarize, we have analyzed a Hanbury Brown-Twiss type interferometer for Majorana fermions. We have calculated its conductance and noise properties. The sign of the cross-correlations of the outgoing currents of the interferometer is predicted to be positive if the parity of the number of vortices threading the superconductor is odd. Our main results are three signatures for the Majorana nature of the transport channels defined by domain walls between superconducting and magnetic regions placed on the surface of a three-dimensional topological insulator. On the one hand, the average charge current in the outgoing leads vanishes since there are symmetric probabilities for outgoing electrons or holes, see the discussion before Eq. (4.42). This vanishing conductance needs to be complemented by a check that the structure is functional, which is provided by the finite current auto-correlation. On the other hand, we find a finite zero-temperature shot noise at the output port of the interferometer even for a vanishing average current reflecting the finite fluctuations of the Majorana particle around charge neutrality. Finally, our calculations predict the absence of electronic partition noise in a quantum point contact, whereas the parameter dependence of the scattering matrix proves that the point contact actually scatters the fermions. These signatures will be an important help in verifying the existence of Majorana excitations in interferometric structures at the surface of topological insulators.

Finally, by studying the full counting statistics of the interferometers we found that the charge transfer processes can be described as two independent half-charge transfers. It is tantalizing to interpret this as a further signature of Majorana-mediated transport, but further investigations are required to promote this to a definitive statement.

# Part II

# Interferometric methods inspired from quantum weak measurements

# Chapter 5

# Weak-value amplification

Chapters 5 and 6 are adapted from the publication:

> G. Strübi and C. Bruder, *Measuring Ultrasmall Time Delays of Light by Joint Weak Measurements*, Phys. Rev. Lett. **110**, 083605.

Twenty years after the proposal [Aharonov88] of Aharonov, Albert, and Vaidman, several experiments have demonstrated the possibility to measure tiny physical effects using the so-called weak-value amplification scheme [Hosten08, Dixon09, Hogan11, Pfeifer11, Gorodetski12, Zhou12, Xu13, Jayaswal14, Salazar-Serrano14]. These ideas have paved the way for new approaches to precision measurements in general, and have triggered a great deal of further theoretical and experimental developments.

Recently, Hosten and Kwiat [Hosten08] were able to experimentally confirm the spin Hall effect of light by measuring a polarization-dependent displacement of a laser beam to a precision of 1 Å using weak-value amplification. Gorodetski *et al.* [Gorodetski12] investigated the plasmonic spin Hall effect. Dixon *et al.* [Dixon09] determined the angle of a mirror to a precision of the order of 500 frad by measuring deflection of light off the mirror. Several experiments were proposed in order to enhance the precision of the measurement of longitudinal phase shifts of light [Brunner10], or amplify the single-photon nonlinearity to a measurable effect [Feizpour11]. An application to charge sensing in a solid-state context has also been put forward [Zilberberg11]. The advantages of weak-value amplification schemes for suppressing technical noise were investigated in [Feizpour11, Starling09, Nishizawa12], and [Kedem12] showed how technical noise could even improve the precision in this scheme. Ways to optimize the initial meter wavefunction were studied in [Susa12].

There was a number of attempts to go beyond the weak-value formalism. This includes, for instance, higher-order expansions for nearly orthogonal pre- and post-selected states [Geszti10, Wu11, Nakamura12, Pang12, Kofman12], or the use of full counting statistics [Di Lorenzo12], and orbital-angular-momentum pointer states [Puentes12]. The effect of decoherence was investigated in Ref. [Knee13a]. The limits of amplification for arbitrary coupling strength were addressed in [Koike11, Zhu11]. Connections of the weak-value formalism with the theoretical tools of precision metrology were made in [Hofmann11, Hofmann12]. Weak values were also related to quasiprobability distributions of incompat-

ible observables [Bednorz10].

The goal of this chapter is to explain what is the weak-value amplification technique, how it works (Sec. 5.2) and why it is useful (Sec. 5.3). We then proceed to study its limitations to understand why a generalization is desirable (Sec. 5.4). To get there we start by reviewing briefly the necessary material that leads to the definition of the weak value introduced in Ref. [Aharonov88].

## 5.1 Basics of quantum measurements

According to the basic postulates of quantum mechanics, the result of any measurement of a system in state $|\psi\rangle$ is an eigenvalue $a$ of an observable $\hat{A}$. Moreover, just after the measurement the state of the system collapses into the respective eigenstate $|a\rangle$ of $\hat{A}$. This implies the intervention of mysterious and nonunitary dynamics outside of the Schrödinger equation. But we shall not dive deeper into this so-called measurement problem. Instead, we are content to stay within the realm offered by the projection postulate.

However, it is possible, we dare say necessary, to go beyond the single-step collapse description of measurement processes. Any real measurement of a *system* $S$ must involve a transfer of information from $S$ to another physical system, a *meter*, $M$. It is perfectly valid to describe this process alone using quantum mechanics without invoking any collapse mechanism. The subsequent transfer of information from the meter to our classical world can then be described satisfactorily with the projection postulate for our purposes. In this section, we shall see how the concepts of measurement strength and weak values arise naturally from this framework.

### 5.1.1 Von Neumann measurements

We describe here in details how the mean value of an observable $\hat{A}$ of a quantum system can be obtained by coupling the system to an external meter degree of freedom, see Fig. 5.1a. The coupling is described by the time-dependent interaction Hamiltonian

$$\hat{H}_I(t) = k\delta(t)\hat{x}\hat{A}\,. \tag{5.1}$$

First, the meter is initialized in a zero-mean Gaussian state

$$\psi_M(p) = \left(\frac{1}{2\pi\Delta^2}\right)^{1/4} \exp(-p^2/4\Delta^2)\,, \tag{5.2}$$

and the system is in the (unknown) state $|i\rangle$. The second step is to let the meter and the system interact. We assume that the internal dynamics of the system and the meter are much slower than the interaction process and can be neglected. The evolution operator reads

$$\hat{U} = \exp\left(-i\int dt\ \hat{H}_I(t)\right) = \exp(-ik\hat{q}\hat{A})\,. \tag{5.3}$$

After the interaction the total state is an entangled superposition of the meter in a Gaussian state peaked at position $ka$ and the system in state $|a\rangle$:

$$|\Psi\rangle = \sum_a |\psi_M(p-ka)\rangle \otimes \langle a|i\rangle\,|a\rangle\ . \tag{5.4}$$

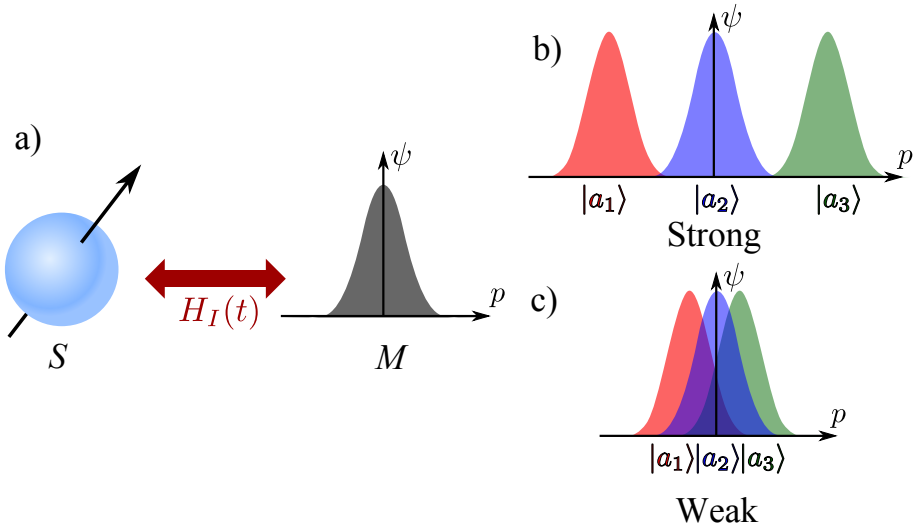


Figure 5.1: (a) A quantum system $S$ and meter $M$ interact according to the Hamiltonian $H_I(t) = k\delta(t)\hat{x}\hat{A}$, where $\hat{A}$ is an observable of $S$ and $\hat{x}$ is the operator of $M$ conjugate to $\hat{p}$. (b) If the interaction constant $k$ is large, the interaction entangles the system and the meter strongly. Each value of the pointer $p$ is unambiguously associated to a single eigenstate $|a_i\rangle$ of $\hat{A}$. (c) For a small interaction constant $k$, the interaction entangles the system and the meter weakly. A readout $p$ of the pointer is associated to a coherent superposition of eigenstates $|a_i\rangle$.

At the last step, the meter pointer $\hat{p}$ is measured projectively (we have not gotten rid of the projection postulate). The probability density $P(p)$ of obtaining the outcome $p$ is given by

$$P(p) = \sum_a |\langle a|i\rangle \psi_M(p - ka)|^2 \tag{5.5}$$

Because of the entanglement in $\Psi$ prior to the projection, the system state is also affected by the projection. The final state is no longer entangled and reads

$$|\Psi\rangle' = |p\rangle \otimes \sum_a \frac{\langle a|i\rangle \psi_M(p - ka)}{\sqrt{P(p)}} |a\rangle \ . \tag{5.6}$$

The collapse of the meter into the eigenstate $|p\rangle$ acts back onto the state of the system; this *back-action* is unavoidable in quantum mechanics [Wiseman10].

The average value of the meter variable $p$ allows us to extract the average value of the observable $\hat{A}$ in the system state $|i\rangle$

$$\langle \hat{p} \rangle = k \langle i| \hat{A} |i\rangle \ . \tag{5.7}$$

The averaging process entails a repetition of the measurement procedure.

There are two qualitatively different situations: either the distance between two peaks, $k\delta a$, is larger than their widths $\Delta$, see Fig. 5.1b; or $k\delta a \leq \Delta$, see Fig. 5.1c. In the first case we speak of a *strong* measurement, in the second case we speak of a *weak* measurement. In a strong measurement, each result of the meter $p$ corresponds to a single eigenvalue $a$

of $\hat{A}$; the system collapses to the state $|a\rangle$. In a weak measurement, a single result $p$ of the meter is compatible with several system states. Correspondingly, the state of the system is less disturbed by the measurement procedure; some degree of coherence between the different eigenstates $|a\rangle$ remains.

### 5.1.2 Kraus operators

It is possible to abstract the meter away in the description of the measurement effect on the system. The idea is to write the whole measurement process using one family of operators $K(p)$, called *Kraus operators*, which act on the system and depend explicitly on the possible measurement outcomes $p$ and implicitly on the meter initial wavefunction and the system-meter coupling.

In our previous example, see Eq. (5.6), we can write the final state of the system as

$$|\psi\rangle' = \frac{K(p)\,|i\rangle}{\langle i|\,K^\dagger(p)K(p)\,|i\rangle}\,, \tag{5.8}$$

where the Kraus operators are given by

$$K(p) = \sum_a \psi_M(p - ka)\,|a\rangle\langle a|\ . \tag{5.9}$$

Moreover, the probability of obtaining the result $p$ is given by

$$P(p) = \langle i|\,K^\dagger(p)K(p)\,|i\rangle\ . \tag{5.10}$$

Note that while the Kraus operators act on the system alone, the measurement outcomes $p$ are really eigenvalues of an observable of the meter.

It is possible to recover the results of the projection postulate by choosing the Kraus operators $K(a) = |a\rangle\langle a|$, where $a$ takes all the values in the spectrum of the system observable $\hat{A}$. Therefore the description of a measurement process using arbitrary Kraus operators is a strict generalization of projective measurements.

The possible outcomes and the form of the operators $K(p)$ are specified by the measurement model. The only necessary condition to impose upon the operators $K(p)$ is the completeness relation

$$\int dp\ K^\dagger(p)K(p) = 1 \tag{5.11}$$

to ensure the normalization of the probability distribution of outcomes. The positive operators $E(p) = K^\dagger(p)K(p)$, called *effects*, form what is sometimes called a *probability-operator-valued measure* (POVM) on the space of outcomes $p$ [Wiseman10].

### 5.1.3 Weak value

The weak value $A_w$ of an observable $\hat{A}$ is defined by

$$A_w = \frac{\langle f|\,\hat{A}\,|i\rangle}{\langle f|i\rangle}\,; \tag{5.12}$$

it depends on the choice of an *initial* state $|i\rangle$, and a *final* state $|f\rangle$. The weak value was first introduced in the seminal work of Aharonov, Albert, and Vaidman [Aharonov88]. In

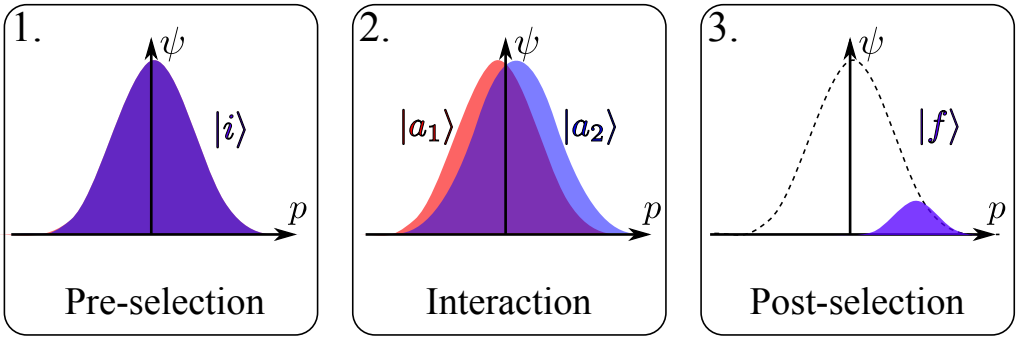


Figure 5.2: The three steps of the weak-value measurement protocol. First, the system and meter are prepared in states $|i\rangle$ and $|\psi_M\rangle$ respectively (pre-selection). Second, they interact according to the evolution operator $\exp(-ik\hat{q}\hat{A})$ and become weakly entangled. Third, the system and the meter are strongly measured. The result is discarded if $S$ is not found in state $|f\rangle$ (post-selection).

a sense, the weak value is a generalization of the more common average value. If the final state is equal to the initial state, $|f\rangle = |i\rangle$, the weak value reduces to an average value over the state $|i\rangle$: $A_w = \langle\hat{A}\rangle_i$.

There are however big differences between weak and average values. Most importantly the weak value $A_w$ is *complex* and *unbounded*, in particular it need not lie within the spectrum of $\hat{A}$. At first sight, on would think that such a quantity is not of foremost significance in quantum measurements. After all the result of a measurement is supposed to be a real eigenvalue of an observable.

The big surprise is that weak values, more precisely the real and imaginary parts thereof, exactly correspond to what is read out on the meter in a certain class of measurement. Of course, it is also the reason why they were introduced in the first place. Let us now see how they arise in practice. We consider a weak measurement of a system $S$ by a meter $M$ with an additional twist: after the interaction between $S$ and $M$, *both* $M$ and $S$ are strongly measured and then the result given by $M$ is kept if, and only if, $S$ is found to be in a particular final state $|f\rangle$. This last process is known as *post-selection*. A pictorial representation of the measurement process is shown in Fig. 5.2.

We consider again the model of a Gaussian meter, see Eq. (5.2). The total state after the interaction between the meter and the system is given by Eq. (5.4). Now we perform the post-selection, i.e. a projective measurement of the system. This step can be described by a Kraus operator *acting on the meter*

$$K(f) = \langle f|\exp(-ik\hat{q}\hat{A})\,|i\rangle\ . \tag{5.13}$$

It $k$ is small we can approximate $K(f)$ by

$$K(f) = \langle f|i\rangle\exp(-ikA_w\hat{q})\,, \tag{5.14}$$

where $A_w$ is defined in Eq. (5.12).

For a purely real weak-value, the Kraus operator (5.14) is nothing but a translation

operator of the meter variable $p$. Therefore a post-selected measurement of $p$ yields

$$\langle \hat{p} \rangle_{\text{p.s}} = k \operatorname{Re} A_w \,. \tag{5.15}$$

this result is to be compared to the standard von Neumann measurement result given in Eq. (5.7). As advertised, the weak value has a direct experimental relevance; it is the direct result of weak measurement with post-selection. The result (5.15) is quite remarkable because the interaction $\exp(-ik\hat{q}\hat{A})$ generates a superposition of translated meter with shifts given by $ka_i$, where $a_i$ are eigenvalues of $\hat{A}$. The interferences between a subset those states are able to generate a shift that can be much larger, since $A_w \gg a_i$ for a suitable choice of the initial and final states $|i\rangle$, $|f\rangle$.

The weak-value protocol opens up the possibility of measuring a nontrivial conditioned average of the conjugate operator $\hat{q}$

$$\langle \hat{q} \rangle_{\text{p.s.}} = \langle \hat{q} \rangle_0 + 2k\Delta_q^2 \operatorname{Im} A_w \,, \tag{5.16}$$

where $\langle \hat{q} \rangle_0$ is the average in the initial state of $M$. Note that without post-selection the average is trivially $\langle \hat{q} \rangle = \langle \hat{q} \rangle_0$. It is therefore possible to measure both the real and imaginary parts of the weak value.

#### Validity of the weak-value approximation

Equation (5.14) is exact up to first order in the expansion of the exponential, but higher orders will deviate. We thus require the higher order to be negligible, i.e. $|kA_w\hat{q}|^2 \ll 1$. This has formally no meaning as $\hat{q}$ is not bounded and this condition is never satisfied. In fact we want $|kA_wq|^2 \ll 1$ for those values of $q$ where $\psi_M(q)$ is not negligibly small. Therefore the condition of validity for weak-value measurements reads

$$|kA_w\Delta_q|^2 \ll 1 \,. \tag{5.17}$$

As a consequence, the shift $\langle \hat{q} \rangle_{\text{p.s.}} - \langle \hat{q} \rangle_0$, see Eq. (5.16), cannot exceed $\Delta_q$, the initial spread of $q$.

### 5.1.4 How the measurement of a spin component of a spin-1/2 particle can turn out to be 100?

To give a concrete example, we now review the original proposal [Aharonov88] of Aharonov, Albert, and Vaidman of a weak-value measurement of the spin of an electron by a Stern-Gerlach apparatus. In their scheme, a beam of electrons with a definite initial state

$$|\psi\rangle = \Delta^{-3/2}(2\pi)^{-3/4} e^{-(x^2+y^2+z^2)/4\Delta^2} e^{-ip_0 y} \left(\cos(\alpha/2)\,|{\uparrow_x}\rangle + \sin(\alpha/2)\,|{\downarrow_x}\rangle\right) \tag{5.18}$$

is sent through two Stern-Gerlach devices. The electrons propagate along the $y$-axis, the $x$ and $z$ axes are transverse. The first device performs a weak measurement of the $z$-component of the spin. It can be described by the evolution operator

$$U = \exp\left(i\mu \frac{\partial B_z}{\partial z} \hat{z}\hat{\sigma}_z\right) \,, \tag{5.19}$$

where $(\partial B_z/\partial z)$ is a weak magnetic field gradient along $z$, $\mu$ is the magnetic moment of the electron, and $\hat{\sigma}_z$ is the Pauli matrix in spin space. This interaction imparts a small spin-dependent momentum kick to the electrons in the $z$ direction. The second Stern-Gerlach device measures strongly the $x$ component of the spin. Finally, the $z$ component of the position of the electrons with spin $|\uparrow_x\rangle$ is measured on a screen.

In our notations, the role of the system $S$ is played by the spin of the electrons. The meter $M$ degree of freedom is the $z$ component of the position of the electron. So, a single particle plays the role of both $M$ and $S$. The initial state of $S$ is $|i\rangle = \cos(\alpha/2)\,|\uparrow_x\rangle + \sin(\alpha/2)\,|\downarrow_x\rangle$, and the final state is $|f\rangle = |\uparrow_x\rangle$. The weak-value of $\hat{\sigma}_z$ reads

$$(\sigma_z)_w = \tan(\alpha/2)\,. \tag{5.20}$$

The measured conditional position is thus

$$\langle z\rangle_{\text{p.s.}} = \ell\frac{\langle p_z\rangle_{\text{p.s.}}}{p_0} = \frac{\ell}{p_0}\mu\frac{\partial B_z}{\partial z}\tan(\alpha/2)\,, \tag{5.21}$$

where $\ell$ is the distance between the first Stern-Gerlach device and the measuring screen. The weak-value $(\sigma_z)_w$ can be made very large by taking $\alpha \to \pi$, say $(\sigma_z)_w = 100$. In that sense, the measured shift corresponds to non-post-selected electrons with a $z$-spin component of 100. We want to stress the "as-if" character of the interpretation; the actual spin component of an electron in the experiment is $\pm 1/2$. In particular, the measured value is not directly a spin value and this led to some controversy early on [Peres89, Leggett89] about the relevance of this scheme and weak values in general.

Aharonov, Albert, and Vaidman also commented in the same work that we can turn the scheme around to measure small magnetic field gradients. The idea is that a large weak value amplifies $(\partial B_z/\partial z)$ in the measurement of $\langle z\rangle_{\text{p.s.}}$, see Eq. (5.21). This observation forms the basis of the weak-value amplification scheme, which we develop in Sec. 5.2.

### 5.1.5 Measuring the wavefunction

One nice application of the concept of weak value is the ability to directly measure the wavefunction $\psi(x)$ itself (*not* only its modulus squared) as proposed in Ref. [Lundeen11]. For this, take the operator $C = |x\rangle\langle x|$ and post-select on the state $|p = 0\rangle$ (of the system, not the meter). Then

$$C_w = \frac{\langle p = 0|x\rangle\langle x|\psi\rangle}{\langle p = 0|\psi\rangle} = \frac{1}{\tilde{\psi}(p = 0)}\psi(x)\,, \tag{5.22}$$

where $\tilde{\psi}(p = 0)$ is the component of the wavefunction at zero momentum. Now by scanning over each value of $x$ and measuring both components of the weak value, we obtain the full wavefunction up to a global factor $\tilde{\psi}(p = 0)^{-1}$ which we can remove by a normalization condition. This is a somewhat amazing result, the wavefunction acquires a physical reality: it is directly measurable. Granted we have to repeat many actual measurement steps (this might provide a loophole for epistemologists) but it is still a big step forward from the view that only $|\psi(x)|^2$ is measurable. This wavefunction measurement was realized experimentally for the transverse wavefunction of a single photon [Lundeen11]. In the same spirit, weak measurements were used to "measure the trajectory" of photons in a double-slit experiment [Kocsis11].

## 5.2 Weak-value amplification

A weak-value amplification experiment is in its essence nothing but a weak-value measurement. However the weak value itself is no longer a goal but rather an amplification tool. Our goal is to measure the coupling constant $k$ that couples a system and a meter through an evolution operator of the type $\hat{U} = \exp(ik\hat{A}\hat{q})$, where $\hat{A}$ acts on the system, and $\hat{q}$ acts on the meter. For convenience we repeat the outcome of weak-value measurement, see Eqs.(5.15,5.16), here

$$\langle \hat{p} \rangle_{\text{p.s}} = k \operatorname{Re} A_w \,, \tag{5.23}$$

$$\langle \hat{q} \rangle_{\text{p.s.}} = 2k\Delta_q^2 \operatorname{Im} A_w \,. \tag{5.24}$$

From these equations we easily understand the idea of the weak-value amplification technique: we can use a tailored large weak value to amplify a (small) "coupling constant" $k$ of interest. It is also clear that there are two flavours of weak-value amplification; we may use either the real part of the weak value or its imaginary part.

The shift of interest to the coupling constant may appear strange at first sight. However it is precisely what is interesting in some cases. For instance, the spin Hall effect of light [Hosten08] is a minute coupling between the polarisation and transverse position of photons that occur at the interface of materials with different indices of refraction. The coupling translates into a polarisation dependent transverse displacement of light traversing the interface. The displacement is very small, of the order of a few nanometers; this effect naturally realizes a weak measurement of the light polarization, where the role of the meter is played by the tranverse position of the light. A direct measurement of the displacement is beyond the resolution of photodetectors for direct measurement. This is where the weak-value amplification technique enters the game [Hosten08].

We now want to study weak-value amplification from a quantitative standpoint. We start with a nonamplified technique and compare it to real and imaginary weak-value amplification. In particular, we are interested to see how the signal-to-noise compares in the two cases and what are the technical advantages and drawbacks of the methods.

### 5.2.1 Scheme without amplification

The naive method to measure $k$, without amplification, is a simple three-step process very similar to a von Neumann measurement:

1) Prepare the two-level system in a definite, known, state $|i\rangle$ and the meter in, say, the Gaussian state $\psi_M(p) \propto \exp(-p^2/4\sigma^2)$.

2) Let the system and meter interact and evolve according to $\hat{U}$.

3) Readout the meter, *i.e.* measure strongly $\hat{p}$.

The process is repeated $N$ times and produces the set of $N$ results $\{p_i\}$. We now take the statistical average $\bar{p} = \sum p_i/N$ to obtain an estimate of the quantum-mechanical average $\langle \hat{p} \rangle = k \langle i | A | i \rangle$ from which it is easy to extract the desired value of $k$. Even in the absence of technical noise, the results will display Gaussian fluctuations due to the original

uncertainty $\sigma$ of $\hat{p}$ in the initial state of the meter. This leads to the signal-to-noise ratio

$$\mathrm{SNR} = \sqrt{N}\,\frac{k\langle\hat{A}\rangle}{\sigma}\,, \tag{5.25}$$

that displays the statistical scaling $\sqrt{N}$ because the $N$ measurements are independent.

### 5.2.2 Real-weak-value amplification

The amplification using the real part of the weak value is a four-step process. The first three-steps are the same as in the nonamplified case, but there is a fourth step consisting of the post-selection.

4) Measure strongly the system and see if it is found in a chosen state $|f\rangle$. If not, *discard* the measurement result $p_i$ of the meter.

The process is repeated $N$ times but it does *not* produce $N$ outcomes because of the post-selection. Instead it yields on average $P_{\mathrm{ps}}N$ outcomes $p_i$, where $P_{\mathrm{ps}}$ is the post-selection probability. This whole scheme is essentially a weak-value measurement provided that $k$ is small enough to satisfy the weak-value condition $k|A_w|/\sigma \ll 1$. In that case we also have the relation $P_{\mathrm{ps}} = |\,\langle f|i\rangle\,|^2$.

This time, the statistical average $\bar{p}$ provides an estimate of $\langle\hat{p}\rangle_{\mathrm{p.s.}} = k\,\mathrm{Re}\,A_w$. In a certain sense, the signal is thus amplified by the *amplification factor*

$$\mathcal{F} = \frac{\mathrm{Re}\,A_w}{\langle\hat{A}\rangle} = \frac{\mathrm{Re}(\langle f|\,\hat{A}\,|i\rangle)}{\langle i|\,\hat{A}\,|i\rangle}\,\frac{1}{\mathrm{Re}(\langle f|i\rangle)}\,, \tag{5.26}$$

which is a figure of merit for this scheme.

By a clever choice of the initial and final states $|i\rangle\,, |f\rangle$ it is thus possible to obtain a very large amplification factor. This is the core of the weak-value amplification method. However, the post-selection adds statistical noise: only $P_{\mathrm{ps}}N$ trials produce an output. Therefore, the signal-to-noise ratio

$$\mathrm{SNR} = \sqrt{P_{\mathrm{ps}}N}\,\frac{k\,\mathrm{Re}(A_w)}{\sigma} = \sqrt{N}\,\frac{k\,\mathrm{Re}(\langle f|\,\hat{A}\,|i\rangle)}{\sigma} \tag{5.27}$$

is essentially of the same order of magnitude as in the nonamplified case; actually, it can only be lower. This result may sound disappointing, but it is also expected; there is no black magic there, and it would have been strange indeed that by *throwing out* measurement results we obtain a better signal-to-noise ratio! In fact, the converse is true: it is surprising that the signal-to-noise ratio does not show a dramatic decrease when $P_{\mathrm{ps}} \ll 1$ and most of the meter readouts are ignored.

An important question remains: why bother with the weak-value amplification if there is no increase in the signal-to-noise ratio? The answer is hidden in the advantages of the method when a finite detector resolution and technical noise are considered. But before analyzing these in detail we briefly expose the imaginary-weak-value amplification.

### 5.2.3 Imaginary-weak-value amplification

The imaginary weak-value amplification is almost the same as its real counterpart. The only difference lies in the step 3 of the above procedure:

3') Readout the meter, but this time measure strongly the conjugate operator $\hat{q}$.

Note that $\hat{q}$ is also the operator that appears in the evolution operator $\hat{U} = \exp(ik\hat{A}\hat{q})$. This means that the conjugate operator of $\hat{q}$ need not appear in the formalism of imaginary-weak-value amplification. As a consequence a quantum description of the meter is superfluous; a probabilistic, but *classical*, description is enough. Namely, if we start with a centered probability density $p_0(q)$ for the meter (corresponding to $|\psi_M(q)|^2$ in a quantum description) the probability density $p(q)$ for the outcomes $q_i$ reads

$$p(q) = p_0(q)(1 + 2k\,\mathrm{Im}(A_w)q)\,. \tag{5.28}$$

In particular, no knowledge of the phase of $\psi_M(q)$ is necessary. The mean-value of $q$ is given by $\langle q\rangle_{\mathrm{p.s.}} = 2\Delta_q^2\,\mathrm{Im}(A_w)k$, where $\Delta_q^2 = \int dq\, p_0(q)q^2$ is the initial variance of $q$. By analogy to Eq. (5.26), we may again define an amplification factor

$$\tilde{\mathcal{F}} = 2\Delta_q^2 \frac{\mathrm{Im}\, A_w}{\langle \hat{A}\rangle}\,, \tag{5.29}$$

which can be made large by an appropriate choice of post-selection and also by an increase of $\Delta_q^2$. As we shall see later, the amplification factor is *not* a central quantity in imaginary weak-value amplification, unlike for its real counterpart.

The signal-to-noise does not have a more favourable dependence on $\Delta_q \sim 1/2\sigma$ (valid for a meter in a pure state that saturates the Heisenberg uncertainty inequality) as in the other two cases

$$\mathrm{SNR} = \sqrt{P_{\mathrm{ps}}N}\,2k\Delta_q\,\mathrm{Im}(A_w) \approx \sqrt{N}\,\frac{k\,\mathrm{Im}(\langle f|\,\hat{A}\,|i\rangle)}{\sigma}\,. \tag{5.30}$$

Again, this is a disappointing result. However, note that without post-selection it is simply not possible to extract a value for $k$ from a $\hat{q}$ measurement, for without post-selection $\langle\hat{q}\rangle = 0$. Depending on the underlying physical situation it might provide an advantage. The utility of the method will become clear in the next section.

### 5.2.4 Comparison

To summarize, weak-value amplification does not provide any advantage in the signal-to-noise ratio. However, it also does not diminish it even if most of the results are discarded by post-selection. Moreover, weak-value amplification does increase the values of the signal read at the detector while decreasing its power. Finally, imaginary-weak-value amplification does not rely on the quantum coherence of the meter. As we shall now see, all those properties have interesting consequences for the practical application of weak-value amplification in real-life scenarios where noise is unavoidable and detectors imperfect.

## 5.3 Benefits of weak-value amplification

### 5.3.1 Detector resolution

We start with the most obvious, and perhaps most important, technical advantage offered by the weak-value amplification technique. If the resolution of the detector $\delta p$ (smallest measurable shift in $p$) is the limiting factor for a nonamplified measurement, the real-weak-value amplification helps by enlarging the signal by the amplification factor $\mathcal{F}$ (5.26). This leads to an effectively better resolution $\delta p/\mathcal{F}$.

Moreover, the imaginary-weak-value amplification technique allows us to measure $q$ instead of $p$. This alternative may already provide an advantage. Moreover, the signal is also multiplied by $\mathrm{Im}(A_w)$ and $\Delta_q^2$, but strictly speaking we cannot speak of amplification without a reference value; imaginary weak-value amplification opens up a new type of measurements. In practice, the scheme is advantageous if $\left[\mathrm{Im}(A_w)\Delta_q^2\right]^{-1}\delta q < \delta p$, where $\delta q$ is the resolution of the $q$ detector.

### 5.3.2 Detector noise

The benefit of weak-value amplification in the presence of detector noise is twofold. First, in the presence of detection white noise the effective detector resolution is decreased. This leads to an advantage of amplified techniques for the same reasons as in intrinsic-resolution-limited measurements. Second, the post-selection makes the signal-to-noise ratio more robust to noise with long correlation times [Feizpour11], where long means larger than the typical interval between two meter readouts. To understand this, we now introduce a simple noise model [Starling09, Feizpour11, Knee13b, Kedem12, Jordan13]. The $i$-th signal $s_i$ measured is given by the sum of the previously considered $p_i$ plus a technical noise $\xi_i$

$$s_i = p_i + \xi_i \,. \tag{5.31}$$

The technical noise has a correlation time $\tau_c$

$$\langle \xi_i \xi_j \rangle = J^2 \exp\left(\frac{-|t_i - t_j|}{\tau_c}\right) , \tag{5.32}$$

where $t_i$ is the time at which the $i$-th detection is carried out, and $J^2$ is the noise magnitude. The signal $\bar{s} = \langle \hat{p} \rangle$ is unchanged, but its fluctuations are enhanced by the additional noise

$$(\Delta s)^2 = \frac{1}{N}\sigma^2 + \frac{1}{N^2}\sum_{i,j=1}^{N} \langle \xi_i \xi_j \rangle \,, \tag{5.33}$$

where $\sigma$ is again the intrinsic fluctuation of the meter variable $p$.

We now compute the effect of the noise on the signal-to-noise ratio. In the nonamplified scenario, for a total measurement time $T$ and a detection rate $\Gamma$, we have $N = \Gamma T$ and we can replace $\langle \xi_i \xi_j \rangle = J^2 \exp(-|i-j|/\Gamma\tau_c)$. It is now possible to compute the fluctuations

of the signal explicitly

$$\begin{aligned}(\Delta s)^2 &= \frac{1}{N}(\sigma^2+J^2)+\frac{2J^2}{N^2}\sum_{i=2}^{N}\exp(-i/\Gamma\tau_c)\sum_{j=1}^{i-1}\exp(j/\Gamma\tau_c)\\ &= \frac{1}{N}(\sigma^2+J^2)+\frac{2J^2}{N^2}\sum_{i=1}^{N}\exp(-i/\Gamma\tau_c)\frac{\exp(1/\Gamma\tau_c)-\exp(i/\Gamma\tau_c)}{1-\exp(1/\Gamma\tau_c)}\\ &= \frac{1}{N}(\sigma^2+J^2)+\frac{2J^2}{N^2(1-\exp(1/\Gamma\tau_c))}\left(\frac{1-\exp(-N/\Gamma\tau_c)}{1-\exp(-1/\Gamma\tau_c)}-N\right). \end{aligned} \tag{5.34}$$

There are several interesting limits: (1) the white-noise limit $\Gamma\tau_c \ll 1$; (2) the long-correlation-time limit $1 \ll \Gamma\tau_c \ll N$; (3) the very-long-correlation-time limit $N \ll \Gamma\tau_c$. In those cases we can simplify the fluctuations of the signal to

$$(\Delta s_1)^2 = \frac{1}{\Gamma T}(\sigma^2+J^2)\,, \tag{5.35}$$

$$(\Delta s_2)^2 = \frac{1}{\Gamma T}(\sigma^2+J^2)+2J^2\frac{\tau_c}{T}\,, \tag{5.36}$$

$$(\Delta s_3)^2 = \frac{1}{\Gamma T}\sigma^2+J^2\,. \tag{5.37}$$

As we can see a higher measurement rate $\Gamma$ is useful to reduce the delta-correlated noise. However, for time-correlated noise there is a part that is independent of the measurement rate. This is expected because measuring faster than the noise correlation time does not help us to average out the noise.

With weak-value amplification, the measurement rate drops by a factor $P_{\rm ps}$ due to post-selection: $\Gamma \to P_{\rm ps}\Gamma$. Therefore the white-noise-induced fluctuations are also increased. On the other hand, the signal is also increased by a factor of roughly $1/\sqrt{P_{\rm ps}}$. Therefore, the signal-to-noise ratio remains unchanged in the presence of white noise, case (1). For long correlation times, the signal-to-noise ratio is larger with weak-value amplification. In particular, for case (3), the signal-to-noise ratio is capped (for $T \longrightarrow \infty$) to

$$\mathrm{SNR} = k\langle\hat{A}\rangle/J \tag{5.38}$$

without amplification, versus the larger bound

$$\mathrm{SNR}_{\rm real} = k\,\mathrm{Re}(A_w)/J = \mathcal{F}\times\mathrm{SNR} \tag{5.39}$$

with real weak-value amplification, where the amplification factor $\mathcal{F}$, see Eq. (5.26), is again a figure of merit. Using the imaginary weak-value scheme the signal-to-noise ratio is capped to

$$\mathrm{SNR}_{\rm im} = 2k\,\mathrm{Im}(A_w)\Delta_q^2/\tilde{J}\,, \tag{5.40}$$

where $\tilde{J}$ characterizes the strength of noise on the measurement of $q$.

To conclude, the amplification does not apparently increase the signal-to-noise ratio in the presence of technical noise with a white spectrum. However, these calculations assume an infinite detector resolution. If white noise leads to an effective lower resolution weak-value amplification still helps. Moreover, and this is the key point, weak-value amplification effectively reduces the effect of technical noise with long correlation times. This is especially desirable to deal with low-frequency noise such as the "$1/f$" electronic noise for instance.

### 5.3.3 Detector saturation

To explain this technical advantage, we briefly explain how a typical experiment using weak-value amplification works [Hosten08]. The role of the meter is taken by the transverse position of a photon, while the role of the system is played by its polarization. The polarization and transverse position are then entangled by some effect we want to measure. Then the photon traverse a polarizer to post-select a particular polarization (final state $|f\rangle$). Finally, the succesfully post-selected photons, and only those, hit a photodetector to measure their transverse position. A stringent post-selection thus allows the experimentalist to either use a cheaper photodetector with a lower saturation rate, or to increase the input power, and thereby also increase the signal-to-noise ratio, without saturating the detector. This is another key technical advantage of the weak-value amplification scheme [Starling09].

### 5.3.4 Real versus imaginary weak-value amplification

Despite the superficial similarity, there is a deep conceptual difference between real and imaginary weak-value amplification. As we have already shown, there is in fact no need to treat the meter as a quantum system for the imaginary weak-value amplification. Real-weak-value amplification, on the contrary, requires full quantum coherence of the meter to work at its full potential. For instance, if the meter is initially in a mixed state it makes no difference to the imaginary weak-value method. On the other hand, it decreases dramatically the signal-to-noise ratio of the real weak-value scheme.

As an example we consider the initial meter wavefunction

$$\psi_M(p) = (\sigma\sqrt{2\pi})^{-1/2} e^{-(p-p_0)/4\sigma^2}\,, \tag{5.41}$$

where $p_0$ is a random displacement that varies from run to run according to a Gaussian distribution of standard deviation $\Delta_0$; in practice this corresponds to, *e.g.*, beam jitter. In this situation the signal-to-noise ratios for the real and imaginary schemes read

$$\mathrm{SNR}_{\mathrm{real}} = \frac{k\,\mathrm{Re}(A_w)}{\sqrt{\sigma^2+\Delta_0^2}}\,, \tag{5.42}$$

$$\mathrm{SNR}_{\mathrm{im}} = \frac{2k\,\mathrm{Im}(A_w)}{\sigma}\,. \tag{5.43}$$

Comparing to Eqs. (5.27) and (5.30) respectively shows that the signal-to-noise ratio decreases only for the real weak-value amplification scheme. A similar situation arises when considering the effect of decoherence [Knee13a].

On the other hand, as is already apparent from Eq. (5.30), a classical noise affecting the variable $q$ prior to the weak interaction is in fact *beneficial* to the signal-to-noise ratio of the imaginary weak-value technique [Kedem12, Jordan13].

## 5.4 Limits to the amplification

The amplification provided by weak-value technique, see Eqs. (5.26, 5.29), is obtained by cleverly choosing and initial and final state to get a large weak-value $A_w = \langle f|\,\hat{A}\,|i\rangle\,/\,\langle f|i\rangle$.

Therefore, it seems that the amplification can be arbitrarily large by picking almost orthogonal initial and final states $\langle f|i\rangle \approx 0$. We give three important limiting factors on the amplification.

The first, fundamental, reason is tied to the weakness condition: the whole formalism is only true in the regime of validity of weak-values $|kA_w\Delta_q|^2 \ll 1$, see Eq. (5.17). In fact, a straightforward calculation shows that the amplification factor goes to zero for $\langle f|i\rangle \longrightarrow 0$ when leaving the regime of validity of the weak-value approximation.

The second source of limitation is the dual to the detector saturation advantage of Sec. 5.3.3. On the one hand, by reducing the post-selection probability $P_{\rm ps}$ the detector is less prone to saturation issues. On the other hand, having less "good" counts at the detector makes the experiment more sensitive to "bad" counts such as stray photons hitting the detector.

The third limitation comes from experimental imperfections: the pre- and post-selection cannot be perfect and some non-zero overlap $\langle f|i\rangle$ remains. In practice, this is often encountered first [Hosten08, Dixon09, Starling09]. Moreover, technical noise plaguing the post-selection can be the overall bottleneck to the ultimate precision of the experiment [Brunner10]. Let us study in more details how such a noise affects the measurements.

#### Pre- and post-selection technical noise

We consider a two-level system with initial and final states written on the Bloch sphere as

$$|i\rangle = \cos\frac{\theta_i}{2}\,|1\rangle + e^{i\phi_i}\sin\frac{\theta_i}{2}\,|2\rangle \tag{5.44}$$

$$|f\rangle = \cos\frac{\theta_f}{2}\,|1\rangle + e^{i\phi_f}\sin\frac{\theta_f}{2}\,|2\rangle\ . \tag{5.45}$$

We are interested in the weak value of the $\sigma_z$ operator

$$(\sigma_z)_w = \frac{\cos\theta_i + \cos\theta_f + i\sin\theta_i\sin\theta_f\sin(\phi_f-\phi_i)}{1+\cos\theta_i\cos\theta_f+\sin\theta_i\sin\theta_f\cos(\phi_f-\phi_i)}\,. \tag{5.46}$$

To obtain a large and purely imaginary $(\sigma_z)_w$ we choose $\theta_i = \theta_f = \pi/2$ and $\phi_f - \phi_i = \pi - \phi$, with $\phi \ll 1$, which yields $(\sigma_z)_w \approx 2i/\phi$. A very small $\phi$ thus leads to large amplification factors.

In practice, there is an uncertainty $\delta\phi$ on the value of $\phi$ that originates from either systematic errors or technical noise. The consequent uncertainty $\delta(\sigma_z)_w \approx -2i\delta\phi/\phi^2$ becomes too large to deal with for $\phi \gtrsim \delta\phi$. The amplification factor due to weak-values is thus limited to a fraction of $1/\delta\phi$.

## 5.5 Conclusion

Weak-value amplification is a new and successful technique that has found many applications in precision measurements. In this chapter, we hope to have convinced the reader that discarding most of the signal, by virtue of the post-selection process, is a good idea in the context of precision measurements of small effects. If we had to give an intuitive explanation to this counterintuitive result, we would say that the post-selection process

concentrates the useful information into fewer actual detections, so that each individual detection is somehow more robust to the deleterious effect of technical noise.

Unfortunately, a large weak value also amplifies pre- and post-selection technical noise. Despite all the strengths of the weak-value amplification method, this strikes as a great limitation. This intrinsic flaw cannot be overcome without modifying slightly the weak-value amplification protocol. It is the main goal of the next chapter to provide an alternative scheme that combines most of the advantages of weak value amplification without the drawbacks listed in Sec. 5.4.

# Chapter 6

# Joint weak measurements

As advertised in the conclusion of the previous section, the goal of the present chapter is to provide a generalization of the weak-value amplification scheme. Section 6.1 presents elements of the underlying statistical concepts to our method. We then apply these concepts to weak measurements in Sec. 6.2. This will make clear that weak-value amplification is not always optimal. In Sec. 6.3 we give a solution to the problem of pre- and post-selection noise that limits the smallest measurable of the weak-value method in a Mach-Zehnder interferometer setup [Brunner10].

#### Scale analysis

To understand the logic that leads to our generalization of the weak-value amplification scheme, we start with a rough analysis of scales involved in the problem. This will shed light on the exact role played by large weak values in the amplification mechanism. Again, the situation is the following: some interaction described by $U = \exp(ik\hat{q}\hat{A})$ is given and we want to extract the value of $k$ by measuring the effect of $U$ on a couple system and meter. We assume that $\hat{A}$ is an operator acting on a small system, think of a spin-1/2, while $\hat{q}$ is a meter continuous degree of freedom, conjugate to the operator $\hat{p}$. We distinguish between two general strategies to measure $k$.

First, consider a $p$ measurement. The natural $p$ length scale is given by $k$. Without weak-value amplification we need a detector resolution $\delta p \lesssim k$ to measure $k$. With weak-value amplification we must resolve shifts of the order of $k\mathrm{Re}A_w$.

Second, we consider a $q$ measurement. The $q$ length scale is less obvious. Unconditioned measurement of $q$ are trivial: $U$ only induces a phase shift that depends jointly on the state of the system and on $q$. To obtain some information, it is crucial to condition the measurement of $q$ with a measurement on the system. The imaginary weak-value amplification scheme extracts *some* of the correlations between $q$ and the system, and leads to shifts of the order of $k\Delta_q^2\mathrm{Im}A_w$. The question is: does the imaginary weak-value amplification exploit the correlations to their full potential? Can we obtain more information on $k$ by a more general scheme?

**Exploiting the full correlations**

The obvious way to generalize the imaginary weak-value amplification scheme is to replace the post-selection by a full joint measurement. That is correlating the measurement of $q$ with a complete basis $\{|s\rangle\}$ of the space of the system. After the interaction $U$, the joint probability of finding the meter in state $|q\rangle$ and the system in state $|s\rangle$ is given by

$$p(q, s|k) = \left|\langle s| e^{-ikq\hat{A}} |i\rangle\right|^2 p_0(q)\,, \tag{6.1}$$

where $p_0(q)$ is the initial meter distribution. We call this procedure *joint weak measurement* to contrast it to post-selected weak measurements that lead to the weak-value amplification. If we perform an experiment, we obtain a set of measurement results $\{q_i, s_i\}$ distributed according to $p(q, s|k)$. To go further, we need a procedure to estimate $k$ from the data $\{q_i, s_i\}$; this is the topic of the next section.

## 6.1 Parameter estimation

Although our ultimate goal is to apply parameter estimation to weak measurements, we take a slighlty more general viewpoint in this section. Suppose we are interested in a quantity $\lambda \in \mathbb{R}^m$ that characterizes the state of the quantum system. A practical meaning of a *measurement* of $\lambda$ is given by the following two-step process: first we choose a relevant observable $A$ of the quantum system and measure as precisely as possible its probability distribution $p_A(a)$; second we *estimate* the value of $\lambda$ from the measured $p_A(a)$. While the first step is mainly the experimentalist's burden, solutions to the theoretical challenges raised by the second step are the crux of this section. We shall only introduce the necessary concepts for us. For a much more detailed discussion see [Helstrom76].

### 6.1.1 Maximum-likelihood estimation

Let us step back for a moment from the physical context of the problem and tackle the problem from a purely statistical point of view. The goal is the following: estimate the value of a parameter $\lambda_0 \in \mathbb{R}^m$ from a sample $\{x_1, x_2, \ldots, x_N\} \in \mathbb{R}^N$ distributed according to probability distribution $p(x|\lambda_0)$. We assume that we know the exact probability distribution $p(x|\lambda)$ for all the possible values of $\lambda$; our goal is to find a $\lambda$ that fits best with the observed sample. Formally we are looking for a function

$$\hat{\lambda} : \mathbb{R}^N \longrightarrow \mathbb{R}^m \tag{6.2}$$

which maps the sample to an estimate $\hat{\lambda}(x_1, \ldots, x_N)$ of the true value $\lambda_0$. The map $\hat{\lambda}$ is called an *estimator* of $\lambda$. Several properties are desirable for estimators in general. First we would like to have an *unbiased* estimator, namely

$$\langle\hat{\lambda}\rangle = \int dx^N\ \hat{\lambda}(x_1, \ldots, x_N) p(x_1|\lambda_0) \cdots p(x_N|\lambda_0) = \lambda_0\,, \tag{6.3}$$

where we assumed all sample points to be independent from each other. Eq. (6.3) says that, while for a given sample the estimator deviates from the value $\lambda_0$, an unbiased estimator

will yield $\lambda_0$ on average. The second property is called *efficiency* of the estimator and quantifies the standard deviation of the estimator. We shall consider it again below when we derive the Cramér-Rao bound which is a lower bound to this standard deviation.

In general it is not easy to find the best estimator for a given purpose. However we are mostly interested in asymptotic properties of the estimator, *i.e.* when the sample size $N \to \infty$. In this case the task is simpler and the so-called *maximum-likelihood estimator* is usually both unbiased and efficient. The basic concept underlying this estimator is the *likelihood function* of $\lambda$ for a given sample defined by

$$L(\lambda|x_1, \ldots, x_N) = p(x_1|\lambda) \cdots p(x_N|\lambda)\,. \tag{6.4}$$

Intuitively it describes the likelihood that the parameter takes the value $\lambda$ if a given sample is observed. The hope is that the parameter that maximizes $L$ is also good estimate of $\lambda_0$. The maximum-likelihood estimator is thus defined by

$$\hat{\lambda}_{\mathrm{MLE}}(x_1, \ldots, x_N) = \arg\max_{\lambda \in \mathbb{R}^m} \left[L(\lambda|x_1, \ldots, x_N)\right]\,. \tag{6.5}$$

Note that there is in principle no guarantee that a single maximum exists in general, but we need not worry about it in the cases studied in this thesis. In practice it is easier to work with the *log-likelihood function*

$$\ell(\lambda|x_1, \ldots, x_N) = \sum_{i=1}^{N} \log p(x_i|\lambda)\,, \tag{6.6}$$

and we can equivalently maximize $\ell$ to find the maximum-likelihood estimate of $\lambda$.

For $N \to \infty$ we can replace the summation by an average over the probability distribution

$$\ell(\lambda) = N \int dx\, p(x|\lambda_0) \log p(x|\lambda)\,. \tag{6.7}$$

We can show that $\lambda = \lambda_0$ indeed maximizes $\ell(\lambda)$. The first derivatives vanish

$$\frac{\partial}{\partial \lambda_i}\ell(\lambda_0) = N \int dx\, p(x|\lambda_0) \left[\frac{\partial}{\partial \lambda_i} \log p(x|\lambda)\right]_{\lambda=\lambda_0} = N \left[\frac{\partial}{\partial \lambda_i} \int dx\, p(x|\lambda)\right]_{\lambda=\lambda_0} = 0\,, \tag{6.8}$$

and the Hessian

$$\frac{\partial}{\partial \lambda_i}\frac{\partial}{\partial \lambda_j}\ell(\lambda_0) = -N \int dx\, p(x|\lambda_0) \left[\frac{\partial}{\partial \lambda_i} \log p(x|\lambda)\right] \left[\frac{\partial}{\partial \lambda_j} \log p(x|\lambda)\right]_{\lambda=\lambda_0} \equiv -N F_{ij} \tag{6.9}$$

is negative, because the thereby defined $F_{ij}$ is an average of positive matrices (projectors). We henceforth assume the Hessian to be even negative definite (as is the case if all the components of $\lambda$ are independently relevant). Essentially we have proven that the maximum-likelihood estimator will yield the correct value $\lambda_0$ asymptotically provided that the likelihood function has an unique global maximum.

The distribution of $\hat{\lambda}_{\mathrm{MLE}}$ in the asymptotic limit is obtained by considering the normalized likelihood function $p_{\mathrm{MLE}}(\lambda) = L(\lambda)/C = \exp(\ell(\lambda))/C$, where $C = \int d\lambda\, L(\lambda)$.

Using the steepest-descent method we obtain

$$p_{\mathrm{MLE}}(\lambda) = \lim_{N\to\infty} \frac{1}{C} \exp\left( N \int dx\, p(x|\lambda_0) \log p(x|\lambda) \right)$$
$$= \frac{1}{\sqrt{(2\pi)^m N \det F}} \exp\left( -\frac{1}{2} (\lambda - \lambda_0)_i F^{-1}_{ij} (\lambda - \lambda_0)_j \right) . \tag{6.10}$$

The maximum-likelihood estimator is thus *asymptotically normal*, with standard deviations given by

$$\Delta\lambda_i = \sqrt{\frac{(F^{-1})_{ii}}{N}} . \tag{6.11}$$

This result is very useful because it gives the statistical uncertainty on the estimation of a parameter from a finite-size sample. The scaling $1/\sqrt{N}$ which appears here is ubiquitous when $N$ repetitions of *independent* experiments are run.

Remarkably it is possible to prove that the statistical uncertainty (6.11) is minimal [Helstrom76]. In other words no other unbiased estimator of $\lambda$ can do a better job than the maximum-likelihood estimator asymptotically. The general result is called the *Cramér-Rao bound* and states that any unbiased estimator $\hat{\lambda}$ has minimal standard deviation

$$\Delta\hat{\lambda} \geq \sqrt{\frac{(F^{-1})_{ii}}{N}} , \tag{6.12}$$

where $F_{ij}$ is the *Fisher information matrix* given by

$$F_{ij} = \int dx\, p(x|\lambda_0) \left[ \frac{\partial}{\partial\lambda_i} \log p(x|\lambda) \right] \left[ \frac{\partial}{\partial\lambda_j} \log p(x|\lambda) \right]_{\lambda=\lambda_0} . \tag{6.13}$$

The Fisher information already appeared in the Hessian of the log-likelihood function, see Eq. (6.9). Estimators that saturate the Cramér-Rao bound are called *efficient*. The maximum-likelihood estimator is thus asymptotically efficient.

### Trivial example

In order to illustrate the maximum-likelihood estimation procedure we consider a simple example. We consider the estimation of the average height $\mu$ of trees in a given forest. We assume that the height $h$ is Gaussian distributed

$$p(h|\mu) = \frac{1}{\sqrt{2\pi}\sigma} \exp(-(h-\mu)^2/2\sigma^2)$$

around the mean height $\mu$. We want to illustrate explictly how the maximum-likelihood procedure yields an estimation for $\mu$ from a set of observed tree heights $\{h_i\}$.

The log-likelihood of a sample of $N$ tree heights reads

$$\ell(\mu) = \sum_i^N \log p(h_i|\mu) = \sum_i^N -\frac{(h_i-\mu)^2}{2\sigma^2} - \log(\sqrt{2\pi}\sigma) ,$$

and its maximization yields the simple result $\hat{\mu}_{\mathrm{MLE}} = \frac{1}{N}\sum_i h_i$. The Fisher information is given by $F = \sigma^{-2}$ and the Cramér-Rao bound reads $\Delta\hat{\mu} \geq \sigma/\sqrt{N}$.

Through this example we learn two essential things. On the one hand, the maximum-likelihood estimation works as expected. On the other hand, the whole formalism is absolutely superfluous in these cases. This explains why these concepts from parameter estimation, which appear as absolutely fundamental to any interpretation of quantum measurements, are not part of the basic training of every physicist. Nevertheless a solid understanding of these concepts becomes mandatory for satisfactory treatments of many complex measurement scenarios.

### Noise

Up to now we took for granted that the probability distribution $p(x|\lambda)$ was exactly known. As a consequence the only source of uncertainty in the estimation of parameters was of statistical nature. By repeating the experiment many times it is possible to reduce the statistical uncertainty at will, and thus obtain measurements of any quantity to an arbitrary precision. In real experiments however, unwanted sources of disturbance modify the observed $p(x|\lambda)$ in an uncontrolled way. We investigate what are the effects of this noise on parameter estimation.

Let us take our example again to illustrate the concepts at hand. This time however the measurement process is plagued by two kind of uncertainties: a systematic error $d$ due to a miscalibration of the ruler used for measuring trees, and Gaussian fluctuations of amplitude $s$ due to the finite precision of the measurement process. To formalize these noises we introduce the noise kernel

$$\xi(h,h') = \frac{1}{\sqrt{2\pi}s} e^{-(h-(h'+d))^2/2s^2}\,, \tag{6.14}$$

which allows us to express the observed height distribution $p_{\text{obs}}(h)$ as a convolution of $\xi$ with the real height distribution $p_{\text{real}}(h) = \frac{1}{\sqrt{2\pi}\sigma}\exp(-(h-\mu)^2/2\sigma^2)$:

$$p_{\text{obs}}(h) = \int dh'\, \xi(h,h') p_{\text{real}}(h') = \frac{1}{\sqrt{2\pi(\sigma^2+s^2)}} \exp(-\frac{(h-(\mu+d))^2}{2(\sigma^2+s^2)})\,. \tag{6.15}$$

The problem of estimating $\mu$ from $p_{\text{obs}}$ rather than $p_{\text{real}}$ is formally the same. Indeed we can perform a maximum-likelihood estimation, and we find unsurprisingly $\hat{\mu}_{\text{MLE}} = \frac{1}{N}\sum_i h_i - d$ and $\Delta\hat{\mu}_{\text{MLE}} = \sqrt{(\sigma^2+s^2)/N}$. The problem is, of course, that $d$ and $s$ are unknown. In practice their values can merely be bound by some more general considerations; say the reliable manufacturer of the tree rulers provide $|d| < 1\text{cm}$. In that case, we must accept that the accuracy our final estimation of $\mu$ is ultimately limited by $\pm 1\text{cm}$.

Although this example is somewhat too simple we can still draw some useful observations. First, different noises have different impacts on the parameter estimation. Here the systematic error $d$ limits the accuracy of the measurement, while $s$ decreases its precision. In other words the Gaussian fluctuations $s$ increase the statistical uncertainty and we can counter it by performing more measurements, while $d$ sets an absolute limit. Second, the strategy of incorporating the noise sources prior to the parameter estimation process and dealing with them at the very end is a valid procedure. It allows us to precisely evaluate the effect of noise sources on the measurement.

## 6.2 Parameter estimation in weak measurements

### 6.2.1 Quantum limit

We are now ready to apply the formalism of parameter estimation to weak measurement problems. Our goal is to study how much information about the value of a small parameter $k$ is contained in a joint measurement of a "meter + system" pair due to an interaction of the form $\hat{U}(k) = \exp(ik\hat{A}\hat{q})$.

Let us start by computing the quantum Fisher information [Zhang13] $F_q$ contained in the joint state $|\Psi(k)\rangle = \hat{U}(k)\,|\psi_0\rangle\,|i\rangle$, where $|\psi_0\rangle$ is the initial state of the meter and $|i\rangle$ is the initial state of the system. We obtain

$$\begin{aligned} F_q &= 4\left(\frac{d\,\langle\Psi(k)|}{dk}\frac{d\,|\Psi(k)\rangle}{dk} - \left|\langle\Psi(k)|\,\frac{d\,|\Psi(k)\rangle}{dk}\right|^2\right) \\ &= 4\left[\langle\hat{q}^2\rangle_0\langle\hat{A}^2\rangle_i - \langle\hat{q}\rangle_0{}^2\langle\hat{A}\rangle_i{}^2\right] \equiv 4[\Delta(Aq)]^2\,. \end{aligned} \tag{6.16}$$

It is independent of the choice of any actual measurement performed on the system and the meter. The quantum Fisher information yields an absolute bound on the estimation of $k$ in the form of a quantum Cramér-Rao bound

$$\Delta k_{\text{est}} \geq \frac{1}{2\Delta(Aq)\sqrt{N}}\,, \tag{6.17}$$

where $N$ is the number of repetitions of the experiment. This bound depends on the initial states of $M$ and $S$, but is independent of any actual measurement performed on them. There is in principle no guarantee that there is a suitable choice of observables allows us to saturate this bound.

#### Weak measurements

We now choose observables for the meter and system with eigenstates $|m\rangle$ and $|s\rangle$ respectively. The result of a weak measurement is described by the joint probability distribution $p(m,s|k)$. Since the measurement is weak, it is natural to expand $p(m,s|k)$ in powers of $k$ around $p_0(m,s)$, where $p_0(m,s) = |\langle m|\psi_0\rangle|^2\,|\langle s|i\rangle|^2$ is the known initial probability distribution before the interaction. Namely, we write

$$p(m,s|k) = \left[1 + kf_1(m,s) + \frac{1}{2}k^2 f_2(m,s)\right] p_0(m,s) + O(k^3)\,, \tag{6.18}$$

where $f_j(m,s)$ is the contribution of order $j$ in $k$, and satisfies $\sum_s \int dm\; f_j(m,s)p_0(m,s) = 0$ to ensure proper normalization. The Fisher information is readily obtained

$$F = \sum_s \int dm\; f_1(m,s)^2 p_0(m,s) + O(k)\,. \tag{6.19}$$

The maximization of the log-likelihood of a set of outcomes $\{m_j, s_j\}$ leads to

$$0 = \frac{d}{dk}\ell(k) = \sum_{j=1}^{N}\frac{d}{dk}\log f(m_j,s_j,k) = \sum_{j=1}^{N} f_1(m_j,s_j) + k(f_2(m_j,s_j) - f_1(m_j,s_j)^2) + O(k^2)\,. \tag{6.20}$$

Solving the equation provides the maximum-likelihood estimate for $k$. We may further neglect the term containing $f_2$ in the asymptotic limit ($N \to \infty$), because then the sum over outcomes approximates well the average $\sum_s \int dm\ f_2(m,s)p(m,s|k) = O(k)$. Therefore we obtain the simple formula

$$k_{\text{est}} = \frac{\sum_{j=1}^{N} f_1(m_j, s_j)}{\sum_{j=1}^{N} f_1(m_j, s_j)^2}\,. \tag{6.21}$$

And the mean-square deviation of the estimate is provided by the Fisher information in the asymptotic limit

$$\Delta k_{\text{est}} = \frac{1}{\sqrt{N\langle f_1(m,s)^2\rangle_0}}\,. \tag{6.22}$$

We shall use these results in the next sections to compute the performance of the weak-value amplification schemes from a parameter estimation point of view.

### 6.2.2 Imaginary weak-value amplification

The probability distribution that characterizes an imaginary-weak-value measurement is given by the conditional probability

$$p(q|k,f) = \frac{p(q,f|k)}{\int dq\ p(q,f|k)} = [1 + 2k(q - \langle q\rangle_0)\,\mathrm{Im}\,A_w]\,p_0(q)\,, \tag{6.23}$$

at first order in $k$, and where we used $p(q,f;k) = \left|\langle f|\, e^{-ikq\hat{A}}\,|i\rangle\right|^2 p_0(q)$. We see that $f_1(q) = 2(q - \langle q\rangle_0)\,\mathrm{Im}\,A_w$, from which we can extract the maximum likelihood estimator (6.21)

$$k_{\text{est}} = \frac{\sum_{j=1}^{N}(q_j - \langle q\rangle_0)}{2\,\mathrm{Im}\,A_w \sum_{j=1}^{N}(q_j - \langle q\rangle_0)^2}\,. \tag{6.24}$$

The Fisher information for the imaginary-weak-value amplification scheme reads

$$F_{\text{iwva}} = 4(\Delta q)^2\,|\langle f|i\rangle|^2\,(\mathrm{Im}\,A_w)^2\,, \tag{6.25}$$

where we multiplied the expression (6.19) by $|\langle f|i\rangle|^2$ to take into account the post-selection process.

Since the weak-value is unbounded, we might worry that $F_{\text{iwva}}$ can be larger than $F_q$ (6.16) with a suitable choice of pre- and post-selection. This is not the case, for the product $|\langle f|i\rangle|^2\,(\mathrm{Im}\,A_w)^2$ is bounded

$$\begin{aligned}
|\langle f|i\rangle|^2\,(\mathrm{Im}\,A_w)^2 &\le \sum_s |\langle s|i\rangle|^2 \left[\mathrm{Im}\left(\frac{\langle s|\,\hat{A}\,|i\rangle}{\langle s|i\rangle}\right)\right]^2 \\
&= \sum_s |\langle s|i\rangle|^2 \left[\mathrm{Im}\left(\frac{\langle s|\,\hat{A} - \langle\hat{A}\rangle_i\,|i\rangle}{\langle s|i\rangle}\right)\right]^2 \\
&\le \sum_s \langle i|\,\hat{A} - \langle\hat{A}\rangle_i\,|s\rangle\,\langle s|\,\hat{A} - \langle\hat{A}\rangle_i\,|i\rangle \\
&= \langle i|\,(\hat{A} - \langle\hat{A}\rangle_i)^2\,|i\rangle = (\Delta A)^2\,,
\end{aligned} \tag{6.26}$$

which, together with the trivial inequality $\Delta A \Delta q \le \Delta(Aq)$, ensures that $F_{\text{iwva}} \le F_q$.

### 6.2.3 Joint weak measurements

We now investigate the case of a full joint weak measurement without post-selection. The main question is whether any information is gained by not restricting the scheme to a single system outcome $f$. The full joint probability distribution reads

$$p(q,s|k) = |\langle s|i\rangle|^2 \left[1 + 2kq \operatorname{Im} A_{w(i\to s)}\right] p_0(q)\,, \tag{6.27}$$

where $p_0(q)$ is the initial probability distribution of the meter and $s$ runs over a complete basis of the system. Using the formula (6.19 we obtain the Fisher information

$$F_{\text{jwm}} = 4\langle q^2\rangle_0 \sum_s |\langle s|i\rangle|^2 \left(\operatorname{Im} A_{w(i\to s)}\right)^2\,, \tag{6.28}$$

where $A_{w(i\to s)} = \langle s|\,\hat{A}\,|i\rangle \,/\, \langle s|i\rangle$. Comparing to $F_{\text{iwva}}$ (6.25) we observe that $F_{\text{jwm}}$ sums over all system states and thus may hold more information. However, it is often possible to concentrate almost all of the sum into a single term with $s = f$ [Hofmann11, Hofmann12].

There is a second, more interesting, difference: instead of a prefactor of $(\Delta q)^2$ in $F_{\text{iwva}}$, $F_{\text{jwm}}$ has a potentially much larger $\langle q^2\rangle_0$. As a consequence, a full joint measurement offers an advantage over post-selection schemes in the signal-to-noise ratio. This is a little acknowledged fact in the literature [Hofmann11, Hofmann12, Jordan13] which focused on centered meters for which $(\Delta q)^2 = \langle q^2\rangle_0$. This proves that there can be useful information in the usually discarded failed post-selection mode. An application of this observation is made in Sec. 6.2.5.

Because the amplification mechanism does not, in fact, hinge upon a choice of large weak values, some works [Knee13b, Ferrie14, Tanaka13] claimed that weak-value amplification is useless on the basis of a Fisher information analysis. However, there are essentially two cases for which post-selection can still be useful (see also [Jordan13]): first, for detection noise with long coherence times where the post-selection probability reduces the noise, see Sec. 5.3.2; second, when detector saturation is the bottleneck, post-selection allows one to concentrate the useful information in fewer detection events, see Sec. 5.3.3. Otherwise, the additional information contained in the failed post-selection modes can be fruitfully used to further reduce detection white noise and improve the statistical signal-to-noise ratio. We shall also see another use of the additional information to mitigate technical noise due to post-selection imperfections in Sec. 6.3.

### 6.2.4 Estimation in the presence of noise

Joint weak measurements also perform better in the presence of certain types of technical noise. To see this we first give the explicit estimator of $k$ as a function of the experimental outcomes

$$k_{\text{est}} = \frac{1}{NF_{\text{jwm}}} \sum_{j=1}^{N} 2q_j \operatorname{Im}\left(\frac{\langle s_j|\,\hat{A}\,|i\rangle}{\langle s_j|i\rangle}\right)\,. \tag{6.29}$$

We consider again a simple white detection-noise model $q_j \to q_j + \xi_j$ with $\langle \xi_i\rangle = 0$ and $\langle \xi_i\xi_j\rangle = \xi^2\delta_{ij}$ and compute the additional expected mean-square deviation $\delta k_{\text{est}}$ due to the noise terms. We find

$$\delta k_{\text{est, jwm}} = \frac{\xi}{2\sqrt{N}\langle q^2\rangle_0 \sqrt{\sum_s |\langle s|i\rangle|^2 \left(\operatorname{Im} A_{w(i\to s)}\right)^2}}\,. \tag{6.30}$$

This is to be compared to the deviation for the imaginary weak-value amplification scheme

$$\delta k_{\text{est, iwva}} = \frac{\xi}{2\sqrt{N}(\Delta q)^2 \, |\langle f|i\rangle| \, \text{Im}\, A_{w(i\to f)}} \,. \tag{6.31}$$

The ratio

$$\frac{\delta k_{\text{est, jwm}}}{\delta k_{\text{est, iwva}}} \lesssim \frac{(\Delta q)^2}{\langle q^2\rangle_0} \leq 1 \tag{6.32}$$

clearly demonstrate the superiority of the joint weak measurement scheme against the imaginary weak-value technique in the presence of detection white noise.

### 6.2.5 Reaching the Heisenberg limit using joint weak measurements

Recently, a proposal [Feizpour11] was made to amplify a single-photon nonlinearity using a real weak-value amplification scheme. In their idea, a single photon and a probe laser beam are coupled by the cross Kerr effect by traversing a suitable material; the evolution is described by the operator $U = e^{i\phi_0 \hat{n}_p \hat{n}}$, where $\phi_0$ is the strength of the effect to be measured, $\hat{n}_p$ is the number operator of the single photon, and $\hat{n}$ is the number operator of the laser beam. Before interacting, the single-photon is split into two paths, only one of which interacts with the beam. This controlled splitting corresponds to the pre-selection in the weak-value amplification scheme. The two arms then recombine and only one output port of the single-photon interferometer is observed (post-selection).

In their proposal, Feizpour *et al.* choose a particular pre- and post-selection in order to obtain a real weak-value. Whenever a single-photon is successfully post-selected they predict that the phase of the laser light will be altered by the interaction with the single-photon due to the cross Kerr effect with an amplified strength, "as if the single-photon behaves like 100 photons". The hope is that this enhancement is enough to bring this single-photon nonlinearity to a measurable level.

We now want to investigate what would happen with the same setup if we choose a joint weak measurement scheme instead. To make contact with our notations, we introduce a which-path operator $\sigma_z$ for the single photon. Then the measurement interaction has the form

$$U = e^{i\phi_0 \hat{n}(1+\sigma_z)/2} \,, \tag{6.33}$$

where $\hat{n}$, the number operator of the probe laser beam, acts as the "meter", and the which-path information takes the role of the "system".

The probe laser beam is prepared in a coherent state $|\alpha\rangle$. The number of photons $n$ it contains follows a Poisson distribution

$$p_0(n) = \frac{e^{-|\alpha|^2}}{n!}\alpha^n \,, \tag{6.34}$$

with an average photon number $\bar{n} = |\alpha|^2$. After interaction with the single-photon the measured distribution becomes

$$p(n,s) = p_0(n)\left[1 + n\phi_0 \, \text{Im}\,(\sigma_z)_{w(i\to s)}\right] \tag{6.35}$$

at first order in the coupling, and where we used $\text{Im}(1+\sigma_z)_{w(i\to s)} = \text{Im}(\sigma_z)_{w(i\to s)}$ . The Fisher information contained in the full distribution can be maximized by choosing

final states $s$ to obtain purely imaginary weak values. In that case, we obtain the Fisher information

$$F = 4\langle n^2 \rangle_0 = 4\bar{n}^2 + 4\bar{n}\,. \tag{6.36}$$

The signal-to-noise ratio thus scales as the Heisenberg limit, *i.e.* proportionally to the number of photons $\bar{n}$, whereas the original proposition [Feizpour11] that uses weak-value amplification is bound by the SQL and displays a scaling proportional to $\sqrt{\bar{n}}$. This is a clear example where the information contained in the failed post-selection mode can be used to significantly enhance the signal-to-noise ratio.

Superficially, it appears that we can beat the SQL using only classical resources: the incoming laser beam is just a coherent state well described classically. However, this is not quite the case. The interaction (6.33) entangles the beam with the single photon. In fact, for purely imaginary weak values the entanglement between the single photon output states and the beam is "maximal". This entanglement is the reason why we reach the Heisenberg limit in that case.

An independent work [Zhang13] also studied this idea and found results consistent with ours. Theoretically, this joint weak measurement scheme would thus benefit from photon shot noise, whereas it is detrimental to the phase estimation necessary in the real-weak-value amplification scheme. Whether this translates into a practical advantage as well depends on the characteristics of detectors, and would be the subject of further investigations.

## 6.3 Measuring ultrasmall time delays of light using joint weak measurements

In this section, we propose a scheme to measure very small time delays, or longitudinal phase shifts of light. The idea is to use weak measurements away from the weak-value amplification regime and to exploit the full information contained in the correlations induced by the time delay between the frequency and the polarization of photons going through the interferometer. A joint estimation is performed on the time-delay of interest and on the post-selection parameter. This mitigates strongly the effect of post-selection noise, and effectively removes it as an ultimate bottleneck of precision; on the contrary to the imaginary weak-value amplification based scheme proposed in Ref. [Brunner10] that inspired the present analysis.

### 6.3.1 Time-delay measurements

Following Ref. [Brunner10], we consider a Mach-Zehnder interferometer for laser light, see Fig. 6.1a. Encoding the which-path information in a two-level system allows us to write the effect of the time delay as

$$U = e^{i\tau\hat{\sigma}_y \hat{H}/2}\,, \tag{6.37}$$

where $\hat{\sigma}_y$ acts on the which-path space, and $\hat{H}$ is the Hamiltonian of the laser light. In the weak-value amplification language, the time delay now takes the role of the interaction parameter, and the photon frequencies (which are contained in $\hat{H}$) the role of the pointer variable $x$. The incoming light is evenly split into the two arms with opposite circular polarizations by a polarizing beam splitter. The two arms then recombine at

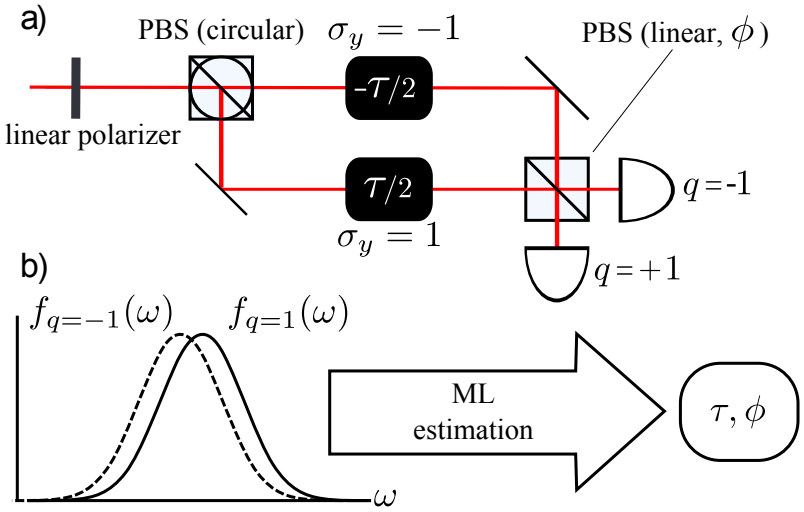


Figure 6.1: (a) Mach-Zehnder interferometer for laser light with a time-delay asymmetry $\tau$. The incoming beam is linearly polarized and then evenly split by a polarizing beam splitter (PBS) into the two arms with opposite circular polarizations, $\sigma_y = \pm 1$. The beams are recombined at a second PBS with linearly polarized outputs. The direction of the linear polarization is described by the azimuthal angle $\phi$ on the Poincaré sphere. Two spectrometers labeled by $q = \pm 1$ measure the spectrum of the outgoing light. (b) Graphical representation of the estimation process. The values of $\tau$ and $\phi$ are extracted from the spectra measured by the two detectors by a maximum-likelihood (ML) estimation technique as described in the text.

another polarizing beam splitter with linearly polarized outputs. The direction of the linear polarization is described by the azimuthal angle $\phi$ on the Poincaré sphere. The two output ports $q = \pm 1$ are monitored by spectrometers. In the weak-value language, the pre-selected polarization state is $|i\rangle = (|-\rangle + |+\rangle)/\sqrt{2}$ and the two post-selected states at detector $q$ are $|f_q\rangle = (|-\rangle + qe^{i\phi}|+\rangle)/\sqrt{2}$.

A laser pulse with normalized spectrum $p_0(\omega)$, which can be interpreted as a probability density, is sent through the interferometer. The probability density of outcomes is then given by

$$p_q(\omega;\tau,\phi) = \frac{1}{2}p_0(\omega)[1 + q\exp(-\epsilon^2/2)\cos(\phi - \omega\tau)]\,, \tag{6.38}$$

where we have introduced Gaussian fluctuations of amplitude $\epsilon$ of the alignment parameter $\phi$, *i.e.*, convoluted the bare probability density with a fluctuation kernel

$$\xi(\phi,\phi') = \frac{1}{\sqrt{2\pi}\epsilon}\exp\left(-\frac{(\phi-\phi')^2}{2\epsilon^2}\right) \tag{6.39}$$

that describes fluctuations around the average alignment $\phi$. Note that only the fluctuations with a correlation time smaller than the measurement duration are included in $\epsilon$. Fluctuations with a longer correlation time will modify the effective value of $\phi$. From now on we make the realistic assumption $\epsilon \ll 1$. It can be shown that fluctuations of the alignment of the circular polarizing beam splitter and of the linear polarizer can also be encompassed in $\epsilon$.

**Joint estimation**

Our goal is to find an estimate of the values of the parameters $\tau, \phi$ from outcomes of an experiment following the probability distribution (6.38). Although $\phi$ is in principle controlled experimentally, its estimation permits to remove possible systematic errors. The quantity produced by the experiment is a set of observed frequencies $f_q(\omega)$, which, in principle, converge to $p_q(\omega;\tau,\phi)$ as the number $N$ of measured photons is increased.

We use the maximum likelihood procedure, see Sec. 6.1, to provide unbiased estimates of the values of the parameters, see Fig. 6.1b. This is achieved by maximizing the log-likelihood function $l(\tau,\phi)$ defined as

$$l(\tau,\phi) = \sum_{q=\pm1} \int d\omega \; f_q(\omega) \log p_q(\omega;\tau,\phi) \,. \tag{6.40}$$

Maximizing the log-likelihood yields two equations which have to be solved numerically in the general case. However, for the special case of almost equal intensities at the two detectors, $|\phi - \omega\tau - \frac{\pi}{2}| \ll 1$, analytical expressions can be derived

$$\phi = \frac{\pi}{2} - \exp(\epsilon^2/2) \sum_q q P_q \,, \tag{6.41}$$

$$\tau = \frac{1}{4\Delta\omega} \exp(\epsilon^2/2) \left( \frac{1}{\Delta\omega} \sum_q q P_q \langle\omega\rangle_q - \sum_q q P_q \right) , \tag{6.42}$$

where $P_q$ is the integrated fraction of outcomes in detector $q$, and $\langle\cdot\rangle_q$ denotes the average value in detector $q$. The frequency spread $\Delta\omega$ of the initial distribution is given by $(\Delta\omega)^2 = \sum_q P_q \langle\omega^2\rangle_q - \left(\sum_q P_q \langle\omega\rangle_q\right)^2$. The estimates (6.41,6.42) depend on measurement results and on one unknown amplitude $\epsilon$ that characterizes alignment fluctuations. Remarkably, $\exp(\epsilon^2/2)$ only appears as an overall multiplicative factor. Thus, the ultimate error $\Delta\tau_{\rm ult}$ on the estimation of $\tau$ by assuming $\epsilon = 0$ (since its value is unknown, yet realistically $\epsilon \ll 1$) scales with $\tau$, *i.e.* only a relative error occurs that does not limit the smallest $\tau$ that can be measured. Equation (6.42) is one of the main results of this section.

Aside from the errors due to technical noise, statistical uncertainties also contribute to the estimation error. For a finite number $N$ of detected photons, the statistical errors are provided by the Cramér-Rao bound: $\Delta\tau_{\rm stat} \geq \sqrt{(\mathcal{I}^{-1})_{\tau\tau}/N}$, and $\Delta\phi_{\rm stat} \geq \sqrt{(\mathcal{I}^{-1})_{\phi\phi}/N}$, where $\mathcal{I}$ is the Fisher information matrix given by

$$\mathcal{I}_{yz} = \sum_{q=\pm1} \int dx \; p_q(x;\tau,\phi) \left(\partial_y \log p_q\right) \left(\partial_z \log p_q\right) \,. \tag{6.43}$$

Asymptotically, *i.e.*, for large $N$, the Cramér-Rao bounds are saturated by the maximum-likelihood procedure. In the case of almost equal intensities at the two detectors we obtain

$$\Delta\tau_{\rm stat} \geq \frac{\exp(\epsilon^2/2)}{4\Delta\omega\sqrt{N}} \,, \tag{6.44}$$

which shows that the fluctuations of $\phi$ do not increase significantly statistical noise. On the contrary to single parameter estimation, the denominator contains only $\Delta\omega$ instead

of the better $\langle\omega^2\rangle_0$. The reason is that estimating $\phi$ increases the statistical error on the estimation on $\tau$ from the same data. However, the scaling $1/\Delta\omega$ is the same as in imaginary weak-value amplification schemes. Moreover, $\Delta\omega$ and $\langle\omega^2\rangle_0$ is of the same order of magnitude for ultrashort laser pulses.

The number of detected photons $N$ required to obtain a good estimate of $\tau$ is of the order $10/(\Delta\omega\tau)^2$. Estimating a time delay of the order of 1 attosecond with ultrashort laser pulses with $\Delta\omega \approx 10^{15}$Hz would require detecting $10^7$ photons. A typical pulse contains typically $10^{13}$ photons which would be enough to measure time delays of the order of 1 zeptosecond corresponding to a displacement of 100fm.

### 6.3.2 Split detectors

We would now like to apply this result to an actual detector with a finite resolution. This will in particular shed light on the roles played by the resolution and readout noise of the detector. In principle, the results of the previous section could require measuring the full distribution of $\omega$ without any readout noise. To show that this is not the case we consider "split" detectors which can only discriminate two spectral regions $\omega > \omega_0$, leading to a measurement result $r = +1$, and $\omega < \omega_0$, leading to $r = -1$. We also add readout noise from the outset. we shall see that our conclusion from Eq. (6.42) (*viz.* that there is no absolute lower limit on the smallest value of $\tau$ that can be measured) survives even in this extreme case.

To make up for losing the detector resolution some *a priori* knowledge of the initial frequency distribution $p_0(\omega)$ is required. For analytical calculations we shall assume an initial Gaussian distribution, but the results will depend only quantitatively on the shape. In practice the distribution should be measured and the calculations done numerically. We thus assume $p_0(\omega) \approx e^{-(\omega-\omega_0)^2/2(\Delta\omega)^2}/\sqrt{2\pi}\Delta\omega$. The probabilities of the two possible outcomes $r = \pm 1$ at the two detectors $q = \pm 1$ at second order in the small quantity $\Delta\omega\tau$ read

$$\begin{aligned} p_{rq} = \frac{1}{4}[1 + q\exp(-\epsilon^2/2)(1 - \frac{1}{2}(\Delta\omega\tau)^2)\cos\phi] \\ + rq\exp(-\epsilon^2/2)\frac{\Delta\omega\tau}{2\sqrt{2\pi(1+(\Omega/\Delta\omega)^2)}}\sin\phi\,, \end{aligned} \tag{6.45}$$

where we allowed for a frequency detection uncertainty of order $\Omega$ modeled as Gaussian white noise.

Denoting the measured probabilities by $f_{rq}$, the maximum likelihood estimation can be analytically carried out in the regime $|\sin\phi| \gg \Delta\omega\tau$, and yields $\cos\phi = \exp(\epsilon^2/2)(P_+ - P_-)$ in terms of the integrated fraction of outcomes $P_q = \sum_r f_{rq}$, and

$$\tau = \frac{\sqrt{2\pi(1+(\Omega/\Delta\omega)^2)}}{8\Delta\omega\sqrt{\exp(-\epsilon^2) - (P_+ - P_-)^2}} \sum_{r,q} \frac{rqf_{rq}}{1 + q(P_+ - P_-)}\,. \tag{6.46}$$

The first terms in the expansion of $\tau$ in the fluctuations $\epsilon$ and detection noise $\Omega$ can now be calculated, and we finally obtain

$$\tau = \tau_0\left[1 + \frac{1}{2}\left(\frac{\epsilon}{\sin\phi}\right)^2 + \frac{1}{2}\left(\frac{\Omega}{\Delta\omega}\right)^2\right], \tag{6.47}$$

where $\tau_0$ is the estimated value of $\tau$ in the absence of noise, see Eq. (6.46) with $\epsilon$ and $\Omega$ set to zero. Again the noise does not set an absolute limit on the precision of the estimation of $\tau$ but only a relative precision. The frequency spread $\Delta\omega$ reduces the effect of readout noise. Moreover we observe that in order to minimize the effect of fluctuations of $\phi$, we have to work in the regime $\sin\phi \approx 1$ and not in the weak-value amplification regime of $\sin\phi \approx 0$ where the effect of fluctuations increased.

The statistical uncertainty is given by the Fisher information matrix, which is diagonal in this case, through the Cramér-Rao bound

$$\Delta\tau_{\text{stat}} \geq \frac{\sqrt{2\pi}}{4\Delta\omega\sqrt{N}} \left[1 + \frac{1}{2}\left(\frac{\epsilon}{\sin\phi}\right)^2 + \frac{1}{2}\left(\frac{\Omega}{\Delta\omega}\right)^2\right] . \tag{6.48}$$

Hence the considered fluctuations do not jeopardize the estimation of $\tau$ away from the weak-value amplification regime. We also note that using split detectors leads to a modest increase of statistical noise by a factor $\sqrt{2\pi}$ with respect to Eq. (6.44). Equations (6.47,6.48) demonstrate that even for low-resolution detectors our scheme is robust against readout noise and alignment errors.

### 6.3.3 Comparison to existing schemes

Standard interferometry compares two probabilities given by the sine and cosine of the total phase shift given by the combination $\phi - \omega\tau$. This leads to two difficulties: first, to estimate $\tau$ precisely, the laser frequency $\omega$ has to be highly stabilized. Secondly, the alignment $\phi$ cannot be separated from the effect of $\tau$, *i.e.*, alignment errors are a limiting factor to the precision achievable having complete statistical information. This ultimate precision, which cannot be increased by acquiring more measured data, is given by $\Delta\tau_{\text{ult}} = \epsilon/\omega$. In the procedure proposed by Brunner and Simon [Brunner10] that uses the imaginary part of the weak value, the first issue is solved since a large frequency spread $\Delta\omega$ is advantageous for the precise evaluation of $\tau$, which is also true in our scheme. However, the second issue is only partially addressed in [Brunner10]: alignments errors are still a limiting factor, $\Delta\tau_{\text{ult}} = C\epsilon$, where the proportionality constant $C \approx 10^{-18}$ s is three orders of magnitude smaller than for standard interferometry.

In contrast to that, a major advantage of our scheme is to remove systematic errors as well as fluctuations of the alignment as a limiting factor to the ultimate precision of the time-delay measurement. Alignment fluctuations lead to a relative error $\Delta\tau_{\text{ult}} = \epsilon^2\tau/2$ on the estimation of $\tau$, see the discussion after Eq. (6.42) and the illustration in Fig. 6.2. This is made possible by working away from the weak-value amplification regime and using all the information contained in the correlations between frequency and polarization of the photons to perform a simultaneous estimation of $\phi$ and $\tau$.

Finally, we would like to mention that if the detector can only measure events at a small rate due to detector saturation, small post-selection probabilities as realized in weak-value amplification schemes permit to effectively increase the rate of measurements [Starling09]. This allows to obtain better statistics, however, if the measurement is limited not by statistics but for other reasons, our method appears preferable.

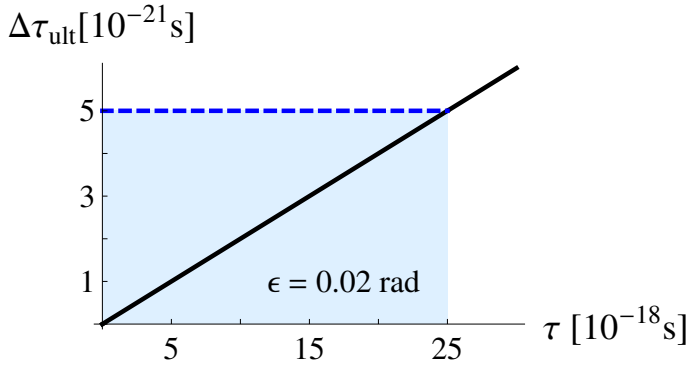


Figure 6.2: Ultimate precision limit $\Delta\tau_{\rm ult}$ on the estimation of the physical time delay $\tau$ as a function of $\tau$, in the presence of fluctuations of the alignment $\phi$, see Eq. (6.39). We assume $\epsilon = 0.02$ rad for the plot. The dashed line shows the constant (zeroth-order) contribution of fluctuations to $\Delta\tau_{\rm ult} = C\epsilon$ for weak-value amplification, here we assume $C \approx 0.25 \times 10^{-18}$ s like in [Brunner10]. The solid line is the result of our scheme, $\Delta\tau_{\rm ult} = \epsilon^2\tau/2$. For $\tau < 2C/\epsilon$ (shaded area), our scheme outperforms weak-value amplification .

## 6.4 Conclusion

To summarize, we have investigated the potential advantages of a natural extension to the imaginary weak-value amplification scheme. We have seen that the additional information provided by the full correlations between the system and meter degree of freedom can be used to great effects.

First, the signal-to-noise ratio can be dramatically enhanced by measuring the failed post-selection modes, see Eqs. (6.28.6.32). A potential application of this observation to reach the Heisenberg limit was investigated in Sec. 6.2.5.

Second, we have proposed a technique that could be useful to determine very small time delays, or longitudinal phase shifts, due to its robustness with respect to various noise sources. The time delay induces correlations between frequency and polarization of photons going through the interferometer, and our scheme exploits the full information contained in these correlations. The key idea is to perform a joint estimation of the time delay and of a noise parameter to mitigate its effects.

This procedure is not limited to time-delay measurements and could be used for other precision measurements. For example, it is readily applicable to measurements of ultra-small beam deflections by slightly modifying the protocol of Dixon *et al.* [Dixon09]. In a broader setting, the idea of carrying out a full joint measurement of two weakly entangled degrees of freedom could be relevant in many domains such as charge sensing in solid state physics [Zilberberg11], precision metrology, and gravitational wave detection.

# Chapter 7

# Conclusion

We start with a brief summary of the main results obtained in this thesis. In Chapter 3, we discussed the effect of spin axis symmetry breaking on the helical edge states of the quantum spin Hall effect. This led to consider generic helical liquids that are characterized by a spin texture [Schmidt12]. We saw how the spin texture can drastically affect transport properties in the presence of quantum point contacts. We gave a method to measure the spin texture using the width of Fabry-Pérot resonances. Finally, we saw how the localization length of the edge states in a narrow strip sample with disorder depends strongly on the spin texture. In Chapter 4, we proposed a Hanbury Brown-Twiss interferometric scheme that can be used to confirm the Majorana fermion nature of the edge states in transport experiments. We found three signatures of Majorana fermions. First, an exactly vanishing conductance together with an enhanced quantized shot noise at zero bias in the outgoing leads. Second, the robust absence of partition noise in the Hanbury Brown-Twiss interferometer with a quantum point contact. We argued that this is connected to the exact charge neutrality of the carriers; in other words, of their Majorana nature. Finally we saw that the full counting statistics leads to an interpretation of the charge transfer processes in terms of two half-fermion processes at zero bias. In Chapter 6, we gave a generalization to the weak-value amplification method that exploits the correlations induces by weak measurements to their full extent. The additional information was shown to improve the signal-to-noise ratio and could be used to reach the Heisenberg limit. We proposed another use of this additional information in the context of ultrasmall time-delay measurement; the idea is to perform a joint estimation of the main noise source and the parameter of interest. This was shown to outperform the bare weak-value amplification scheme in realistic scenarios.

We can think of several extensions to our work. First, the spin-texture dependance of transport in generic helical liquids coupled by point contacts could also find practical applications. For instance, by applying transverse electric fields it is possible to modify the local spin texture of the edge states via the induced Rashba spin-orbit coupling. In principle this could provide a way to tune the conductance of these systems by electrical means. For Majorana interferometry, the obvious follow-up to our work is to find the reach of our full counting statistics result. Namely, is the interpretation of electron/hole transfer processes as two independent half-charge transfers a deep property of Majorana fermions, or is it just by chance that this decomposition happens in our setup? A first step to go forward would be to investigate full counting statistics of other setups where

electrical transport is mediated by Majorana fermions, and see if there is an analogue to our result.

All of the weak-value amplification experiments thus far were carried out in optics. However, the applicability of the scheme is not in principle limited to these systems; it would be interesting to find applications to other fields of physics. One of the major difficulties to implement weak-value-type schemes using electrons in condensed matter is the need to couple two measurable degrees of freedom of the particle. For photons, we have plenty of choices: the polarization, transverse position, frequency, and which-path variable. For electrons, a theoretical proof of principle was given in Ref. [Zilberberg11], in which they use the weak-value amplification scheme to make sensitive measurements of charge. The idea is to use an Aharonov-Bohm ring interferometer for electrons in the presence of a magnetic field. The presence of a small electric charge $q$ in proximity to one of the arms changes the effective arm length due to electrostatic effects. The net effect is a weak coupling between the which-path degree of freedom and spin of the electrons proportional to $q$. Finally, the spin of the electrons is pre- and post-selected by means of spin valves. The scheme is very nice in principle, but it raises two big practical problems: first, the necessary stringent post-selection for amplification reduces the signal; in optics it is often an advantage, but reducing an already small current in mesoscopic physics is detrimental to its measurement. Second, the need for extrinsic spin valves complicates experimental realizations. A broad direction to adress these issues would be to combine the ideas of the first part and second part of this thesis. Notably, the intrinsic spin-filtering of the edge states of quantum spin Hall insulators combined with a joint weak-measurement-based scheme remove the need of extrinsic spin-valves and stringent post-selection issues.

In a very recent report [Salazar-Serrano14], the authors present an experimental realization of the Brunner and Simon [Brunner10] scheme using a Michelson-Morley interferometer. They demonstrate the measurement of a time-delay of the order of 10 attoseconds using a femtosecond laser source but with otherwise only linear optical elements. Significantly, they found a better sensitivity when working away from the high-loss regime, nearly orthognal pre- and post-selection, rather than in the large weak-value limit ordinary considered crucial for weak-value amplification. In this context, we think that a our joint weak measurement scheme is relevant and could lead to further improvements.

# Bibliography


[Aharonov59] Y. Aharonov and D. Bohm, *Significance of Electromagnetic Potentials in the Quantum Theory*. Phys. Rev. **115**, 485 (1959).

[Aharonov88] Y. Aharonov, D. Z. Albert, and L. Vaidman, *How the result of a measurement of a component of the spin of a spin- 1/2 particle can turn out to be 100*. Phys. Rev. Lett. **60**, 1351 (1988).

[Akhmerov09] A. Akhmerov, J. Nilsson, and C. Beenakker, *Electrically detected interferometry of Majorana fermions in a topological insulator*. Phys. Rev. Lett. **102**, 216404 (2009).

[Alicea10] J. Alicea, Y. Oreg, G. Refael, F. von Oppen, and M. P. A. Fisher, *Non-Abelian statistics and topological quantum information processing in 1D wire networks*. Nature Physics **7**, 412 (2010).

[Alicea12] J. Alicea, *New directions in the pursuit of Majorana fermions in solid state systems*. Reports on Progress in Physics **75**, 076501 (2012).

[Altland97] A. Altland and M. R. Zirnbauer, *Novel Symmetry Classes in Mesoscopic Normal-Superconducting Hybrid Structures*. Phys. Rev. B **55**, 1142 (1997).

[Anderson80] P. W. Anderson, D. J. Thouless, E. Abrahams, and D. S. Fisher, *New method for a scaling theory of localization*. Phys. Rev. B **22**, 3519 (1980).

[Avron83] J. E. Avron, R. Seiler, and B. Simon, *Homotopy and Quantization in Condensed Matter Physics*. Phys. Rev. Lett. **51**, 51 (1983).

[Bardarson13] J. H. Bardarson and J. E. Moore, *Quantum interference and Aharonov-Bohm oscillations in topological insulators*. Reports on Progress in Physics **76**, 056501 (2013).

[Bednorz10] A. Bednorz and W. Belzig, *Quasiprobabilistic Interpretation of Weak Measurements in Mesoscopic Junctions*. Phys. Rev. Lett. **105**, 106803 (2010).

[Beenakker13] C. W. J. Beenakker, *Search for Majorana Fermions in Superconductors*. Annu. Rev. Con. Mat. Phys. **4**, 113 (2013).

[Bernevig06] B. A. Bernevig, T. L. Hughes, and S.-C. Zhang, *Quantum Spin Hall Effect and Topological Phase Transition in HgTe Quantum Wells*. Science **314**, 1757 (2006).

[Börlin02] J. Börlin, W. Belzig, and C. Bruder, *Full Counting Statistics of a Superconducting Beam Splitter*. Phys. Rev. Lett. **88**, 197001 (2002).

[Bose11] S. Bose and P. Sodano, *Nonlocal Hanbury-Brown-Twiss interferometry and entanglement generation from Majorana bound states*. New Journal of Physics **13**, 085002 (2011).

[Brunner10] N. Brunner and C. Simon, *Measuring Small Longitudinal Phase Shifts: Weak Measurements or Standard Interferometry?* Phys. Rev. Lett. **105**, 010405 (2010).

[Bruus04] H. Bruus and K. Flensberg, *Many-Body Quantum Theory in Condensed Matter Physics*. Oxford University Press (2004).

[Budich13] J. C. Budich and B. Trauzettel, *From the adiabatic theorem of quantum mechanics to topological states of matter*. physica status solidi (RRL) **7**, 109 (2013).

[Büttiker88] M. Büttiker, *Absence of backscattering in the quantum Hall effect in multiprobe conductors*. Phys. Rev. B **38**, 9375 (1988).

[Büttiker92] M. Büttiker, *Scattering theory of current and intensity noise correlations in conductors and wave guides*. Phys. Rev. B **46**, 12485 (1992).

[Chang13] C.-Z. Chang, J. Zhang, X. Feng, J. Shen, Z. Zhang, M. Guo, K. Li, Y. Ou, P. Wei, L.-L. Wang, Z.-Q. Ji, Y. Feng, S. Ji, X. Chen, J. Jia, X. Dai, Z. Fang, S.-C. Zhang, K. He, Y. Wang, L. Lu, X.-C. Ma, and Q.-K. Xue, *Experimental Observation of the Quantum Anomalous Hall Effect in a Magnetic Topological Insulator*. Science **340**, 167 (2013).

[Cheng10] P. Cheng, C. Song, T. Zhang, Y. Zhang, Y. Wang, J.-F. Jia, J. Wang, Y. Wang, B.-F. Zhu, X. Chen, X. Ma, K. He, L. Wang, X. Dai, Z. Fang, X. Xie, X.-L. Qi, C.-X. Liu, S.-C. Zhang, and Q.-K. Xue, *Landau Quantization of Topological Surface States in $Bi_2Se_3$*. Phys. Rev. Lett. **105**, 076801 (2010).

[Chung11] S. B. Chung, X.-L. Qi, J. Maciejko, and S.-C. Zhang, *Conductance and noise signatures of Majorana backscattering*. Phys. Rev. B **83**, 100512 (2011).

[Das12] A. Das, Y. Ronen, Y. Most, Y. Oreg, M. Heiblum, and H. Shtrikman, *Zero-bias peaks and splitting in an Al-InAs nanowire topological superconductor as a signature of Majorana fermions*. Nature Physics **8**, 887 (2012).

[Delplace12] P. Delplace, J. Li, and M. Büttiker, *Magnetic-Field-Induced Localization in 2D Topological Insulators*. Phys. Rev. Lett. **109**, 246803 (2012).

[Deng12] M. T. Deng, C. L. Yu, G. Y. Huang, M. Larsson, P. Caroff, and H. Q. Xu, *Anomalous Zero-Bias Conductance Peak in a Nb-InSb Nanowire-Nb Hybrid Device*. Nano Letters **12**, 6414 (2012).

[Di Lorenzo12] A. Di Lorenzo, *Full counting statistics of weak-value measurement*. Phys. Rev. A **85**, 032106 (2012).

[Dixon09] P. B. Dixon, D. J. Starling, A. N. Jordan, and J. C. Howell, *Ultrasensitive Beam Deflection Measurement via Interferometric Weak Value Amplification*. Phys. Rev. Lett. **102**, 173601 (2009).

[Dolcetto12] G. Dolcetto, S. Barbarino, D. Ferraro, N. Magnoli, and M. Sassetti, *Tunneling between helical edge states through extended contacts*. Phys. Rev. B **85**, 195138 (2012).

[Dolcini11] F. Dolcini, *Full electrical control of charge and spin conductance through interferometry of edge states in topological insulators*. Phys. Rev. B **83**, 165304 (2011).

[Dyakonov71] M. Dyakonov and V. Perel, *Current-induced spin orientation of electrons in semiconductors*. Physics Letters A **35**, 459 (1971).

[Edge13] J. M. Edge, J. Li, P. Delplace, and M. Büttiker, *$Z_2$ Peak of Noise Correlations in a Quantum Spin Hall Insulator*. Phys. Rev. Lett. **110**, 246601 (2013).

[Feizpour11] A. Feizpour, X. Xing, and A. M. Steinberg, *Amplifying Single-Photon Nonlinearity Using Weak Measurements*. Phys. Rev. Lett. **107**, 133603 (2011).

[Ferrie14] C. Ferrie and J. Combes, *Weak Value Amplification is Suboptimal for Estimation and Detection*. Phys. Rev. Lett. **112**, 040406 (2014).

[Finck12] A. D. K. Finck, D. J. V. Harlingen, P. K. Mohseni, K. Jung, and X. Li, *Anomalous modulation of a zero bias peak in a hybrid nanowire-superconductor device*. Phys. Rev. Lett. **110**, 126406 (2012).

[Fu07] L. Fu, C. Kane, and E. Mele, *Topological insulators in three dimensions*. Phys. Rev. Lett. **98**, 106803 (2007).

[Fu08] L. Fu and C. Kane, *Superconducting proximity effect and Majorana fermions at the surface of a topological insulator*. Phys. Rev. Lett. **100**, 96407 (2008).

[Fu09a] L. Fu and C. Kane, *Josephson current and noise at a superconductor/quantum-spin-Hall-insulator/superconductor junction*. Physical Review B **79**, 161408 (2009).

[Fu09b] L. Fu and C. Kane, *Probing neutral Majorana fermion edge modes with charge transport*. Phys. Rev. Lett. **102**, 216403 (2009).

[Geszti10] T. Geszti, *Postselected weak measurement beyond the weak value*. Phys. Rev. A **81**, 044102 (2010).

[Gorodetski12] Y. Gorodetski, K. Y. Bliokh, B. Stein, C. Genet, N. Shitrit, V. Kleiner, E. Hasman, and T. W. Ebbesen, *Weak Measurements of Light Chirality with a Plasmonic Slit*. Phys. Rev. Lett. **109**, 013901 (2012).

[Grosfeld10] E. Grosfeld and A. Stern, *Observing Majorana bound states of Josephson vortices in topological superconductors*. PNAS **108**, 11810 (2010).

[Haldane88] F. D. M. Haldane, *Model for a Quantum Hall Effect without Landau Levels: Condensed-Matter Realization of the "Parity Anomaly"*. Phys. Rev. Lett. **61**, 2015 (1988).

[Halperin82] B. I. Halperin, *Quantized Hall conductance, current-carrying edge states, and the existence of extended states in a two-dimensional disordered potential*. Phys. Rev. B **25**, 2185 (1982).

[Hanaguri10] T. Hanaguri, K. Igarashi, M. Kawamura, H. Takagi, and T. Sasagawa, *Momentum-resolved Landau-level spectroscopy of Dirac surface state in $Bi_2Se_3$*. Phys. Rev. B **82**, 081305 (2010).

[Hasan10] M. Z. Hasan and C. L. Kane, *Colloquium : Topological insulators*. Rev. Mod. Phys. **82**, 3045 (2010).

[Helstrom76] C. W. Helstrom *et al.*, *Quantum detection and estimation theory*, volume 84. Academic press New York (1976).

[Hofmann11] H. F. Hofmann, *Uncertainty limits for quantum metrology obtained from the statistics of weak measurements*. Phys. Rev. A **83**, 022106 (2011).

[Hofmann12] H. F. Hofmann, M. E. Goggin, M. P. Almeida, and M. Barbieri, *Estimation of a quantum interaction parameter using weak measurements: Theory and experiment*. Phys. Rev. A **86**, 040102 (2012).

[Hogan11] J. M. Hogan, J. Hammer, S.-W. Chiow, S. Dickerson, D. M. S. Johnson, T. Kovachy, A. Sugarbaker, and M. A. Kasevich, *Precision angle sensor using an optical lever inside a Sagnac interferometer*. Opt. Lett. **36**, 1698 (2011).

[Hosten08] O. Hosten and P. Kwiat, *Observation of the Spin Hall Effect of Light via Weak Measurements*. Science **319**, 787 (2008).

[Hou09] C.-Y. Hou, E.-A. Kim, and C. Chamon, *Corner Junction as a Probe of Helical Edge States*. Phys. Rev. Lett. **102**, 076602 (2009).

[Hu12] J. Hu, J. Alicea, R. Wu, and M. Franz, *Giant topological insulator gap in graphene with 5d adatoms*. Phys. Rev. Lett. **109**, 266801 (2012).

[Ivanov01] D. A. Ivanov, *Non-Abelian Statistics of Half-Quantum Vortices in p-Wave Superconductors*. Phys. Rev. Lett. **86**, 268 (2001).

[Jayaswal14] G. Jayaswal, G. Mistura, and M. Merano, *Observation of the Imbert-Fedorov effect via weak value amplification*. arXiv:1401.0450 (2014).

[Jordan13] A. N. Jordan, J. Martínez-Rincón, and J. C. Howell, *Technical advantages for weak value amplification: When less is more*. arXiv:1309.5011 (2013).

[Kane05a] C. L. Kane and E. J. Mele, *Quantum Spin Hall Effect in Graphene*. Phys. Rev. Lett. **95**, 226801 (2005).

[Kane05b] C. L. Kane and E. J. Mele, *$Z_2$ Topological Order and the Quantum Spin Hall Effect*. Phys. Rev. Lett. **95**, 146802 (2005).

[Kedem12] Y. Kedem, *Using technical noise to increase the signal-to-noise ratio of measurements via imaginary weak values*. Phys. Rev. A **85**, 060102 (2012).

[Kitaev01] A. Y. Kitaev, *Unpaired Majorana fermions in quantum wires*. Physics-Uspekhi **44**, 131 (2001).

[Kitaev09] A. Kitaev, *Periodic table for topological insulators and superconductors*. AIP Conference Proceedings **1134**, 22 (2009).

[Klich02] I. Klich, *Full Counting Statistics: An elementary derivation of Levitov's formula*. eprint arXiv:cond-mat/0209642 (2002).

[Klitzing80] K. v. Klitzing, G. Dorda, and M. Pepper, *New Method for High-Accuracy Determination of the Fine-Structure Constant Based on Quantized Hall Resistance*. Phys. Rev. Lett. **45**, 494 (1980).

[Knee13a] G. C. Knee, G. A. D. Briggs, S. C. Benjamin, and E. M. Gauger, *Quantum sensors based on weak-value amplification cannot overcome decoherence*. Phys. Rev. A **87**, 012115 (2013).

[Knee13b] G. C. Knee and E. M. Gauger, *Weak-value amplification offers no fundamental advantage for overcoming technical imperfections*. arXiv:1306.6321 (2013).

[Kocsis11] S. Kocsis, B. Braverman, S. Ravets, M. J. Stevens, R. P. Mirin, L. K. Shalm, and A. M. Steinberg, *Observing the Average Trajectories of Single Photons in a Two-Slit Interferometer*. Science **332**, 1170 (2011).

[Kofman12] A. G. Kofman, S. Ashhab, and F. Nori, *Nonperturbative theory of weak pre- and post-selected measurements*. Physics Reports **520**, 43 (2012).

[Koike11] T. Koike and S. Tanaka, *Limits on amplification by Aharonov-Albert-Vaidman weak measurement*. Phys. Rev. A **84**, 062106 (2011).

[Komiyama96] S. Komiyama and H. Hirai, *Two representations of the current density in charge-transport problems*. Phys. Rev. B **54**, 2067 (1996).

[König07] M. König, S. Wiedmann, C. Brüne, A. Roth, H. Buhmann, L. W. Molenkamp, X.-L. Qi, and S.-C. Zhang, *Quantum Spin Hall Insulator State in HgTe Quantum Wells*. Science **318**, 766 (2007).

[König13] M. König, M. Baenninger, A. G. F. Garcia, N. Harjee, B. L. Pruitt, C. Ames, P. Leubner, C. Brüne, H. Buhmann, L. W. Molenkamp, and D. Goldhaber-Gordon, *Spatially Resolved Study of Backscattering in the Quantum Spin Hall State*. Phys. Rev. X **3**, 021003 (2013).

[Laughlin81] R. B. Laughlin, *Quantized Hall conductivity in two dimensions*. Phys. Rev. B **23**, 5632 (1981).

[Lee12] Y.-W. Lee, Y.-L. Lee, and C.-H. Chung, *Nonequilibrium noise correlations in a point contact of helical edge states*. Phys. Rev. B **86**, 235121 (2012).

[Leggett89] A. J. Leggett, *Comment on "How the result of a measurement of a component of the spin of a spin-(1/2 particle can turn out to be 100"*. Phys. Rev. Lett. **62**, 2325 (1989).

[Levitov93] L. Levitov and G. Lesovik, *Charge distribution in quantum shot noise*. JETP Letters **58**, 230 (1993).

[Li12] J. Li, G. Fleury, and M. Büttiker, *Scattering theory of chiral Majorana fermion interferometry*. Phys. Rev. B **85**, 125440 (2012).

[Liu08] C. Liu, T. L. Hughes, X.-L. Qi, K. Wang, and S.-C. Zhang, *Quantum Spin Hall Effect in Inverted Type-II Semiconductors*. Phys. Rev. Lett. **100**, 236601 (2008).

[Liu11a] C.-X. Liu, J. C. Budich, P. Recher, and B. Trauzettel, *Charge-spin duality in nonequilibrium transport of helical liquids*. Phys. Rev. B **83**, 035407 (2011).

[Liu11b] C.-X. Liu and B. Trauzettel, *Helical Dirac-Majorana interferometer in a superconductor-topological insulator sandwich structure*. Phys. Rev. B **83**, 220510(2011) (2011).

[Liu12] J. Liu, A. C. Potter, K. T. Law, and P. A. Lee, *Zero-Bias Peaks in the Tunneling Conductance of Spin-Orbit-Coupled Superconducting Wires with and without Majorana End-States*. Physical Review Letters **109**, 267002 (2012).

[Lundeen11] J. S. Lundeen, B. Sutherland, A. Patel, C. Stewart, and C. Bamber, *Direct measurement of the quantum wavefunction*. Nature **474**, 188 (2011).

[Lutchyn10] R. M. Lutchyn, J. D. Sau, and S. Das Sarma, *Majorana Fermions and a Topological Phase Transition in Semiconductor-Superconductor Heterostructures*. Phys. Rev. Lett. **105**, 077001 (2010).

[Maciejko09] J. Maciejko, C. Liu, Y. Oreg, X. Qi, C. Wu, and S. Zhang, *Kondo Effect in the Helical Edge Liquid of the Quantum Spin Hall State*. Phys. Rev. Lett. **102**, 256803 (2009).

[Martin96] T. Martin, *Wave packet approach to noise in N-S junctions*. Physics Letters A **220**, 137 (1996).

[Min06] H. Min, J. E. Hill, N. A. Sinitsyn, B. R. Sahu, L. Kleinman, and A. H. MacDonald, *Intrinsic and Rashba spin-orbit interactions in graphene sheets*. Phys. Rev. B **74**, 165310 (2006).

[Moore91] G. Moore and N. Read, *Nonabelions in the fractional quantum hall effect*. Nuclear Physics B **360**, 362 (1991).

[Moore07] J. E. Moore and L. Balents, *Topological invariants of time-reversal-invariant band structures*. Phys. Rev. B **75**, 121306 (2007).

[Mourik12] V. Mourik, K. Zuo, S. M. Frolov, S. R. Plissard, E. P. A. M. Bakkers, and L. P. Kouwenhoven, *Signatures of Majorana Fermions in Hybrid Superconductor-Semiconductor Nanowire Devices*. Science **336**, 1003 (2012).

[Nakamura12] K. Nakamura, A. Nishizawa, and M.-K. Fujimoto, *Evaluation of weak measurements to all orders*. Phys. Rev. A **85**, 012113 (2012).

[Nayak07] C. Nayak, S. H. Simon, A. Stern, M. Freedman, and S. D. Sarma, *Non-Abelian Anyons and Topological Quantum Computation*. Rev. Mod. Phys. **80**, 1083. (2007).

[Neder07] I. Neder, N. Ofek, Y. Chung, M. Heiblum, D. Mahalu, and V. Umansky, *Interference between two independent electrons: observation of two-particle Aharonov-Bohm interference*. Nature **448**, 333 (2007).

[Nilsson10] J. Nilsson and A. R. Akhmerov, *Theory of non-Abelian Fabry-Perot interferometry in topological insulators*. Phys. Rev. B **81**, 205110 (2010).

[Nishizawa12] A. Nishizawa, K. Nakamura, and M.-K. Fujimoto, *Weak-value amplification in a shot-noise-limited interferometer*. Phys. Rev. A **85**, 062108 (2012).

[Nomura07] K. Nomura, M. Koshino, and S. Ryu, *Topological Delocalization of Two-Dimensional Massless Dirac Fermions*. Phys. Rev. Lett. **99**, 146806 (2007).

[Oreg10] Y. Oreg, G. Refael, and F. von Oppen, *Helical Liquids and Majorana Bound States in Quantum Wires*. Phys. Rev. Lett. **105**, 177002 (2010).

[Orth13] C. P. Orth, G. Strübi, and T. L. Schmidt, *Point contacts and localization in generic helical liquids*. Phys. Rev. B **88**, 165315 (2013).

[Pang12] S. Pang, S. Wu, and Z.-B. Chen, *Weak measurement with orthogonal preselection and postselection*. Phys. Rev. A **86**, 022112 (2012).

[Park13] S. Park, J. E. Moore, and H. S. Sim, *Absence of Aharonov-Bohm effect of chiral Majorana fermion edge states*. arXiv:1307.7484 (2013).

[Pendry94] J. Pendry, *Symmetry and transport of waves in one-dimensional disordered systems*. Advances in Physics **43**, 461 (1994).

[Peres89] A. Peres, *Quantum measurements with postselection*. Phys. Rev. Lett. **62**, 2326 (1989).

[Pfeifer11] M. Pfeifer and P. Fischer, *Weak value amplified optical activity measurements*. Opt. Express **19**, 16508 (2011).

[Puentes12] G. Puentes, N. Hermosa, and J. P. Torres, *Weak Measurements with Orbital-Angular-Momentum Pointer States*. Phys. Rev. Lett. **109**, 040401 (2012).

[Qi06] X.-L. Qi, Y.-S. Wu, and S.-C. Zhang, *Topological quantization of the spin Hall effect in two-dimensional paramagnetic semiconductors*. Phys. Rev. B **74**, 085308 (2006).

[Qi11] X. Qi and S. Zhang, *Topological insulators and superconductors*. Rev. Mod. Phys. **83**, 1057 (2011).

[Rokhinson12] L. P. Rokhinson, X. Liu, and J. K. Furdyna, *Observation of the fractional ac Josephson effect: the signature of Majorana particles*. Nature Physics **8**, 795 (2012).

[Romeo12] F. Romeo, R. Citro, D. Ferraro, and M. Sassetti, *Electrical switching and interferometry of massive Dirac particles in topological insulator constrictions*. Phys. Rev. B **86**, 165418 (2012).

[Rothe10] D. G. Rothe, R. W. Reinthaler, C. Liu, L. W. Molenkamp, S. Zhang, and E. M. Hankiewicz, *Fingerprint of different spin-orbit terms for spin transport in HgTe quantum wells*. New J. Phys. **12**, 065012 (2010).

[Roy09] R. Roy, *Topological phases and the quantum spin Hall effect in three dimensions*. Phys. Rev. B **79**, 195322 (2009).

[Ryu09] S. Ryu, A. Schnyder, A. Furusaki, and A. Ludwig, *Topological insulators and superconductors: ten-fold way and dimensional hierarchy*. New J. Phys. **12**, 065010 (2009).

[Salazar-Serrano14] L. J. Salazar-Serrano, D. Janner, N. Brunner, V. Pruneri, and J. P. Torres, *Measurement of sub-pulse-width temporal delays via spectral interference induced by weak value amplification*. Phys. Rev. A **89**, 012126 (2014).

[Samuelsson02] P. Samuelsson and M. Büttiker, *Chaotic Dot-Superconductor Analog of the Hanbury Brown–Twiss Effect*. Phys. Rev. Lett. **89**, 046601 (2002).

[Samuelsson04] P. Samuelsson, E. Sukhorukov, and M. Büttiker, *Two-particle Aharonov-Bohm effect and entanglement in the electronic Hanbury Brown–Twiss setup*. Phys. Rev. Lett. **92**, 26805 (2004).

[Sau12] J. D. Sau, E. Berg, and B. I. Halperin, *On the possibility of the fractional ac Josephson effect in non-topological conventional superconductor-normal-superconductor junctions*. arXiv:1206.4596 (2012).

[Schmidt11] T. L. Schmidt, *Current Correlations in Quantum Spin Hall Insulators*. Phys. Rev. Lett. **107**, 096602 (2011).

[Schmidt12] T. L. Schmidt, S. Rachel, F. von Oppen, and L. I. Glazman, *Inelastic Electron Backscattering in a Generic Helical Edge Channel*. Phys. Rev. Lett. **108**, 156402 (2012).

[Schnyder08] A. P. Schnyder, S. Ryu, A. Furusaki, and A. W. W. Ludwig, *Classification of topological insulators and superconductors in three spatial dimensions*. Phys. Rev. B **78**, 195125 (2008).

[Shockley39] W. Shockley, *On the Surface States Associated with a Periodic Potential*. Phys. Rev. **56**, 317 (1939).

[Simon83] B. Simon, *Holonomy, the Quantum Adiabatic Theorem, and Berry's Phase*. Phys. Rev. Lett. **51**, 2167 (1983).

[Skinner12] B. Skinner, T. Chen, and B. I. Shklovskii, *Why Is the Bulk Resistivity of Topological Insulators So Small?* Phys. Rev. Lett. **109**, 176801 (2012).

[Starling09] D. J. Starling, P. B. Dixon, A. N. Jordan, and J. C. Howell, *Optimizing the signal-to-noise ratio of a beam-deflection measurement with interferometric weak values*. Phys. Rev. A **80**, 041803 (2009).

[Stern13] A. Stern and N. H. Lindner, *Topological Quantum Computation-From Basic Concepts to First Experiments*. Science **339**, 1179 (2013).

[Ström09] A. Ström and H. Johannesson, *Tunneling between Edge States in a Quantum Spin Hall System*. Phys. Rev. Lett. **102**, 096806 (2009).

[Strübi11] G. Strübi, W. Belzig, M.-S. Choi, and C. Bruder, *Interferometric and Noise Signatures of Majorana Fermion Edge States in Transport Experiments*. Phys. Rev. Lett. **107**, 136403 (2011).

[Strübi13] G. Strübi and C. Bruder, *Measuring Ultrasmall Time Delays of Light by Joint Weak Measurements*. Phys. Rev. Lett. **110**, 083605 (2013).

[Su79] W. P. Su, J. R. Schrieffer, and A. J. Heeger, *Solitons in Polyacetylene*. Phys. Rev. Lett. **42**, 1698 (1979).

[Susa12] Y. Susa, Y. Shikano, and A. Hosoya, *Optimal probe wave function of weak-value amplification*. Phys. Rev. A **85**, 052110 (2012).

[Tanaka13] S. Tanaka and N. Yamamoto, *Information amplification via postselection: A parameter-estimation perspective*. Phys. Rev. A **88**, 042116 (2013).

[Teo09] J. C. Y. Teo and C. L. Kane, *Critical behavior of a point contact in a quantum spin Hall insulator*. Phys. Rev. B **79**, 235321 (2009).

[Thouless82] D. J. Thouless, M. Kohmoto, M. P. Nightingale, and M. den Nijs, *Quantized Hall Conductance in a Two-Dimensional Periodic Potential*. Phys. Rev. Lett. **49**, 405 (1982).

[Tiwari12] R. P. Tiwari, U. Zülicke, and C. Bruder, *Majorana fermions from Landau quantization in a superconductor–topological-insulator hybrid structure*. Phys. Rev. Lett. **110**, 186805 (2012).

[Väyrynen13] J. I. Väyrynen, M. Goldstein, and L. I. Glazman, *Helical Edge Resistance Introduced by Charge Puddles*. Phys. Rev. Lett. **110**, 216402 (2013).

[Virtanen11] P. Virtanen and P. Recher, *Dephasing of spin and charge interference in helical Luttinger liquids*. Phys. Rev. B **83**, 115332 (2011).

[Volovik03] G. E. Volovik, *The Universe in a Helium Droplet*. Clarendon Press (2003).

[Weeks11] C. Weeks, J. Hu, J. Alicea, M. Franz, and R. Wu, *Engineering a Robust Quantum Spin Hall State in Graphene via Adatom Deposition*. Phys. Rev. X **1**, 021001 (2011).

[Wiseman10] H. Wiseman and G. Milburn, *Quantum Measurement and Control*. Cambridge University Press (2010).

[Wu06] C. Wu, B. A. Bernevig, and S. Zhang, *Helical Liquid and the Edge of Quantum Spin Hall Systems*. Phys. Rev. Lett. **96**, 106401 (2006).

[Wu11] S. Wu and Y. Li, *Weak measurements beyond the Aharonov-Albert-Vaidman formalism*. Phys. Rev. A **83**, 052106 (2011).

[Wunderlich05] J. Wunderlich, B. Kaestner, J. Sinova, and T. Jungwirth, *Experimental Observation of the Spin-Hall Effect in a Two-Dimensional Spin-Orbit Coupled Semiconductor System*. Phys. Rev. Lett. **94**, 047204 (2005).

[Xu06] C. Xu and J. E. Moore, *Stability of the quantum spin Hall effect: Effects of interactions, disorder, and $Z_2$ topology*. Phys. Rev. B **73**, 045322 (2006).

[Xu13] X.-Y. Xu, Y. Kedem, K. Sun, L. Vaidman, C.-F. Li, and G.-C. Guo, *Phase Estimation with Weak Measurement Using a White Light Source*. Phys. Rev. Lett. **111**, 033604 (2013).

[Yao07] Y. Yao, F. Ye, X.-L. Qi, S.-C. Zhang, and Z. Fang, *Spin-orbit gap of graphene: First-principles calculations*. Phys. Rev. B **75**, 041401 (2007).

[Yu10] R. Yu, W. Zhang, H.-J. Zhang, S.-C. Zhang, X. Dai, and Z. Fang, *Quantized Anomalous Hall Effect in Magnetic Topological Insulators*. Science **329**, 61 (2010).

[Zhang13] L. Zhang, A. Datta, and I. A. Walmsley, *Precision metrology using weak measurements*. arXiv:1310.5302 (2013).

[Zhou12] X. Zhou, Z. Xiao, H. Luo, and S. Wen, *Experimental observation of the spin Hall effect of light on a nanometal film via weak measurements*. Phys. Rev. A **85**, 043809 (2012).

[Zhu11] X. Zhu, Y. Zhang, S. Pang, C. Qiao, Q. Liu, and S. Wu, *Quantum measurements with preselection and postselection*. Phys. Rev. A **84**, 052111 (2011).

[Zilberberg11] O. Zilberberg, A. Romito, and Y. Gefen, *Charge Sensing Amplification via Weak Values Measurement*. Phys. Rev. Lett. **106**, 080405 (2011).

# List of publications

1. C. P. Orth, G. Strübi, and T. L. Schmidt, *Point contacts and localization in generic helical liquids.* Phys. Rev. B **88**, 165315 (2013)

2. G. Strübi and C. Bruder, *Measuring ultrasmall time delays of light by joint weak measurements.* Phys. Rev. Lett. **110**, 083605 (2013)

3. G. Strübi, W. Belzig, M.-S. Choi, and C. Bruder, *Interferometric and noise signatures of Majorana fermions edge states in transport experiments.* Phys. Rev. Lett. **107**, 136403 (2011)

4. G. Strübi and D.A. Ivanov, *Vison excitations in near-critical quantum dimer models.* EPL **94**, 57003 (2011)